UNIVERSITÀ
DI PAVIA

UNIVERSITY OF PAVIA
FACULTY OF ENGINEERING
DEPARTMENT OF ELECTRICAL, COMPUTER AND BIOMEDICAL ENGINEERING

MASTER'S DEGREE IN BIOENGINEERING

MASTER THESIS

COMPUTATIONAL HEMODYNAMIC ANALYSIS OF PERCUTANEOUS VALVE MALPOSITIONING

ANALISI COMPUTAZIONALE DELL' EMODINAMICA IN CASO DI MALPOSIZIONAMENTO DELLA VALVOLA PERCUTANEA

Candidate: Letizia Carli

Supervisor: Prof. Michele Conti
Co-supervisor: Prof.ssa Monika Colombo

A.Y. 2024/2025

Abstract (Italiano)

Questa tesi presenta lo sviluppo progressivo di un modello tridimensionale di fluid–structure interaction (FSI) in COMSOL Multiphysics per l'analisi del comportamento emodinamico in fase sistolica precoce di configurazioni di valvola aortica transcatetere (TAVI) in condizioni di malposizionamento. Il lavoro è stato strutturato come un percorso metodologico graduale: dai tutorial preliminari, utili per acquisire familiarità con il workflow FSI, la gestione della mesh mobile e le impostazioni del solutore, fino allo studio di una geometria preliminare di casting, che ha rappresentato il primo banco di prova anatomicamente rilevante per esplorare criticità numeriche e strategie di stabilizzazione del modello. Su queste basi è stato quindi costruito il modello finale modulare TAVI, derivato direttamente dalle geometrie CAD della piattaforma sperimentale del CAVE Lab, così da mantenere coerenza geometrica con il setup in vitro. Sono state investigate cinque configurazioni: valvola nativa, TAVI nominale, due configurazioni con traslazione assiale del dispositivo e una configurazione con disallineamento rotazionale. L'analisi è stata limitata alla fase di apertura valvolare, ritenuta sia clinicamente significativa sia numericamente più gestibile. I risultati mostrano che la valvola nativa mantiene il pattern di apertura più regolare, il getto più centrato e la minore perdita di carico transvalvolare, mentre la configurazione TAVI nominale rappresenta la condizione protesica più equilibrata. Tra i casi malposizionati, la rotazione risulta la condizione più critica dal punto di vista cinematico, con maggiore asimmetria di apertura ed anticipata perdita di convergenza, mentre le traslazioni assiali influenzano soprattutto gli indicatori emodinamici globali, aumentando velocità di getto e pressione transvalvolare. Pur con i limiti legati all'uso di acqua come fluido di lavoro, a leggi costitutive lineari elastiche e alla restrizione alla sola fase di apertura, il modello sviluppato fornisce un

quadro comparativo controllato utile a isolare gli effetti del malposizionamento e costituisce una base metodologica per futuri sviluppi e per una successiva validazione in silico–in vitro.

Abstract (English)

This thesis presents the progressive development of a three-dimensional fluid-structure interaction (FSI) model in COMSOL Multiphysics to investigate the early systolic hemodynamic behaviour of TAVI configurations under malpositioning conditions. The work was structured as a stepwise methodological pathway: preliminary tutorial cases were first used to gain familiarity with the FSI workflow, moving-mesh handling, and solver settings, and were then followed by the study of an initial casting geometry, which served as the first anatomically relevant testbed for exploring numerical limitations and stabilization strategies. On this basis, the final modular TAVI model was developed directly from the CAD geometries of the CAVE Lab experimental platform, thereby preserving geometric consistency with the in vitro setup. Five configurations were analysed: the native valve, a nominal TAVI configuration, two axially translated device positions, and one rotationally misaligned configuration. The investigation was restricted to the valve opening phase, which was considered both clinically meaningful and numerically more manageable. The results show that the native valve preserves the most regular opening pattern, the most centred jet, and the lowest transvalvular pressure drop, whereas the nominal TAVI configuration represents the most balanced prosthetic condition. Among the malpositioned cases, rotational misalignment emerges as the most critical condition from a kinematic standpoint, showing the strongest asymmetry in leaflet motion and the earliest loss of convergence, while axial translations mainly affect global hemodynamic indicators, leading to higher jet velocities and larger transvalvular pressure drops. Although the present framework is limited by the use of water as working fluid, linear elastic constitutive laws, and the restriction to the opening phase only, it provides a controlled comparative setting to isolate the effects of prosthesis malpositioning and rep-

resents a structured methodological basis for future model refinement and in silico–in vitro validation.

Graphical Abstract

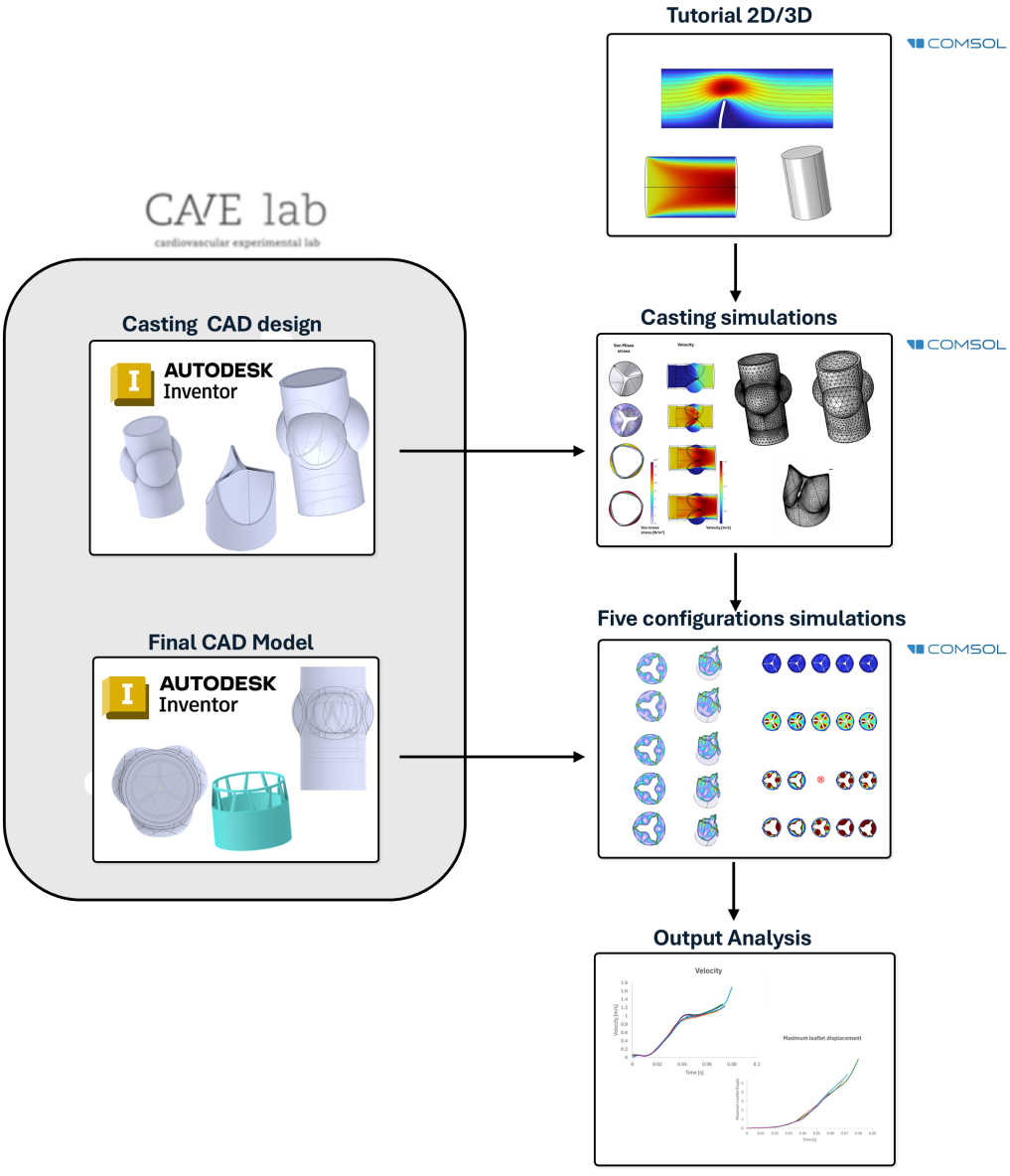

Contents

List of Tables

List of Figures

List of Abbreviations

FSI	fluid–structure interaction
TAVI	transcatheter aortic valve implantation
LVOT	left ventricular outflow tract
AV	aortic valve
CFD	computational fluid dynamics
STJ	sinotubular junction
CAVD	calcific aortic valve stenosis
AS	aortic stenosis
AR	aortic regurgitation
BAV	bicuspid aortic valve
SAVR	surgical aortic valve replacement
PVL	paravalvular leak
EOA	effective orifice area
MCLs	mock circulatory loops
THV	transcatheter heart valve
HV	heart valve
PIV	particle image velocimetry

FE	finite element
ALE	arbitrary Lagrangian Eulerian

Chapter 1

Introduction

Transcatheter Aortic Valve Implantation (TAVI) has become one of the most important treatment options for aortic valve disease, particularly in patients who are at high or intermediate surgical risk. Its growing clinical relevance has progressively shifted attention from the sole feasibility of the procedure to a deeper understanding of the mechanical and hemodynamic factors that determine prosthesis performance after implantation. Among these factors, the final position of the device within the aortic root plays a crucial role, since even limited deviations from the ideal configuration may alter leaflet kinematics, transvalvular flow development, and local stress distributions.

In this context, the current state of the art can be interpreted as a progressive methodological pathway, moving from highly controlled models toward scenarios that are increasingly close to clinical practice. At the first level, computational fluid-structure interaction (FSI) models are particularly valuable because they allow specific variables to be isolated in a controlled manner and provide access to local quantities that are difficult to measure experimentally, such as stress distributions, pressure fields, and detailed velocity patterns. At the second level, in-vitro mock-loop platforms make it possible to reproduce controlled pulsatile conditions and to obtain repeatable experimental measurements, such as pressure, flow rate, and valve kinematics. For this reason, mock loops represent a crucial intermediate step, since they preserve a relatively high degree of control while already introducing a physical verification of valve behaviour.

A third level is represented by animal studies, which provide greater biological realism but also present important limitations, including higher costs, larger biological variability, and reduced control over individual variables. Finally, studies in humans represent the stage at which the actual clinical relevance of the device and of the implantation procedure can be assessed. This is clearly the level closest to clinical practice, but also the one characterized by the highest complexity and the lowest experimental controllability, because multiple anatomical, procedural, and clinical factors interact simultaneously.

Within this framework, when the objective is to isolate in a controlled way the effect of a specific variable, such as prosthesis malpositioning, the most informative levels are the first two: computational modelling and in-vitro mock-loop experimentation. The main challenge is therefore not only to analyse the phenomenon itself, but to do so through a framework in which the computational and experimental levels remain coherent with each other.

Despite the significant growth of the literature on TAVI modelling, controlled computational investigations specifically focused on implantation malpositioning under physiologically consistent boundary conditions are still limited. This is particularly true for three-dimensional COMSOL-based FSI studies, where the full numerical treatment of valve dynamics remains challenging because of strong nonlinearities, moving-mesh limitations, and the complex interaction between the prosthesis and the surrounding anatomy. At the same time, experimental studies performed in mock-loop platforms provide valuable physical insight, but they do not always offer direct access to the local mechanical quantities needed to interpret the observed behaviour in detail. As a result, there is still a need for controlled studies capable of combining these two levels, namely a computational model that is coherent with the experimental platform and suitable for the systematic analysis of malpositioning under physiologically relevant conditions.

Within this framework, the present thesis develops a three-dimensional FSI model in COMSOL Multiphysics to investigate the early systolic behaviour of transcatheter aortic valve configurations under physiologically relevant conditions. The computational workflow was progressively constructed starting from simplified tutorial problems and from an initial casting geometry, which served as a first anatomically relevant testbed for the assessment of solver

settings, mesh-handling strategies, and boundary-condition definitions. These preliminary stages were then used to support the development of the final modular TAVI configuration, derived directly from the experimental CAD geometries provided by the CAVE Lab at Aarhus University. In this way, the final computational domain preserves geometric consistency with the corresponding in-vitro platform and provides the basis for future in silico–in vitro comparison.

The study focuses on five configurations: the native valve, a nominal TAVI configuration, two axially translated configurations obtained by upward and downward displacement of the device, and one rotated configuration. This comparative design was adopted to isolate the hemodynamic consequences of common non-ideal implantation scenarios. The analysis was restricted to the opening phase of the valve, since this stage is both numerically more robust to simulate and clinically meaningful: during early systole, leaflet opening, transvalvular pressure gradient, and jet development are established, thereby directly affecting the forward-flow performance of the device.

To characterize the response of the investigated configurations, the thesis combines qualitative and quantitative analyses. In particular, leaflet opening dynamics and velocity fields are compared visually, while maximum leaflet displacement, maximum von Mises stress, maximum velocity, and transvalvular pressure drop are used as quantitative descriptors of valve kinematics and hemodynamic performance.

Although experimentally informed boundary conditions were adopted and the computational model was kept geometrically consistent with the mock-loop platform, the present framework still relies on important simplifying assumptions, most notably the use of water as working fluid and linear elastic constitutive laws for the solid domains. Accordingly, the quantitative outputs considered in this thesis should be interpreted primarily in a comparative sense across configurations, rather than as direct physiologic predictions of in-vivo valve function. Even though the present work does not include a complete validation campaign, the adopted framework was conceived to remain consistent with the experimental setup, including the use of CAD-derived geometries and experimentally informed boundary conditions, thus representing a structured basis for future validation activities.

1.1 Thesis organization

This thesis is organized as follows. Chapter 2 presents the anatomical, clinical, experimental, and computational background necessary to frame the study, with particular emphasis on the aortic valve (AV), the TAVI approach, mock circulatory loops (MCLs) testing, and current FSI modelling strategies reported in the literature. Chapter 3 describes the methodological framework adopted in the present work, including the numerical formulation in COMSOL, the geometry preparation steps, the construction of the final modular TAVI model from experimental CAD files, and the definition of materials, meshes, boundary conditions, solver settings, and case-study configurations.
Chapter 4 is dedicated to the preliminary numerical development of the workflow. In particular, it reports the tutorial-based benchmark cases and the casting-geometry study that were used to progressively build the computational framework, assess its numerical behaviour, and identify the main limitations and take-home methodological indications that informed the final model.
Chapter 5 presents the computational results obtained for the final TAVI model, combining qualitative observations of leaflet opening and velocity patterns with quantitative comparisons of leaflet displacement, von Mises stress, transvalvular pressure drop, and maximum velocity across the five investigated configurations. Finally, Chapter 6 summarizes the main findings of the thesis, discusses the principal limitations of the proposed approach, and outlines possible future developments, with particular regard to model refinement and in silico–in vitro validation.

Chapter 2

Aortic Valve and TAVI approach: definitions and State-of-Art

This chapter provides the anatomical, clinical, and methodological background necessary to frame the study of TAVI. It first introduces the structure and function of the heart, with particular focus on the AV and the aortic root as a dynamic functional unit. The main pathological conditions affecting the AV are then reviewed, together with current clinical management strategies and the rationale for TAVI. The chapter subsequently presents an overview of experimental in-vitro approaches used to investigate TAVI devices, including standardized testing frameworks and MCLs, followed by a comprehensive review of computational modeling strategies, with emphasis on FSI methods. Finally, experimental and numerical studies from the literature are systematically classified to highlight current state-of-the-art practices, limitations, and open challenges that motivate the objectives of this thesis.

2.1 General view of the heart and its structure

The heart is a hollow, muscular organ located in the middle of the chest, behind the sternum. Its function relies on four chambers working as two coordinated pumps, but the direction and efficiency of blood flow are ensured above all by the four heart valves (Figure 2.1), which act as one-way gates [23].
Blood returning from the body enters the right atrium through the superior

and inferior vena cavae, and blood from the heart muscle itself drains into the same chamber through the coronary sinus. From the right atrium, blood passes into the right ventricle through the tricuspid valve. This valve opens to allow filling of the ventricle and closes to prevent blood from flowing back into the atrium when the ventricle contracts.

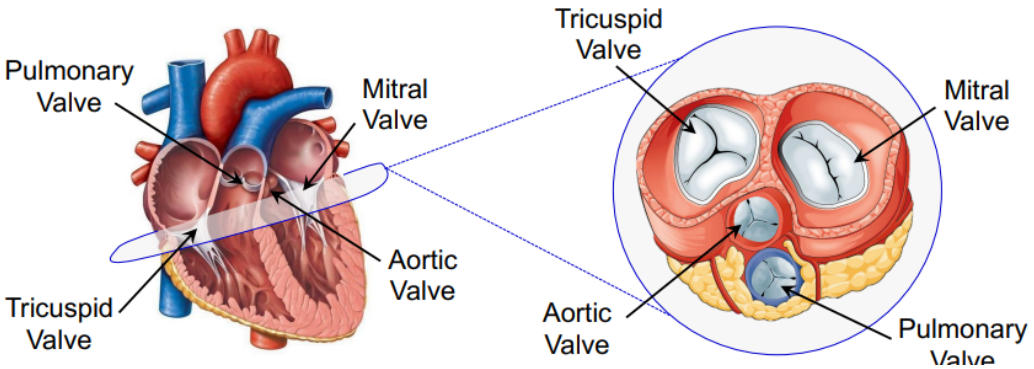

Figure 2.1: Configuration of heart's valves (from Ref [3]).

During contraction of the right ventricle, blood is pushed forward through the outflow tract and crosses the pulmonary valve, which prevents backflow from the pulmonary artery into the ventricle. The pulmonary artery then carries blood to the lungs, where oxygen is taken up in the capillaries surrounding the alveoli [4].

Oxygenated blood returns from the lungs to the left atrium through four pulmonary veins. It then flows into the left ventricle across the mitral valve, which regulates passage from atrium to ventricle and prevents regurgitation during ventricular contraction. Finally, the left ventricle, the main pumping chamber of the left heart, ejects blood into the aorta through the AV, which blocks any backward movement from the aorta into the ventricle.

In this way, each heartbeat is guided by the coordinated opening and closing of the tricuspid, pulmonary, mitral, and aortic valves, whose shared purpose is to maintain forward blood flow and prevent reverse flow throughout the cardiac cycle. A schematic overview of the blood flow pathway through the heart is shown in Figure 2.2.

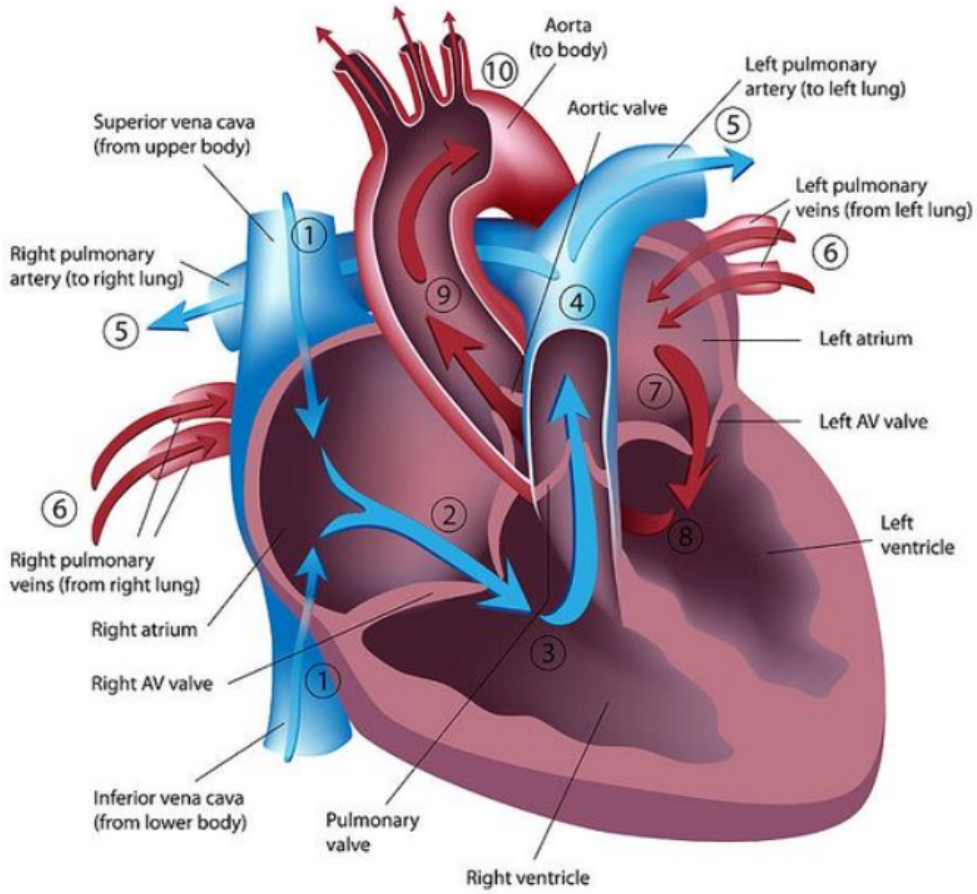

Figure 2.2: Schematic representation of blood flow through the heart (from Ref [4]).

2.2 Aortic root

The aortic root is the short (3.3 cm), anatomically complex transition zone that links the left ventricular outflow tract (LVOT) to the ascending aorta. It behaves like a coordinated functional unit: its geometry and tissue architecture support efficient non-turbolent forward flow in systole, secure leaflet coaptation in diastole, and long-term durability under repetitive loading [24].
The aortic root is composed of the following main components:

- AV and its leaflets with their commissures and the annulus;
- aortic sinuses;

- sinotubular junction (STJ);
- interleaflets triangles.

Each component has specific histological features and anatomical construction [25].

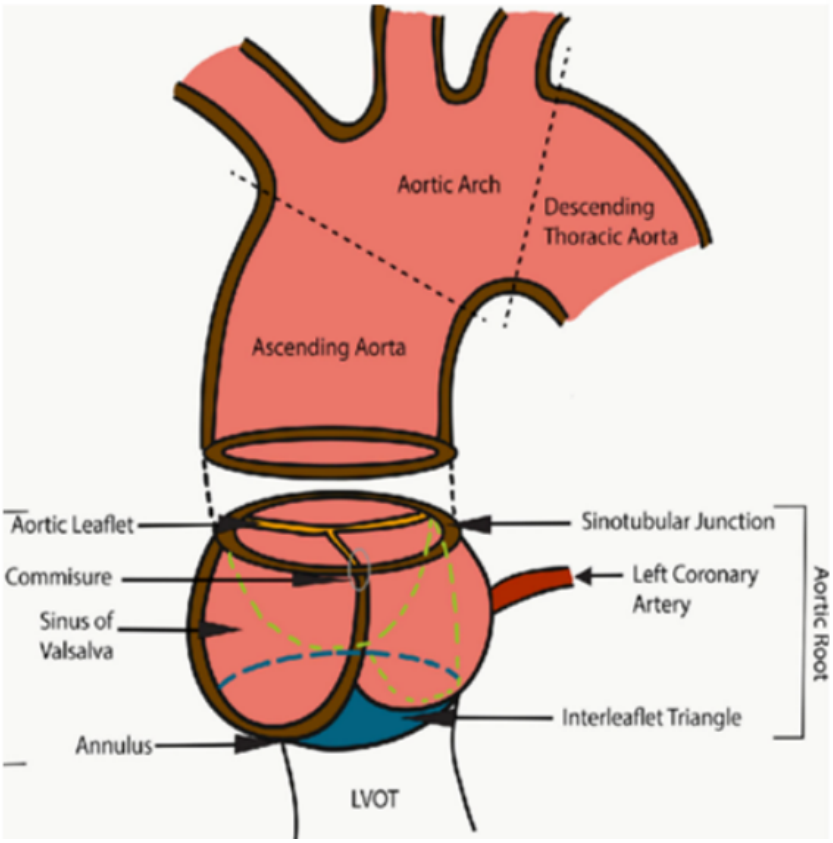

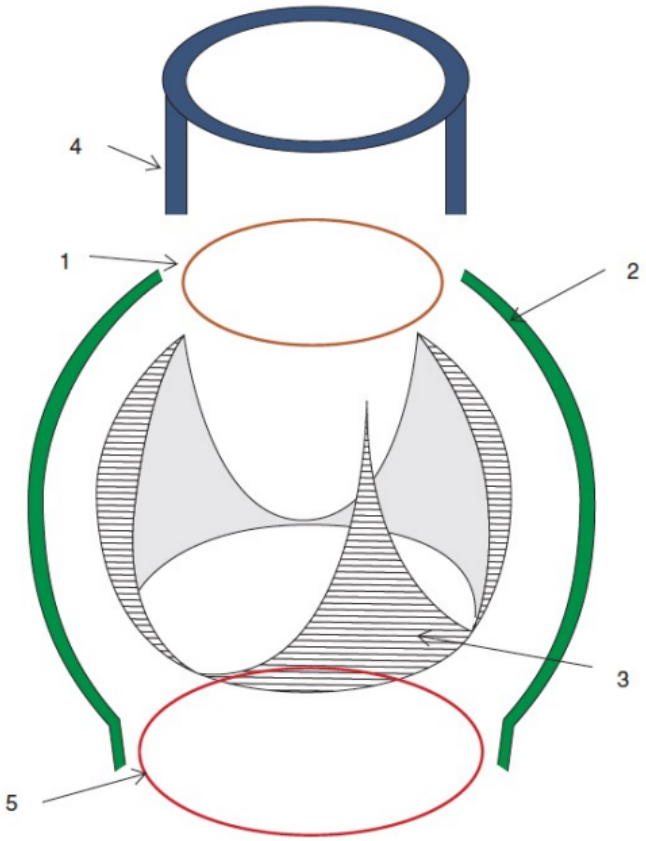

Figure 2.3: Aortic root's components: (1) STJ, (2) Valsalva sinuses, (3) inter-leaflets triangles, (4) ascending aorta, (5) annulus (adapted from Ref [5], [6]).

2.2.1 AV: leaflets, commissures and annulus

The AV is a semilunar valve that is composed of three thin, flexible leaflets (also called cusps). Each leaflet has a basal attachment and a free edge: the base inserts along the aortic annulus/hinge line, while the free margin contributes to valve closure by meeting the adjacent leaflets during diastole. In the normal valve, competence relies on an adequate coaptation area, i.e., a sufficient overlap between the free margins of neighboring leaflets, which prevents retrograde flow into the left ventricle when the valve is closed. Leaflets are conventionally named according to their relationship with the coronary arteries: right coronary, left coronary, and non-coronary leaflets.
Each cusp can be described using distinct anatomical regions that are useful

both for clinical description and for modelling. The hinge is the semilunar insertion zone where the leaflet attaches to the annulus. The belly constitutes the main body of the leaflet and is typically the thinnest and most compliant portion. Toward closure, the coapting surface (the region that apposes the other leaflets) becomes functionally critical because it ensures a tight seal. Near the free edge, the leaflet often presents a specialized zone involved in apposition that is classically referred to as the lunula; the central part of this coapting zone can be thickened, forming the nodule of Arantius, which contributes to central closure. From a surface-structure perspective, the ventricular side of each leaflet is generally smoother, whereas the aortic side can appear more corrugated/crimped, reflecting differences in tissue architecture and loading conditions (adapted from [24] [25]).

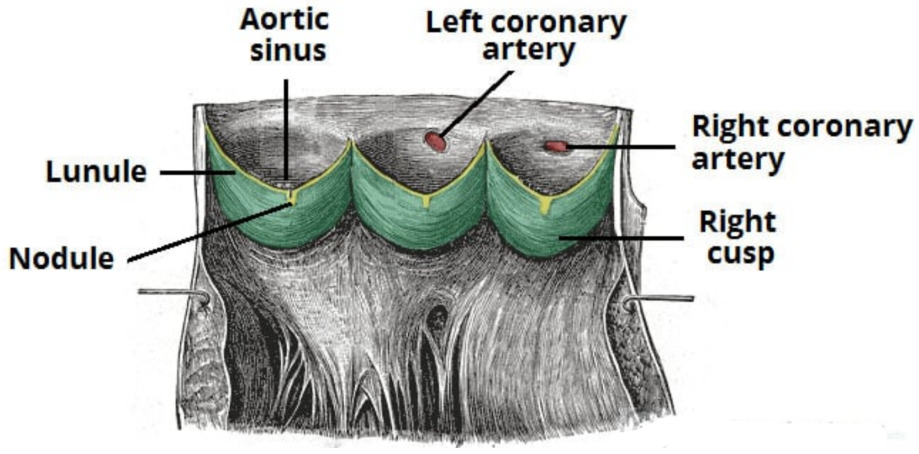

Figure 2.4: The AV cusps, aortic sinuses, and the origin of the coronary arteries (from Ref [7]).

Leaflet thickness is not uniform: it tends to increase toward the free margin and within the coapting portion. Reported thickness values are on the order of $\sim 150 - 180\,\mu$m, although values depend on the measurement method, anatomical location, and tissue state.

The commissures define the lateral boundaries of each cusp. A portion of the leaflet free margin is tethered to the aortic wall at these points, and the three commissures extend superiorly to terminate approximately at the level of the STJ. The leaflet attachment line is commonly called the "aortic annulus".

Although commonly referred to as a ring, the aortic annulus is not a discrete circular structure; it is better described as the three-dimensional, crown-shaped hinge line where the cusps insert into the aortic root.

2.2.2 Valsalva sinus

The spaces between the luminal surface of the three bulges of the aortic root and their respective valvular leaflets are known as the aortic sinuses of Valsalva. The presence of the aortic sinuses is essential for optimal AV performance. By creating a sinus-like space, they facilitate the physiological opening and closing of the native leaflets throughout the cardiac cycle and enhance the fluid-structure interaction between blood flow and the cusps. This configuration helps preserve predominantly laminar flow during ventricular systole, thereby limiting turbulence, reducing systolic energy loss, and keeping the transvalvular pressure gradient low. In diastole, the same sinus geometry also supports effective coronary perfusion.
Within the sinuses of Valsalva, the aortic root wall exhibits a structural gradient-collagen-rich at the base with a progressive increase in elastic lamellae toward the STJ)-and the resulting sinus vortices support physiological leaflet kinematics as we can see in Figure 2.5; accordingly, under pressurization the STJ typically expands more than the annulus, whereas at low pressure the annulus may be relatively larger.

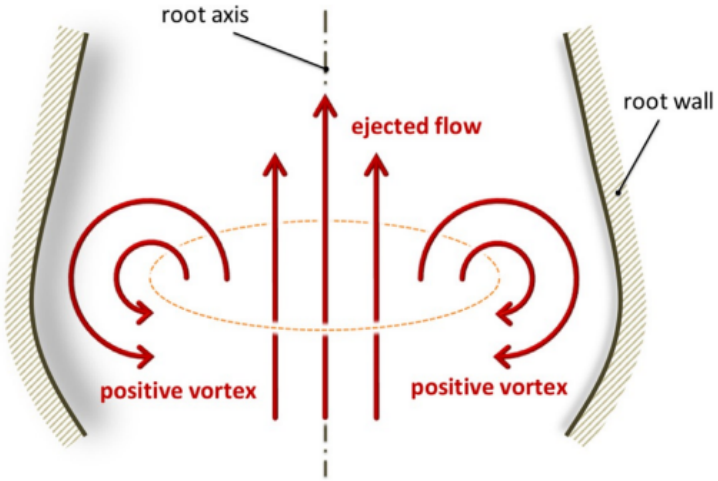

Figure 2.5: Schematic illustration of systolic jet ejection through the aortic root (from Ref [8]).

2.2.3 Sinotubular junction

STJ forms the upper limit of the sinuses and is often referred to as the supra-aortic ridge. Externally, it marks the transition where the straight tubular ascending aorta meets the bulbous sinus segment. From the luminal side, it typically appears as a subtle raised rim created by localized thickening of the aortic wall. Rather than being perfectly round, the STJ follows the contours of the three sinuses, resulting in a gently trilobed, scalloped (trefoil-like) profile.

2.2.4 Interleaflet triangles

Because the aortic cusps insert into the root along semicircular hinge lines, three interleaflet (triangles-triangular wedges of LVOT tissue) extend upward between adjacent sinuses to approximately the level of the STJ (Figure 2.6). The triangle between the left and non-coronary sinuses is in fibrous continuity with the anterior mitral leaflet, forming the mitral–aortic fibrous curtain; the adjacent triangle between the left and non-coronary cusps is typically the largest and lies close to the transverse pericardial sinus. The triangle between the right and non-coronary sinuses relates to the membranous interventricular septum and to the tricuspid valve hinge, and it is also the region anatomically

closest to the central fibrous body and conduction tissues, with the atrioventricular conduction axis passing nearby [9].
Functionally, the interleaflet triangles are key to the dynamic behavior of the aortic root. During systole, root expansion can increase inlet dimensions by roughly 5-15% [25], and the asymmetric deformation of these thin structures allows the root to shift shape (often described as moving from conical toward more cylindrical, and then toward an inverted cone), which helps limit the pressure drop between the left ventricle and the aorta and favors efficient ejection. At the same time, their slender walls make them potential weak points, predisposing to ballooning and aneurysmal changes. In diastole, the triangles also contribute to bearing and distributing closing loads, especially toward end-diastole.

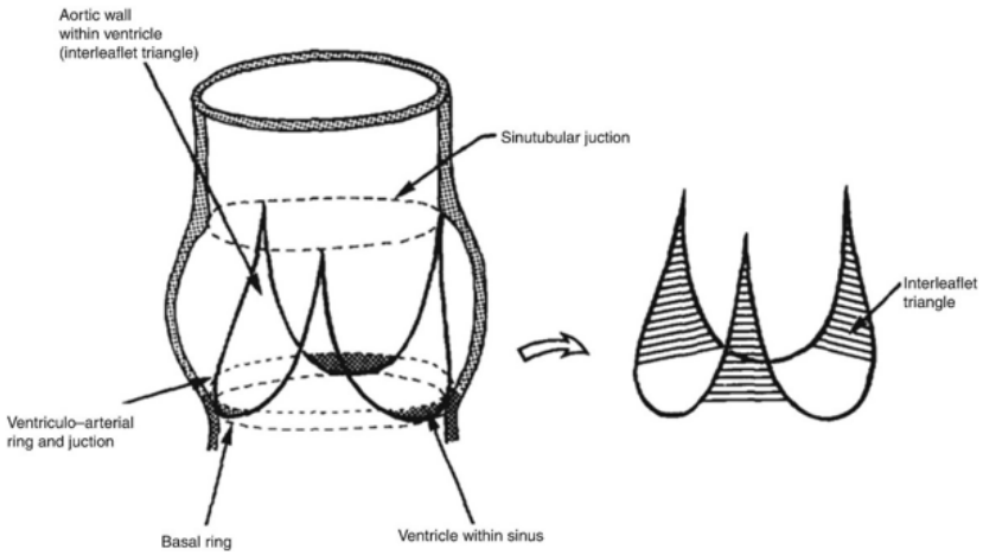

Figure 2.6: Schematic representation of the aortic root geometry highlighting the interleaflet triangles (adapted from [9]).

2.2.5 Aortic root function

The AV and aortic root should be considered a dynamic functional unit rather than a static structure. There is a passive dynamism, in which sub-valvular and supra-valvular regions (including the annular apparatus, sinuses of Valsalva, and the STJ) move throughout the cardiac cycle. This motion supports

favorable flow patterns, such as sinus vortices, that assist rapid closure and help maintain coronary perfusion during systole. Alongside this, an active dynamism is often described, whereby each component (leaflets, annulus, sinuses, STJ) undergoes coordinated changes in shape, size, and stiffness across the cycle. Functionally, this coordinated behavior enables low-resistance opening during systolic ejection, prompt closure at end-systole, and stable coaptation in diastole, while maintaining physiological loading of the valve and the proximal aorta.

In early systole, the rise in left ventricular pressure initiates leaflet opening and is accompanied by deformation of the aortic root, with outward displacement of the sinus walls that helps accommodate the onset of ejection. During late systole, as the main flow jet is expelled into the ascending aorta, the root remains distended and the sinus geometry promotes near-wall recirculation, creating the conditions that assist the subsequent closing motion of the leaflets. In diastole, the reduction in transvalvular pressure and the elastic recoil of the root favor leaflet coaptation, while the sinus flow patterns support stable closure and facilitate coronary filling.

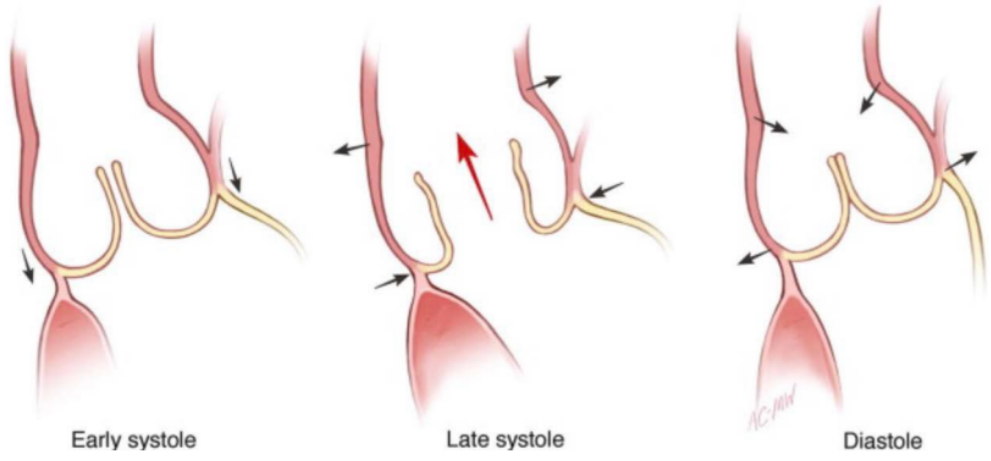

Figure 2.7: Schematic representation of aortic root function across the cardiac cycle (early systole, late systole, diastole) (adapted from Ref [10]).

2.3 AV disease

In adult populations, the main AV disorders include age-associated calcific aortic valve disease progressing to calcific aortic stenosis (the most prevalent valve disease in developed countries), aortic regurgitation due to primary cusp abnormalities and/or aortic root-annular dilatation, congenital bicuspid aortic valve (a common malformation that predisposes to stenosis/regurgitation and proximal aortopathy), and inflammatory/post-inflammatory valve disease (classically rheumatic), so the overall burden increases substantially as populations age [26] [27].

2.3.1 Calcific aortic valve disease and aortic stenosis (CAVD/AS)

Consistent with its clinical impact, calcific AS has been reported to account for 34% of native valve diseases [11]. It is characterized by a slow, progressive fibrocalcific remodeling of the cusps, leading to leaflet thickening, reduced mobility, and ultimately fixed outflow obstruction. As stenosis progresses, flow through the valve becomes an increasingly high-velocity jet with higher transvalvular pressure gradients and elevated laminar and turbulent shear stresses.
Contemporary reviews describe CAVD as a continuum from early thickening/sclerosis to severe stenosis, shaped by epidemiologic factors and individual susceptibility (including genetic and inflammatory/metabolic contributors) [28]. Population data also show that progression tends to accelerate as disease severity increases, underscoring why AS becomes increasingly prevalent and clinically relevant in older age [29].

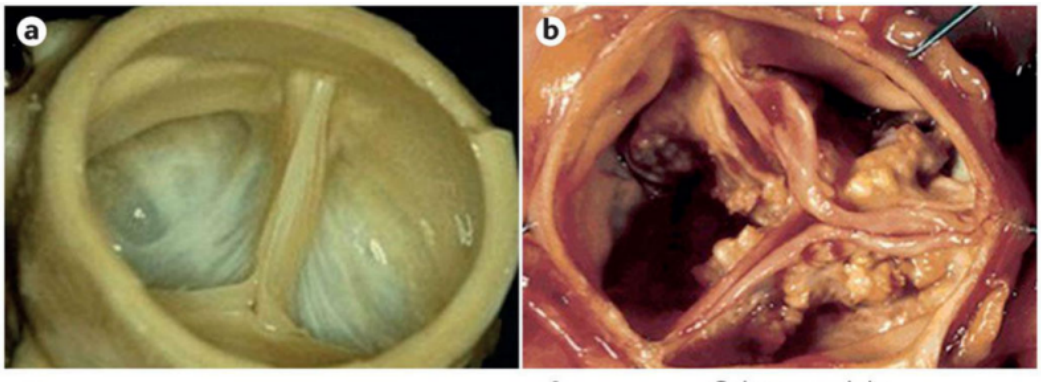

Figure 2.8: Photographs of a) a normal AV and b) an AV with severe calcific aortic stenosis (from Ref [11]).

2.3.2 Aortic regurgitation (AR)

AR is defined by diastolic backflow from the aorta into the left ventricle due to incomplete cusp coaptation, and it can arise from primary leaflet pathology and/or dilatation of the aortic root-annular complex (often in combination). Population data highlight a strong age and sex dependence: AR was detected by color Doppler in 13.0% of men and 8.5% of women [30].
Hemodynamically, AR produces left ventricle volume overload with increased total stroke volume (the amount of blood ejected from a heart's ventricle with each beat); in severe AR, the regurgitant volume may match or exceed the effective forward stroke volume, and chronic compensation can eventually fail, while acute AR can rapidly precipitate pulmonary edema, hypotension, and shock [31].

2.3.3 Congenital bicuspid aortic valve (BAV)

BAV is the most common congenital AV abnormality, with an estimated prevalence of 0.5-2% in the general population [32].
Although it can remain clinically silent for years, BAV predisposes over time to major complications: AR (from cusp prolapse and/or root-ascending aortic dilatation), AS due to dystrophic calcification, infective endocarditis, and progressive ascending aortopathy with risk of aneurysm formation and aortic dissection. Importantly, the associated aortopathy is not only a consequence

of abnormal number of semilunar cursps: pathology-based evidence describes intrinsic, noninflammatory degenerative changes of the aortic media (e.g., elastic fiber fragmentation, smooth muscle cell loss, mucoid extracellular matrix accumulation), supporting the concept of an underlying wall vulnerability and helping explain the frequent association with other congenital lesions [12].

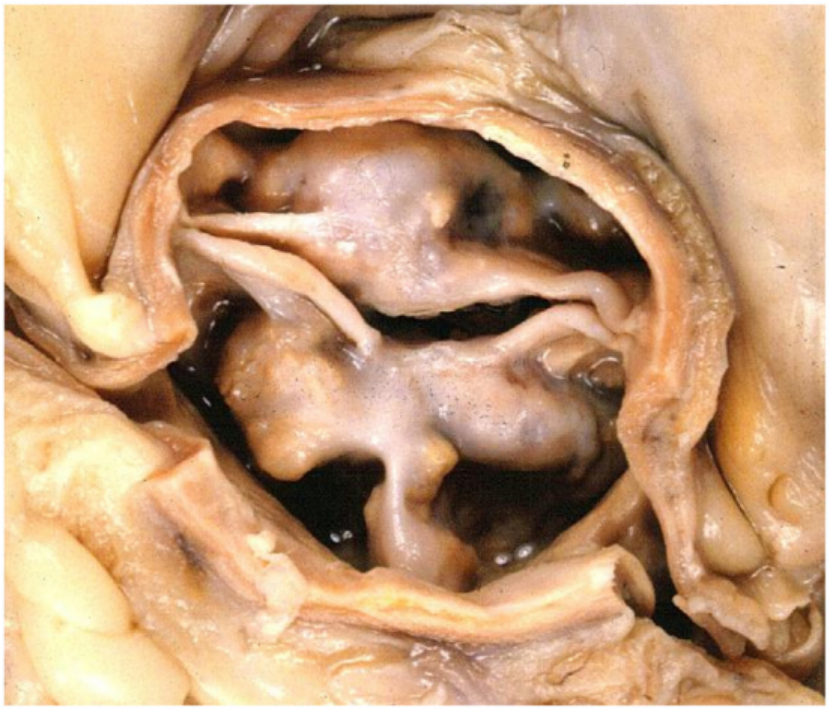

Figure 2.9: Macroscopic view of stenotic BAV with dystrophic calcification (adapted from [12]).

Other AV disease

The remaining major categories of AV pathology include inflammatory/post-inflammatory disease (classically rheumatic heart disease, still a leading cause of valvular disease burden in many low- and middle-income settings) and infective endocarditis, both of which can damage cusps and commissures and produce mixed stenotic-regurgitant phenotypes. In rheumatic heart disease, the AV is often involved together with the mitral valve rather than in isolation [33] [34].

2.4 Clinical Management of AV disease: TAVI

Clinical management of AV disease mainly relies on two strategies: valve repair (when feasible) or, more commonly in AV pathology, valve replacement using either surgical prostheses (SAVR) or transcatheter devices. Since 30%-50% [14] of patients are poor candidates for open-heart surgery due to advanced age, frailty, or comorbidities, TAVI, with the first human procedure perform in 2002, has become the preferred less-invasive replacement option, offering valve implantation via a catheter-based approach [35].

2.4.1 TAVI approach

In terms of what the intervention consists of, TAVI is typically performed in a cardiac catheterization laboratory or a hybrid operating room, most frequently via transfemoral arterial access. After vascular access is obtained and the patient is anticoagulated with heparin, the native AV is crossed and a guidewire is positioned in the left ventricle to provide support for device delivery; a delivery sheath is then advanced into the aorta.

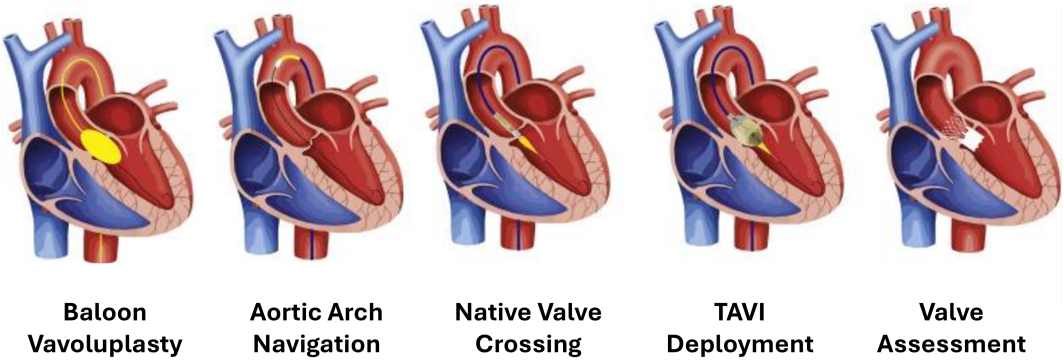

Figure 2.10: Main procedural steps of TAVI, including balloon valvuloplasty, aortic arch navigation, native valve crossing, prosthesis deployment, and final valve assessment (adapted from [13]).

In many protocols, a balloon aortic valvuloplasty may be performed under rapid ventricular pacing to temporarily reduce cardiac output and stabilize the valve/annulus during key steps. The transcatheter valve prosthesis (balloon-expandable or self-expanding, depending on the platform) is advanced ret-

rogradely to the annular plane and deployed under fluoroscopic/angiographic guidance once the position is confirmed. Immediately after implantation, operators assess transvalvular gradients and evaluate for paravalvular leak (PVL); if PVL is significant, post-dilatation can be performed. The sheath is withdrawn with careful surveillance for vascular complications, and transthoracic echocardiography is performed at the end of the procedure and again prior to discharge to document prosthesis function and screen for complications such as significant regurgitation, coronary obstruction-related wall motion changes, or pericardial effusion.
In addition to avoiding sternotomy and cardiopulmonary bypass, a major practical advantage is the shift toward a "minimalist" pathway (selected cases), which can reduce resource utilization and enable shorter length of stay, including same-day or next-day discharge, with associated reductions in hospitalization-related costs in experienced centers and rigorously selected patients (adapted from [35] [36]).

After implantation strategy and procedural workflow, it is worth briefly noting that contemporary TAVI prostheses can be broadly divided into two main categories: balloon-expandable and self-expanding valves. Although the present thesis focuses on an idealized TAVI configuration rather than on a specific commercial prosthesis, this distinction is relevant because the two device families differ in deployment mechanism, structural design, and interaction with the surrounding anatomy.
Balloon-expandable valves, such as those of the Edwards SAPIEN family, are deployed by balloon inflation, typically under rapid ventricular pacing. This deployment mode provides high radial force over a short time interval and generally enables accurate positioning once the prosthesis is aligned with the annular plane. Their structure is typically based on a metallic frame carrying biological leaflets, and newer generations have been developed to improve sealing and reduce PVL [37] [38].
Self-expanding valves, exemplified by the Medtronic CoreValve/Evolut family, rely instead on a nitinol frame that gradually expands after release. In contrast to balloon-expandable systems, they exert a more progressive and sustained radial force and may offer the possibility of repositioning or recapture during

deployment. Their elongated frame geometry can result in a more extended interaction with the annulus and the LVOT [39].

Figure 2.11: Comparison between latest-generation balloon-expandable and self-expanding TAVI prostheses (adapted from Ref. [14]).

From a comparative perspective, the main difference between the two families lies in the balance between deployment control and adaptability to the native anatomy. Balloon-expandable valves usually offer a more immediate and controlled expansion, which can favor precise placement and stable annular anchoring. Self-expanding valves, on the other hand, provide a more gradual release and continuous outward force, which may allow better conformability to complex anatomies and greater procedural flexibility.

2.5 Experimental studies on TAVI

TAVI has evolved from a rescue therapy in inoperable patients to a mainstream alternative to SAVR, including lower-risk cohorts. This shift places strong emphasis on device durability, hemodynamic performance, and procedure-dependent failure modes (e.g., PVL, malposition, underexpansion/ovality, coronary access issues). In this context, in-vitro testing and physical simulation (test benching) are essential because they provide (i) repeatable, well-controlled evaluation of performance and failure mechanisms, and (ii) quantitative outputs that can be linked to clinically meaningful endpoints and used to validate computational models.

2.5.1 Standard for in-vitro testing

The primary international reference is the International Organization for Standardization ISO 5840 family for cardiac valve prostheses, including the transcatheter-specific part ISO 5840-3:2021 [1] [2]. These documents define minimum performance metrics, test conditions, and durability evidence for transcatheter valves. Across ISO-guided hydrodynamic and durability testing, the recurring "rules" for experiments are:

- physiologic boundary conditions (pressures/flows/heart rate) and controlled waveform definitions;
- standardized metrics: effective orifice area (EOA), mean transvalvular pressure drop, regurgitant fraction/volume, and (in advanced research setups) energy loss;
- worst-case conditions: testing across relevant annulus sizes, deployment states (including non-ideal expansion), and sometimes low output states associated with higher risk of flow stasis;
- durability demonstration via accelerated wear (cycle-based), and documentation of damage modes and performance drift.

Mock circulatory loops

While ISO documents specify what should be measured and how results should be reported, the practical implementation of these requirements relies on dedicated experimental platforms commonly referred to as MCLs. MCLs are bench-top hydraulic systems designed to replicate the key hemodynamic features of the cardiovascular system under controlled and repeatable conditions. In the context of valve testing, the most widely adopted implementation is the left-heart simulator, often called a pulse duplicator. Conceptually, a pulse duplicator provides (i) a pulsatile "ventricular" source that generates the cardiac cycle, (ii) a valve test section where the aortic root/annulus model and the transcatheter heart valve (THV) are mounted, and (iii) an "arterial afterload"

module that reproduces the pressure-flow relationship of the systemic circulation through adjustable resistive and compliant elements (Windkessel-like behavior) [40] [41].
This architecture is crucial for THV bench testing because it allows the experimenter to decouple and tune the principal hemodynamic determinants (heart rate, stroke volume/cardiac output, mean arterial pressure and waveform shape) while keeping the geometry and deployment configuration fixed. In practice, this means that the same valve/root setup can be tested across multiple standardized working points, ensuring that measured differences in EOA, pressure drop or regurgitation arise from valve design/deployment state rather than from uncontrolled physiological variability.

Parameter	**Typical value**
Heart rate (HR)	70 bpm
Cardiac output (CO)	5 L/min
Systemic aortic pressure	120/80 mmHg
Test fluid viscosity	3.5–4.5 cP at 37°C
Test fluid density	1.05 g/mL
Temperature	37±2 °C

Table 2.1: Typical ISO-like Hemodynamic Conditions in TAVI In-Vitro Tests (from Ref. [1], [2]).

In classical hydrodynamic testing, the pulse duplicator is primarily used to compute global metrics (EOA, mean transvalvular gradient/pressure drop, and regurgitant fraction/volume) from synchronized pressure and flow signals. However, the state-of-the-art in TAVI experimentation increasingly extends beyond global outputs. Unlike surgical valves, TAVI creates a neo-sinus region (between the THV frame and the native aortic root), and clinically relevant outcomes such as PVL, sinus washout/stasis, and coronary flow sensitivity are strongly modulated by implantation strategy (e.g., implant depth, commissural alignment) and by the interplay between the deployed stent frame, native leaflets and root compliance. For this reason, modern mock loops frequently move from simplified rigid annulus holders to more realistic aortic

root phantoms (often silicone, sometimes including native leaflet analogues and coronary ostia), and may be equipped with optical access for particle image velocimetry (PIV) or other flow-field diagnostics. In this configuration, the MCL is not only a device-benchmarking tool, but also a platform to isolate and quantify how specific procedural variables (depth, rotation/alignment, under-expansion/ovality) translate into measurable changes in leakage pathways, jet structures, vortex organization and washout within the sinus/neo-sinus compartments.
Aligned with ISO-style hydrodynamic testing, a TAVI-oriented mock loop should minimally include:

1. Pulsatile actuation (hydromechanical pump or piston system) capable of reproducing target waveforms.

2. Compliance elements (aortic compliance chamber and/or compliant vessel segments) to match physiologic pressure-volume response.

3. Resistive elements (systemic resistance) to tune mean pressure and flow split.

4. Test section / aortic root phantom (rigid or compliant), often including: sinuses of Valsalva, native leaflets, LVOT bulge and optionally coronary ostia.

5. Thermal control (often 37 °C) and blood analog fluid (water-glycerol mixtures are common when matching viscosity for PIV; saline/water may be used depending on the objective).

6. Instrumentation: pressure transducers upstream/downstream, flowmeter(s), data acquisition synchronized with the cardiac cycle.

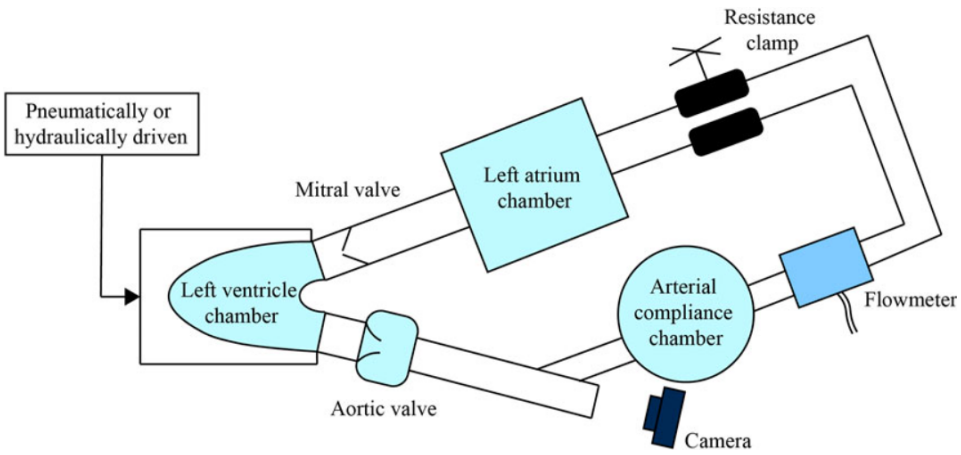

Figure 2.12: A simple MCL construction to study prosthetic heart valves (from Ref [15]).

A common commercial implementation of the pulse-duplicator concept is the ViVitro pulse duplicator system reported in Fig. 2.13, which integrates the test chamber, sensors and data acquisition in a reproducible setup and is widely used as a baseline platform for ISO-style valve testing.

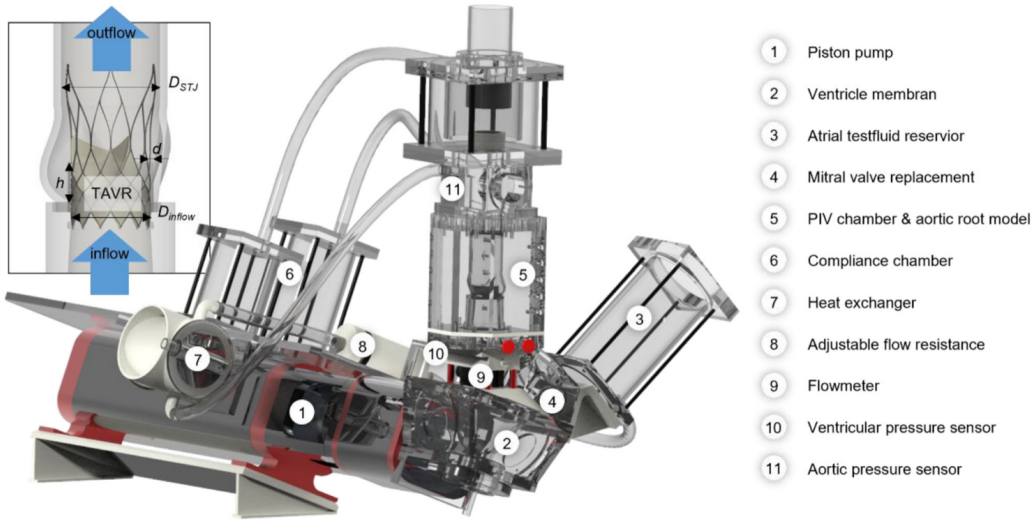

Figure 2.13: Setup of the hydrodynamic circulation loop (pulse duplicator system) to simulate physiological and pathophysiological flow and pressure conditions (from Ref [16]).

Figure 2.14: Illustration of the complete Vivitro Pulse Duplicator system (from Ref [17]).

In addition to standard bench measurements acquired in the ViVitro pulse duplicator (e.g., pressure drop, flow rate and valve kinematics), four-dimensional flow magnetic resonance imaging (4D Flow MRI) can be integrated within mock-loop experiments as an advanced volumetric flow measurement technique [42]. This approach provides time-resolved 3D velocity fields across the entire phantom, enabling the derivation of additional hemodynamic descriptors such as flow jet topology, turbulent kinetic energy, and energy-loss metrics, which are not directly accessible with conventional loop instrumentation.

2.5.2 How experimental studies cluster in the literature

The scientific literature on in vitro testing and the use of MCLs for the evaluation of TAVI devices is vast, encompassing a range of methodological approaches. Studies can be categorized into three distinct clusters. These clusters reflect a shift from standard hydrodynamic verification toward the investigation of complex fluid-structure interactions, procedural variables, and patient-specific realism.

(1) Impact of Deployment Configuration and Procedural Variables

A significant cluster of studies investigates how operator-dependent variables, specifically implant depth and commissural alignment, alter local hydrodynamics. While global performance metrics (such as EOA and mean pressure gradient) often remain within acceptable ranges despite misalignment, local flow patterns are significantly affected. Salmonsmith et al. [43] demonstrated that while commissural misalignment has a negligible impact on global valvular resistance, it critically influences flow stagnation within the aortic sinuses, potentially increasing thrombotic risk. Similarly, Pott et al. [44] focused on implant depth, revealing that a supra-annular position improves washout in the neo-sinus compared to lower deployments, albeit with potential trade-offs regarding coronary access. Moving beyond bulk flow analysis, Pietrasanta et al. [45] employed high-resolution Tomographic Particle Image Velocimetry (Tomo-PIV) to quantify turbulence. Their findings indicate that lower implantation depths result in constrained stent expansion, leading to elevated Turbulent Kinetic Energy (TKE) and Reynolds shear stresses downstream of the valve, markers associated with blood damage.

(2) The Role of Anatomical Realism and Boundary Conditions

This cluster challenges the validity of idealized testing standards (ISO 5840) by introducing anatomical complexity. The literature suggests that simplified cylindrical geometries often mask potential device failures or suboptimal performance. Kovarovic et al. [46] highlighted the discrepancies between ISO-compliant testing and patient-specific models derived from CT scans, showing that realistic anatomies yield lower performance metrics due to non-circular expansion and geometric constraints. This is supported by earlier work from Gunning et al. [47] and Young et al. [18], who investigated eccentric deployment and non-circular orifice shapes. They observed that asymmetric stent expansion, common in calcified heavy anatomy, distorts velocity fields and creates regions of high shear stress that are undetectable in circular mock loops. Furthermore, Sadat et al. [48] emphasized the importance of material properties, demonstrating that the use of calcified biological models versus rigid plexiglass chambers significantly alters the radial expansion force and functional perfor-

mance of self-expanding valves, advocating for higher bio-fidelity in preclinical testing.

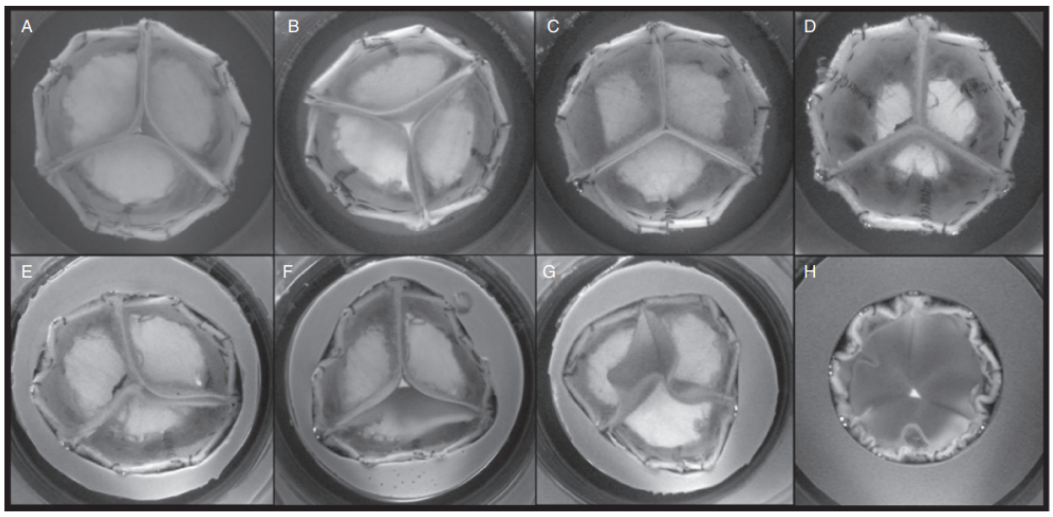

Figure 2.15: Photographs of closing valves in the pulse duplicator during diastole: (A) Nominal, (B) half-triangle with commissures at the corners, (C) half-triangle with commissures midway between the corners, (D) half-undersized, (E) full-elliptical configuration, (F) full-triangle with commissures at the corners, (G) full-triangle with commissures midway between the corners, and (H) full-undersized (from Ref [18]).

(3) Assessment of Thrombotic Risk and Neo-Sinus Hemodynamics

A specialized cluster of research addresses the fluid dynamics within the "neo-sinus" (the space between the native and prosthetic leaflets), which is linked to Hypo-Attenuating Leaflet Thickening (HALT) and subclinical thrombosis. Ncho et al. [49] investigated the hemodynamic impact of native leaflet modification techniques, such as BASILICA. Their in vitro results suggest that lacerating the native leaflet enhances washout and reduces stagnation zones in the neo-sinus, offering a mechanical solution to thrombotic risk. These experimental setups are also crucial for validating computational models. Borowski et al. [50] utilized PIV to validate FSI simulations, confirming that experimental data is essential to identify low-velocity regions prone to thrombus formation that purely numerical models might overestimate or underestimate without calibration.

Cluster	Ref.	Aim	TAVI device	Measurement Techniques
1	Young, 2011, [18]	Impact of non-circular stent configurations on valve performance	Generic Model (26 mm valve)™	Hydrodynamic assessment (Pulse Duplicator)
	Gunning, 2014, [47]	Evaluate the effect of eccentric deployment due to calcification	CoreValve™	PIV
	Salmonsmith, 2019, [43]	Assess the hemodynamic impact of commissural alignment between the THV and native valve	Generic TAVI model	High-Speed Video & Pressure transducers
	Pott, 2021, [44]	Analyze the effect of implantation depth and cardiac output on neo-sinus flow	CoreValve™	PIV & Flow probes
	Pietrasanta, 2022, [45]	Characterize turbulent flow structures downstream of the valve at different depths	Generic TAVI Model	Tomo-PIV (3D Volumetric Velocimetry)
2	Kovarovic, 2021, [46]	Compare standard ISO 5840 testing against patient-specific anatomies	Edwards SAPIEN 3	PIV & Hydrodynamic assessment
	Borowski, 2022, [50]	Validate numerical FSI models for thrombosis prediction	Simplified TAVI Model	PIV
	Sadat, 2023, [48]	Assess how the stiffness of the test chamber affects valve expansion and function	Portico (Abbott) / Evolut (Medtronic)	Fluoroscopy & Hydrodynamics
3	Ncho, 2023, [49]	Evaluate the impact of native leaflet laceration	Edwards SAPIEN 3	Dye Injection (Washout time) & PIV

Cluster 1 = Impact of Deployment Configuration and Procedural Variables.
Cluster 2 = The Role of Anatomical Realism and Boundary Conditions.
Cluster 3 = Assessment of Thrombotic Risk and Neo-Sinus Hemodynamics.

Table 2.2: Summary of selected experimental TAVI/TAVR studies, grouped by cluster.

2.6 Computational studies on TAVI

In the last decade, computational models have become a central tool for understanding the hemodynamic and structural performance of TAVI. Starting from pure computational fluid dynamics (CFD) analyses of aortic root flow, the field has evolved towards fully coupled FSI models that account for real-

istic leaflet and stent deformation, patient-specific anatomy, and deployment mechanics. These models are increasingly used to interpret complications such as PVL, thrombosis, and aortic wall damage, and in several cases have been calibrated or validated against in-vitro or clinical data.

2.6.1 Typical computational workflow for TAVI simulations

Although implementations differ across groups and software environments, most state-of-the-art TAVI studies follow a broadly similar sequence of steps:

1. Image acquisition and anatomical reconstruction

The starting point is almost always pre-procedural imaging, typically contrast-enhanced computed tomography, sometimes supplemented by three-dimensional echocardiography or magnetic resonance imaging. From these images, a patient-specific three-dimensional model of the aortic root and surrounding structures is reconstructed [19] [51]. The segmentation usually delineates:

- LVOT;
- aortic annulus and valve leaflets (tricuspid or bicuspid);
- calcific deposits on the leaflets and annulus;
- sinuses of Valsalva and sino-tubular junction;
- a segment of the ascending aorta;
- and, when relevant, the coronary ostia.

In some studies the anatomy is not strictly patient-specific but anatomically realistic, built by morphing a reference geometry and superimposing different calcification patterns to systematically study their influence on device performance [52] [22].

2. Device and tissue modelling

Parallel to anatomical reconstruction, the THV and surrounding tissues are modelled as deformable bodies:

- The stent frame geometry is obtained either from manufacturer CAD, from reverse engineering of in-vitro devices, or from published descriptions of commercial valves; the metallic frame is usually discretised with beam or solid finite elements [22] [19] [21].
- The prosthetic leaflets are represented as thin shells or solid membranes attached to the frame. Their geometry may follow the actual device design or use idealised symmetric leaflets. Material models are typically hyperelastic and often anisotropic to capture the preferential circumferential stiffness due to collagen fibres in pericardial tissue [22] [53] [54].
- The aortic wall and LVOT are included as a thick shell or solid domain surrounding the frame. In many works this wall is treated as an isotropic hyperelastic material, a simplification of the true anisotropic, fibre-reinforced structure of the aortic root. Some studies assume a rigid wall to reduce computational cost, especially when the focus is on leaflet behaviour and transvalvular haemodynamics rather than wall mechanics [55] [56] [52] [57].
- Calcifications are commonly segmented as separate solid regions with much higher stiffness than the surrounding tissue, often modelled as linear elastic materials with large Young's modulus [22] [19] [51].

In addition, some advanced models include residual native leaflets explicitly, particularly in bicuspid anatomy, so that contact between the prosthesis, native leaflets, and calcifications can be resolved.

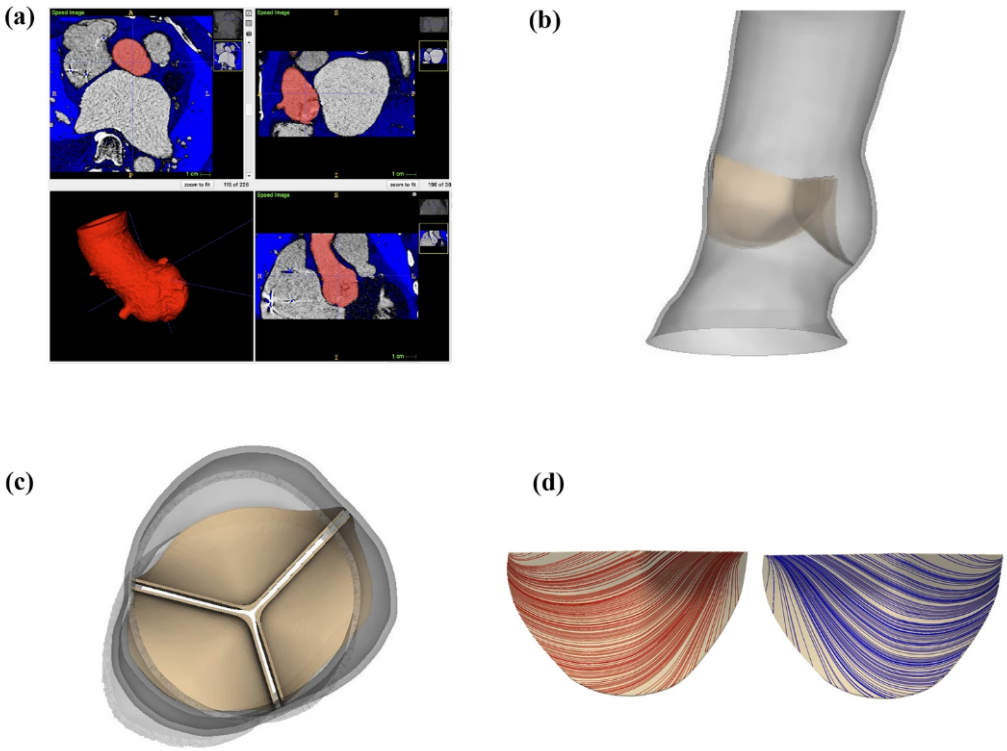

Figure 2.16: Patient-specific three-dimensional aortic root geometry from computed tomography image data. (a) Identification of patient-specific aortic root geometry through semi-automated image segmentation. (b) Reconstructed aortic root geometry. (c) Native AV geometry. (d) Native AV model fiber architecture (from Ref [19]).

3. Virtual deployment

The next step is the simulation of device deployment within the reconstructed anatomy. Nearly all groups use finite element (FE) solid mechanics for this phase, although the details differ between self-expanding and balloon-expandable devices. In most current workflows, this deployment phase is treated as a quasi-static structural problem, with blood represented either by a uniform internal pressure or neglected altogether. Only a few studies have attempted to embed deployment into a fully coupled FSI framework, largely due to the significant added computational cost and numerical complexity [19] [58] [53]. The result of deployment is a patient-specific deformed configuration of stent, leaflets, wall, and calcifications. This configuration is then used as the refer-

ence state for subsequent functional FSI simulations.

4. Post-implantation functional FSI simulations

Once the device has been virtually implanted, the post-operative functional phase is simulated over one or more cardiac cycles. Here the focus shifts to fluid–structure interaction between blood, prosthetic leaflets, and (optionally) the aortic wall. The computational domain for the fluid encompasses: the LVOT up to a plane below the native leaflets, the region enclosing the prosthetic valve and residual native tissue, the sinuses of Valsalva and ascending aorta, and, in some studies, the coronary ostia and proximal coronary arteries. The structural domain includes the deployed stent frame and bioprosthetic leaflets, and, depending on the modelling choices, the aortic wall and residual native leaflets. The interaction at the fluid-solid interface is handled by either a body-fitted moving mesh (ALE) or an immersed boundary formulation.
Researchers commonly simulate one to three cardiac cycles, often discarding the first to allow transients to decay and approximate a periodic steady state. The solutions provide detailed, time-resolved fields of velocity, pressure, stress, and strain, from which clinically relevant metrics can be extracted.

5. Post-processing and validation

After the FSI computation is completed, post-processing is the step where raw numerical fields (pressure, velocity, leaflet displacement, stresses, interface forces) are translated into clinically meaningful quantities of interest (QoIs). In TAVI, this translation is not only a visualization task: it is the point where the simulation becomes evidence, because the quantities extracted are exactly those used to support the aims of the study (e.g., comparing implantation depths, identifying PVL pathways, assessing hemodynamic performance and potential thrombogenic environments). Typical QoIs include transvalvular pressure drop (peak/mean), EOA, paravalvular regurgitant volume and jet location, leaflet kinematics (opening area vs time, closure timing), wall shear stress distributions and flow-stasis/residence-time indicators, and structural metrics such as peak principal stress in the leaflets or contact pressure pat-

terns at the annulus.
From a credibility standpoint, this step is also where the model must be framed according to verification and validation principles, because post-processing defines what the model is actually claiming to predict. This is consistent with the logic of ASME V&V 40, which is built around the idea that model credibility cannot be stated in absolute terms: it must be evaluated relative to a specific Context of Use (CoU) and to the consequences of using the model to support a decision.

2.6.2 FSI strategies

At the heart of these simulations lies the FSI coupling between blood and deformable structures. The blood flow is usually modelled as a viscous incompressible fluid, governed by the Navier-Stokes equations:

$$\rho_f \left(\frac{\partial \mathbf{u}}{\partial t} + \mathbf{u} \cdot \nabla \mathbf{u} \right) = -\nabla p + \mu \nabla^2 \mathbf{u} + \mathbf{f},$$

$$\nabla \cdot \mathbf{u} = 0.$$

where ρ_f is the fluid density, $\mathbf{u}$ the velocity field, p the pressure, μ the dynamic viscosity, and $\mathbf{f}$ represents body forces.
The deformable solids (stent, leaflets, wall) are described in a Lagrangian frame through the balance of linear momentum:

$$\rho_s \frac{\partial^2 \mathbf{d}}{\partial t^2} = \nabla \cdot \mathbf{P} + \mathbf{b},$$

where ρ_s is the solid density, $\mathbf{d}$ the displacement, $\mathbf{P}$ the first Piola-Kirchhoff stress tensor determined by the chosen constitutive law, and $\mathbf{b}$ the body-force density per unit reference volume.
At the fluid–solid interface, kinematic and dynamic continuity conditions are enforced:

- the fluid velocity equals the solid interface velocity,
- tractions are balanced: the fluid Cauchy stress $\boldsymbol{\sigma}_f$ and the solid Cauchy

stress $\boldsymbol{\sigma}_s$ satisfy

$$\boldsymbol{\sigma}_f \, \mathbf{n} = \boldsymbol{\sigma}_s \, \mathbf{n} \quad \text{along the interface normal } \mathbf{n}.$$

These coupled equations are discretised in space and time and solved numerically under the chosen FSI approach.
In FSI simulations, monolithic and partitioned approaches represent two different strategies for coupling the fluid and structural domains.
In the monolithic approach, the governing equations of the fluid and the solid are assembled into a single fully coupled system and solved simultaneously, which generally ensures a more consistent treatment of the fluid–structure interface and a greater numerical robustness, especially in strongly coupled problems.
By contrast, partitioned approaches solve the fluid and structural subproblems separately and exchange interface data iteratively at each time step, making it possible to reuse existing CFD and finite-element solvers and therefore offering greater modularity and easier integration into established computational workflows. However, this flexibility comes at the cost of a stronger sensitivity to coupling instabilities, relaxation strategies, and convergence settings, particularly in hemodynamic applications where fluid and solid densities are comparable and the added-mass effect becomes relevant.
The literature suggests that there is no universally optimal strategy for all FSI problems: Degroote et al. [59] reported that the relative performance of monolithic and partitioned schemes is problem-dependent, with partitioned simulations ranging from faster to significantly slower than monolithic ones depending on the benchmark and solver configuration. Nevertheless, when the interaction becomes stronger, the balance tends to shift in favor of monolithic formulations. In cardiovascular applications, this tendency is even more evident: Bucelli et al. [60], in a systematic comparison for cardiac FSI, concluded that monolithic schemes were significantly more robust and computationally efficient than fully coupled partitioned ones, while Ha et al. [61] showed that, in blood-vessel simulations, monolithic methods achieved faster convergence, lower CPU times, and better stability, whereas partitioned schemes could stagnate or even diverge under stronger fluid–structure interaction. Overall, parti-

tioned approaches remain attractive for their modularity and practical implementation, but current evidence indicates that monolithic methods are generally preferable for strongly coupled cardiovascular FSI problems because of their superior stability, robustness, and computational efficiency.

2.6.3 ALE versus immersed boundary formulations

Beyond the coupling strategy, an important modelling choice in fluid–structure interaction concerns how the fluid domain is represented and how the moving fluid–solid interface is tracked. The two main approaches are the arbitrary Lagrangian Eulerian (ALE) method and immersed methods.

In the present work, the simulations were performed in COMSOL Multiphysics, which relies on an ALE formulation for FSI problems. In ALE methods, the fluid domain is discretised with a body-fitted mesh that deforms in time to follow the motion of the structure. This provides a sharp description of the fluid–solid interface, which is advantageous when accurate estimates of pressure distribution, leaflet loading, and wall shear-related quantities are required. For TAVI post-implantation functional analyses, where the valve is already deployed and the motion is relatively moderate compared with the deployment phase, ALE represents a suitable and widely used choice. In this context, it allows an accurate description of leaflet kinematics and local haemodynamics while remaining fully compatible with the numerical framework available in COMSOL.

The main limitation of ALE methods is that the deforming fluid mesh can become highly distorted when the structure undergoes large displacements or strongly localised deformations, as in crimping, release, and self-expansion of the valve. In such cases, remeshing may be required, increasing computational cost and numerical complexity. For this reason, ALE is generally more appropriate for the functional phase after deployment than for the full simulation of deployment itself.

By contrast, immersed boundary and immersed finite element methods use a fixed Eulerian mesh for the fluid and a separate moving Lagrangian representation for the structure. Since the fluid mesh does not deform with the solid, these methods are better suited to problems involving large motions, contact,

and topological changes. However, the fluid-solid interface is usually represented in a more diffuse manner, which may reduce accuracy near the wall and make the evaluation of quantities such as wall shear stress less precise.
Therefore, for the aims of the present study, namely the analysis of post-deployment valve function in COMSOL, the ALE approach was considered the most appropriate solution, whereas immersed methods are more advantageous in studies aimed at reproducing the entire deployment process. The main differences between the ALE and immersed approaches are summarised in Table 2.3.

Aspect	**ALE method**	**Immersed methods**
Fluid mesh	Body-fitted mesh that deforms with the structure	Fixed Eulerian mesh; structure moves through the fluid grid
Interface representation	Sharp and well-resolved fluid-solid interface	Interface usually spread over a few grid cells
Main advantage	High accuracy near the wall; suitable for pressure and shear-related quantities	Robust for large motions, large deformations, and contact
Main limitation	Mesh distortion under large displacements may require remeshing	Lower near-wall accuracy and more complex coupling treatment
Typical use in TAVI	Post-deployment functional analysis	Deployment, crimping, self-expansion, large structural motions

Table 2.3: Comparison between ALE and immersed approaches for TAVI FSI simulations.

2.6.4 Modelling assumptions

TAVI FSI models inevitably rely on simplifying assumptions to make the problem tractable while capturing the essential physics.
In most TAVI simulations, blood is treated as an incompressible Newtonian

fluid, with constant dynamic viscosity $\mu \approx 3\text{–}4\,\mathrm{mPa \cdot s}$ and density $\rho_f \approx 1050\,\mathrm{kg/m^3}$. This approximation is generally justified in the high shear-rate regime encountered through stenotic or prosthetic valves, where non-Newtonian effects (e.g. shear-thinning) are less pronounced.
Turbulence modelling is another important choice. Fully resolved direct numerical simulation is untenable at physiologic Reynolds numbers. Many TAVI FSI studies assume a laminar flow regime, relying on the spatial and temporal resolution of the numerical mesh to capture transitional features where necessary.
The choice of constitutive laws for the various solid components strongly influences predicted stresses and deformations.

- Stent frame: self-expanding nitinol frames are usually modelled with superelastic constitutive laws capturing the austenite-martensite phase transformation and associated plateau stresses. Balloon-expandable frames made of stainless steel or cobalt-chromium alloys are often modelled as elastoplastic materials with isotropic hardening, so that permanent deformation during balloon expansion and subsequent elastic recoil are reproduced.

- Prosthetic leaflets: bioprosthetic leaflets are typically represented using nonlinear hyperelastic models

- Aortic wall and LVOT: because patient-specific material properties are rarely available, the wall is commonly assigned an isotropic hyperelastic behaviour with parameters drawn from *ex vivo* arterial testing. In addition, some TAVI simulations fix the aortic wall as rigid, especially when interest centres on leaflet kinematics and transvalvular haemodynamics rather than wall stresses.

- Calcifications and native leaflets: calcifications are usually modelled as linear elastic solids with much higher stiffness than the surrounding tissue but without plasticity. Native leaflets, when retained, may be assigned either a stiffened hyperelastic model or even treated as rigid bodies folded against the aortic wall.

Geometric modelling choices also entail approximations. For instance, contact between stent, wall, calcifications, and leaflets is often modelled as frictionless, which simplifies the numerical treatment and improves convergence at the cost of neglecting tangential frictional effects. Calcification morphology may be simplified, for example by smoothing small irregularities or grouping multiple nodules into larger contiguous regions, to avoid mesh pathologies while preserving the gross effect on stent expansion.
Finally, many studies limit the extent of the computational domain for numerical efficiency, including only a short segment of the ascending aorta and, frequently, omitting the coronary arteries; this can influence flow patterns in the sinuses of Valsalva and the representation of coronary perfusion.

2.6.5 Boundary conditions

Boundary conditions are critical in determining the realism of TAVI FSI simulations. They differ substantially between the deployment and functional phases and can be purely mechanical, purely haemodynamic, or a combination of both.

Deployment phase boundary conditions
In patient-specific simulations of TAVI, the deployment phase is typically modelled as a solid mechanics problem, aimed at reproducing the mechanical interaction between the prosthetic device and the surrounding anatomical structures. Boundary conditions play a key role in this phase, as they define the mechanical constraints imposed by the cardiovascular environment and the actuation mechanism of the device.
To account for the mechanical continuity with the surrounding cardiovascular structures that are not explicitly modelled, the proximal and distal ends of the reconstructed aortic root are commonly constrained in displacement. These constraints may consist of fully fixed boundary conditions or elastic support conditions, which prevent rigid-body motion while allowing physiologically plausible radial deformation of the vessel wall.
For self-expanding valve systems, stent crimping is typically achieved by prescribing inward radial displacements or by applying a pressure load through an

idealized cylindrical crimping surface. The deployment is then simulated by gradually releasing these constraints, allowing the stent to recover its nominal configuration. In the case of balloon-expandable devices, a time-dependent internal pressure is applied either to an explicit balloon model or directly to the inner surface of the stent, until the target expansion is reached, followed by pressure unloading to represent balloon deflation.

Some models also apply a background internal pressure to the root cavity (e.g. a diastolic-level pressure) during deployment, to mimic the presence of blood. In most cases, however, detailed fluid dynamics are not included at this stage.

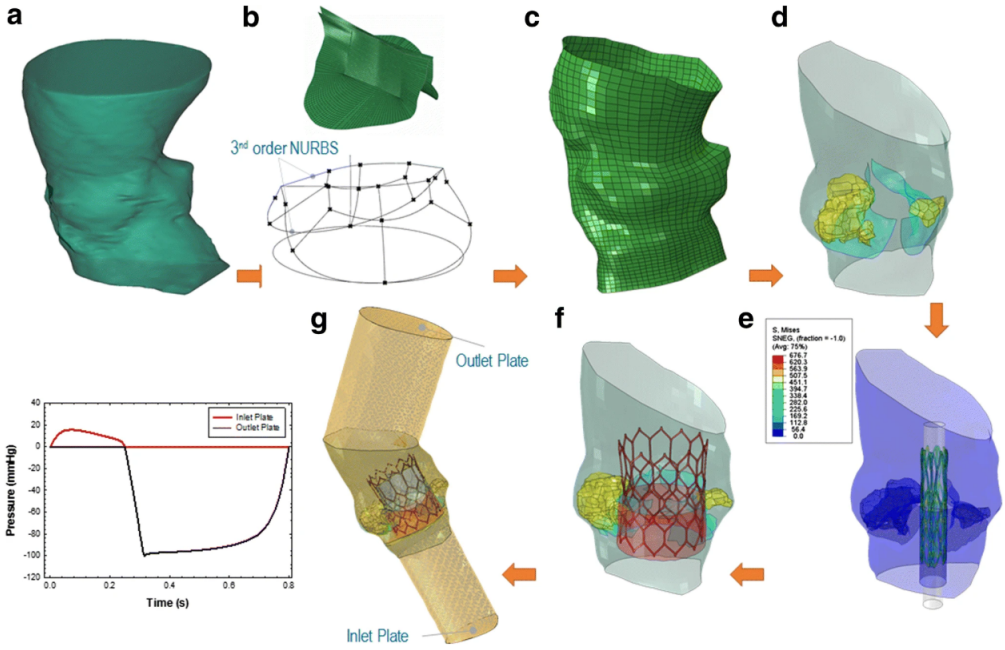

Figure 2.17: Representative computational workflow for patient-specific TAVI simulations, including geometric reconstruction (a), mesh generation (c), crimping (e) and device deployment (f) and FSI analysis(g). Boundary conditions are defined at different stages of the workflow, particularly during the deployment phase (solid mechanics) and the subsequent FSI simulations (from Ref [20]).

Functional phase boundary conditions

For the post-implantation functional phase, boundary conditions must represent the pulsatile loading of the cardiac cycle. At the inlet, corresponding to the LVOT, this is commonly achieved either by imposing a time-varying flow rate

waveform $Q(t)$, typically derived from literature data or Doppler echocardiography and characterized by a systolic ejection phase with near-zero diastolic flow, or by prescribing a left ventricular pressure waveform $p_{LV}(t)$, obtained from catheter-based or population-averaged data, so that the instantaneous pressure difference between the ventricle and the aorta directly drives valve opening and closure. At the outlets, corresponding to the distal aorta and, when included, the coronary ostia, boundary conditions may consist of simple time-varying pressure profiles approximating aortic pressure or of lumped-parameter Windkessel models (two- or three-element) incorporating resistive and compliant effects to provide a more physiological representation of the systemic arterial load; separate outlet conditions can also be defined for the coronaries using prescribed flow splits, resistance models or pressure conditions, which is particularly relevant in studies addressing leaflet thrombosis or coronary obstruction, although coronary flow is still often neglected in many simulations.

2.6.6 How computational studies cluster in the literature

In recent years, computational studies based on fluid-structure interaction have shown a marked and continuous growth in the field of TAVI, reflecting the increasing need to capture the coupled hemodynamic and structural phenomena associated with device deployment and function. This rapid expansion of the literature, while demonstrating the relevance of FSI approaches, has also resulted in a highly heterogeneous body of work in terms of modeling assumptions, objectives, and levels of fidelity.

The analysis of the selected studies reveals that current computational investigations on TAVI can be systematically grouped into a limited number of macro-categories, primarily based on the scientific objective of the study, the degree of multiphysics coupling, and the level of anatomical and physiological idealization. This observation emerges consistently across recent reviews and original investigations addressing TAVI modeling strategies [22] [52] [62]. This clustering highlights not only the dominant research directions in the field, but also the underlying modeling assumptions and their inherent limitations.

(1) Device-oriented and leaflet-scale FSI studies

A first group of studies focuses on the local dynamics of the TAVI device, with particular emphasis on leaflet motion, stress-strain response, and flow-leaflet interaction. In this cluster, the valve is typically investigated in isolation or within a simplified aortic root geometry, and the primary objective is to assess mechanical performance, leaflet kinematics, or design-related hemodynamic effects [53] [21] [62].

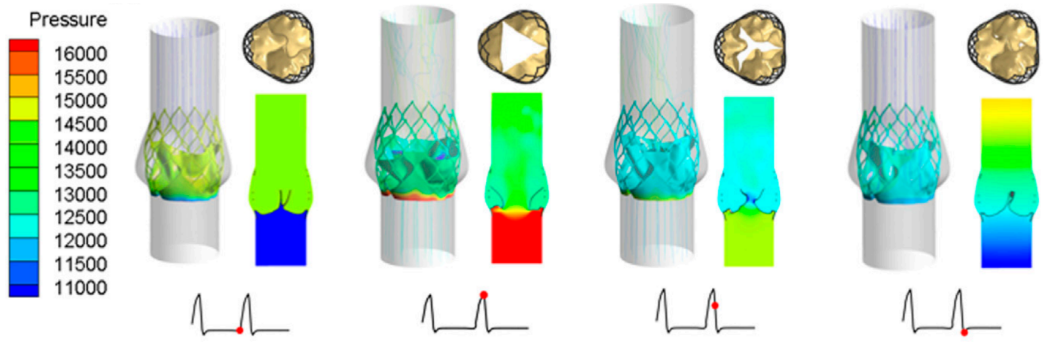

Figure 2.18: Representative leaflet opening and closing configurations of a transcatheter aortic valve, together with the corresponding pressure distributions at four distinct stages of the cardiac cycle (adapted from Ref. [21]).

These works usually implement fully coupled two-way FSI, resolving large leaflet deformations throughout the cardiac cycle. Blood is almost invariably modeled as an incompressible Newtonian fluid, while the flow regime is treated as laminar or transitional, even when high Reynolds numbers are acknowledged. The surrounding anatomy is frequently idealized: the aortic wall is commonly assumed rigid, and ventricular dynamics are either neglected or indirectly imposed through boundary conditions.
Representative studies in this cluster investigate the influence of leaflet stiffness, material anisotropy, orifice geometry, or stent-leaflet design choices on transvalvular pressure gradients, EOA, and stress distributions. While these studies provide valuable mechanistic insight into valve performance, their scope is intentionally local and device-centric. Consequently, the extrapolation of results to patient-specific or procedure-dependent scenarios remains limited.

(2) Patient-specific FSI frameworks for clinical assessment

A second cluster comprises studies that aim to enhance clinical predictability by employing patient-specific geometries reconstructed from medical imaging. These works typically include detailed representations of the aortic root, native leaflets, calcifications, and deployed TAVI devices, and they apply FSI to evaluate post-implantation hemodynamics, leaflet coaptation, and PVL [22] [52].

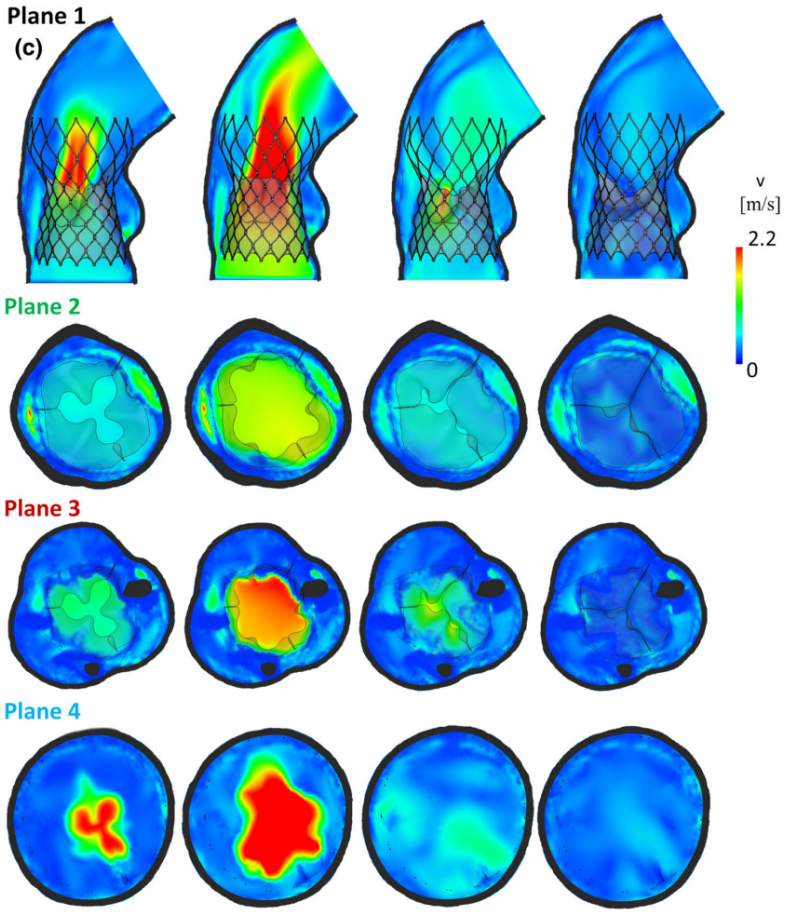

Figure 2.19: Contours of blood velocity magnitude in four representative planes of the fluid domain within a patient-specific aortic root model (adapted from Ref. [22]).

In this category, FSI is used not only as a design-analysis tool but as a clinical decision-support methodology. Boundary conditions are often derived from patient data, such as Doppler-measured velocities or pressure waveforms, and numerical predictions are compared against post-operative CT or echocardio-

graphic measurements, providing application-level validation of the modeling framework.
However, the increased anatomical realism comes at a substantial computational cost. To maintain numerical tractability, these models frequently adopt simplifying assumptions, including rigid aortic walls, simplified constitutive laws for soft tissues, or truncated cardiac domains. As a result, while these studies represent the most clinically ambitious applications of FSI in TAVI research, they also expose the current limitations of high-fidelity patient-specific simulations for routine clinical use.

(3) Procedure- and positioning-driven studies (malpositioning, PVL, deployment effects)

A third and particularly relevant cluster focuses on procedural aspects of TAVI, including implantation depth, tilt, eccentric positioning, and underexpansion, all of which are known to critically influence post-implantation outcomes. These studies explicitly investigate how deviations from ideal deployment affect flow patterns, jet eccentricity, wall shear stress distributions, and PVL formation [52] [56] [16].
Within this group, methodological approaches are more heterogeneous. Some studies adopt two-way FSI, whereas others rely on CFD simulations on fixed post-deployment geometries, occasionally preceded by a separate structural deployment analysis. Despite this variability, the unifying feature of the cluster is the emphasis on relative comparisons between deployment scenarios, rather than absolute physiological accuracy.
Across this cluster, blood is consistently modeled as Newtonian, and turbulence is generally treated implicitly through transient simulations without explicit turbulence models. The aortic root is most often considered rigid, reflecting a deliberate trade-off between physiological realism and numerical robustness. Importantly, these works demonstrate that malpositioning alone, even in idealized geometries, can induce substantial hemodynamic alterations, thereby justifying controlled parametric investigations that isolate deployment effects from patient-specific anatomical variability.

Other studies

There are some studies that reside at the boundary between FSI and CFD, often referred to as hybrid or weakly coupled approaches. These works typically involve structural simulations to obtain a deployed valve configuration, followed by CFD analyses of the resulting flow field, or they impose prescribed leaflet positions without dynamically resolving structural deformation [16] [62]. Although such approaches do not constitute full FSI in a strict sense, they remain prevalent in the literature due to their computational efficiency and their suitability for extensive parametric studies. They are particularly common in investigations of washout flow, thrombosis-related metrics, and coronary hemodynamics, where capturing fine-scale flow features is prioritized over structural feedback effects [52].

The widespread adoption of these simplified frameworks underscores a recurring theme in the literature: for many clinically relevant questions, especially those related to comparative assessment of deployment scenarios, the marginal benefit of full two-way FSI may not always justify its computational cost [22].

Cluster	Ref.	FSI	Software	TAVI device	P.I.	Flow Hyp.	AR Hyp.
1	Luraghi, 2019, [22]	FE	LS-DYNA	Evolut™ (29 mm)	PVL, stress, velocity	–	Anisotropic hyperelastic
	Govindarajan, 2022, [51]	FE	3D-FSI algorithm	TAVR (23 mm)	Velocity, Pressure, WSS	Transitional	–
	Fumagalli, 2023, [57]	ALE	In-house solver	Edwards SAPIEN XT (23 mm)	Velocity, Pressure, WSS	Laminar	Rigid
	Brown, 2023, [19]	IFED	IBAMR	Evolut R™	EOA, ΔP	–	Rigid
2	Kandail, 2018, [52]	ALE	ANSYS + Abaqus	CoreValve™ (29 mm)	Velocity, WSS, Pressure	Laminar	Rigid
	Tango, 2025, [63]	ALE	LS-DYNA	TAVR (idealised)	Velocity, pressure, EOA	–	Linear elastic
	Basri, 2020, [56]	Two-way FSI	ANSYS	Edwards SAPIEN XT (26 mm)	Velocity, Pressure, WSS	Turbulent	Linear elastic
	Liu, 2022, [21]	ALE	Abaqus + LS-DYNA	TAV stent (3 designs)	Velocity, pressure	Laminar	–
	Oks, 2022, [55]	ALE-IBM	In-house solver	TAVR	EOA, ΔP, stress	–	Rigid
3	Mao, 2016, [53]	SPH–FE FSI	Abaqus/ Explicit	TAV (generic)	Leaflet stress, Velocity, Pressure	–	Rigid
	Wu, 2019, [58]	Immerso-geometric FSI	In-house IGA framework	TAVI (full device)	Anchoring forces, Velocity	Laminar	Rigid
OS	Pil, 2023, [54]	ALE	COMSOL Multi-physics	TAVI (idealised, 2D)	Velocity, WSS, Pressure, EOA	–	Rigid
	Catalano, 2025, [64]	SPH	Abaqus	Edwards SAPIEN 3 Ultra	Velocity, Pressure, EOA	Laminar	Hyperelastic
	Wald, 2018, [62]	ALE	ADINA	CoreValve™	Velocity, Pressure, Flow	Laminar	–

Cluster 1 = patient-specific and procedure-oriented fluid–structure interaction studies.
Cluster 2 = post-implantation hemodynamic and complication-focused studies.
Cluster 3 = methodological and numerical fluid–structure interaction studies.
OS = other studies, i.e. complementary computational works not belonging to the three main thematic clusters.
P.I. = parameters of interest; Flow Hyp. = flow hypothesis; AR Hyp. = aortic root hypothesis.

Table 2.4: Summary of selected computational TAVI studies with FSI assumptions.

In the reviewed TAVI-focused computational studies, credibility assessment is highly heterogeneous and only a subset of works explicitly addresses Verification and Validation (V&V) in a structured manner. A first group includes studies that perform formal V&V steps, [55], who explicitly report verification and validation of their two-way FSI solver against the widely used Turek–Hron FSI3 benchmark and additionally contrast ISO 5840-3–inspired performance quantities (e.g., geometric orifice area and transvalvular pressure gradient) against published experimental trends. A second group achieves application-level validation by direct comparison with measured data: apply a patient-specific two-way FSI workflow to two clinical cases and compare predicted device configuration and hemodynamics with post-operative CT and Doppler measurements, reporting qualitative and quantitative agreement for PVL-related metrics [22]. Similarly, in-vitro validation is reported in benchmark-type TAVI FSI investigations (e.g., percutaneous valve models compared against mock-loop data) [63]. However, many contributions provide mainly numerical verification (e.g., mesh-sensitivity or grid-convergence tests) without a full experimental/clinical validation campaign [53]. In addition, some recent patient-specific FSI frameworks explicitly acknowledge that substantial validation is still pending and is planned as future work via dedicated in-vitro measurements (e.g., PIV, pressure/flow acquisition, leaflet kinematics) [19].

Overall, the reviewed literature demonstrates that fluid–structure interaction modeling is a powerful and necessary tool to capture the coupled hemodynamic and structural mechanisms governing TAVI performance. However, the analysis also reveals a persistent lack of controlled and systematic investigations specifically addressing implantation malpositioning under physiologically consistent boundary conditions. This gap motivates the present thesis, which adopts an FSI-based framework to isolate and quantify the hemodynamic consequences of non-ideal TAVI positioning in a controlled and reproducible setting, focusing on the systolic phase.
From a clinical and hemodynamic perspective, focusing specifically on the valve opening phase remains meaningful even when the full cardiac cycle is not reproduced. As discussed throughout this chapter, the onset of systole is

the phase in which leaflet opening, transvalvular pressure gradient, EOA, and early jet development are established, thereby directly affecting the forward-flow performance of the implanted device. Moreover, several studies reviewed above show that implantation-related factors such as depth, alignment, and other non-ideal deployment conditions can substantially alter flow patterns, jet eccentricity, wall shear stress, and sinus hemodynamics. Therefore, although a complete-cycle analysis would be required to fully address diastolic phenomena such as regurgitation or long-term washout, the isolated investigation of the opening phase still provides clinically relevant information on the immediate functional consequences of TAVI malpositioning and constitutes a justified first step toward more comprehensive analyses.

Chapter 3

Methods

This chapter describes the methodological framework adopted to investigate the FSI behavior of transcatheter aortic valve configurations under physiologically relevant conditions. The numerical workflow was progressively developed, starting from simplified tutorial-based models to validate solver settings and mesh-handling strategies, and subsequently extended to anatomically realistic geometries derived from laboratory CAD files. Particular attention was devoted to ensuring geometric consistency with the experimental platform available at the CAVE Lab, enabling the definition of a computational model suitable for controlled comparative analyses and future in silico–in vitro validation. The chapter details the numerical formulation, geometry preparation, material modeling assumptions, boundary conditions, solver configurations, and case-study definitions adopted throughout the study.

3.1 Numerical framework for FSI simulations in Comsol

FSI modelling has become a well-established computational approach for the analysis of heart valve (HV) mechanics and cardiovascular hemodynamics. In this context, FSI enables the simultaneous resolution of blood flow dynamics and structural deformation of valve leaflets, allowing a realistic description of valve opening, closing, stress distribution, and flow patterns under physiological and pathological conditions.

A large number of previous studies have adopted FSI techniques to investigate native and pathological heart valves, including healthy, stenotic, bicuspid, and prosthetic configurations [65] [66] [54]. Most of these works rely on FE-based formulations coupled with computational fluid dynamics, often implemented through an ALE framework to account for the large deformations of valve leaflets while preserving mesh quality in the fluid domain [67] [68]. Although modelling assumptions vary across studies, the literature shows a widespread use of simplified constitutive laws for valve tissues, most commonly linear elastic isotropic models, especially in two-dimensional simulations [69] [65] [70]. More recent contributions have explored isotropic and anisotropic hyperelastic formulations and patient-specific three-dimensional geometries, highlighting the sensitivity of hemodynamic and mechanical results to the adopted material model and geometric fidelity [71] [66] [54].

Among the available multiphysics platforms, COMSOL Multiphysics has been extensively employed for FSI simulations of cardiovascular systems. Its FE formulation, combined with a monolithic or strongly coupled FSI solver and ALE mesh handling, makes it particularly suitable for HV applications, where fluid and structural fields are tightly coupled and evolve over time [67] [71]. COMSOL allows the direct coupling of the incompressible Navier-Stokes equations governing blood flow with the solid mechanics equations describing leaflet deformation, ensuring kinematic and dynamic continuity at the fluid–structure interface.

An additional advantage of COMSOL lies in its flexibility with respect to modelling assumptions. The software supports different levels of geometric complexity, ranging from idealized two-dimensional sections to fully three-dimensional, patient-specific models, as well as a wide range of constitutive laws for soft tissues. This flexibility has enabled its application to the analysis of valve hemodynamics, leaflet stresses, and pathological conditions such as calcific AS or congenital valve abnormalities [65] [66] [72] [54].

In this work, COMSOL Multiphysics is used as the numerical framework to perform FSI simulations of HV behavior. Overall, the COMSOL-based literature shows that, while the platform has been successfully applied to native, pathological, and prosthetic heart valves, TAVI-specific applications remain comparatively sparse. In particular, within the reviewed studies, COMSOL-

Ref.	Aim	HV Modelling	COMSOL Physics / Modules	Deformable Domains	Geometry Source	Dim.
Fedotova, 2025, [72]	AV haemodynamics under leaflet calcification / stiffness variation	Linear elastic; isotropic hyperelastic	FSI (ALE), FEM	Leaflets only	Generated native / calcified AV	3D
Pil, 2023, [54]	Effect of leaflet material model in healthy, pathological and Ozaki AV	Linear elastic; isotropic hyperelastic; anisotropic hyperelastic	FSI; k–ε RANS	Leaflets only	Idealized ultrasound-based AV	2D
Xu, 2024, [71]	Effect of leaflet / wall material properties on healthy AV mechanics	Linear elastic; Mooney–Rivlin hyperelastic	Fluid + solid + ALE + contact	Leaflets + aortic wall	Parametric native tricuspid AV	3D
Loureiro, 2020, [66]	Patient-specific biomechanical model of stenotic AV	Linear elastic	Structural mechanics + flow (not explicit)	Leaflets	Patient-specific TEE-derived AV	3D
Ghanbari, 2022, [68]	Effect of leaflet geometric design on prosthetic HV performance	Linear elastic isotropic polymer	Solid + fluid + moving mesh	Leaflets only	Parametric prosthetic HV	2D, 3D
Bahraseman 2016, [67]	Effect of AS severity and HR on CO and SV	Linear elastic isotropic	FSI + ALE	Leaflets only	Echo-derived idealized AV	2D
Alonazi, 2015, [73]	AV response / state during LVAD support	Linear elastic isotropic	FSI + ALE	AV leaflets + LV wall	Simplified / realistic LV–AV geometries	2D
Khosravi, 2014, [69]	Estimate velocity integral, SV and CO	Linear elastic isotropic	FSI + ALE	Valve cusps only	Echo-Doppler-derived AV	2D
Kuan, 2015, [65]	Modelling requirements for congenitally bicuspid AV	Linear elastic isotropic	FE + CFD + ALE	Cusps only	Idealized bicuspid AV	2D
Yeh, 2019, [74]	Valve mechanics and flow interaction in BMHV; hematocrit effects	Linear elastic isotropic	FSI + ALE	Leaflets only; wall rigid	Experimental / benchtop BMHV	3D
Esfahani, 2019, [75]	Blood flow and leaflet stresses during mitral regurgitation	Linear elastic isotropic	FSI + ALE moving mesh	Leaflets only	MRI-based simplified MV	2D
Avanzini, 2008, [70]	MV hemodynamics and leaflet stress / pressure gradient	Elastic, nonlinear geometry	Structural Mechanics + Incompressible Navier–Stokes + Moving Mesh	Leaflets only	Simplified native MV	3D

Abbreviations: MV = mitral valve; BMHV = bileaflet mechanical heart valve; LVAD = left ventricular assist device; CO = cardiac output; SV = stroke volume; AS = aortic stenosis; MR = mitral regurgitation.

Table 3.1: Summary of selected HV computational studies performed with COMSOL Multiphysics.

based TAVI investigations are still largely limited to simplified representations, whereas fully three-dimensional analyses addressing clinically relevant implantation conditions are still underrepresented. This gap motivates the present work, which develops a 3D COMSOL framework to investigate the hemodynamic effects of TAVI malpositioning in a controlled setting, with specific focus on the valve opening phase.

3.2 Preliminary tutorials

Before addressing the specific simulations developed for this thesis, a series of tutorial-based models and benchmark cases were implemented to gain familiarity with the FSI workflow, solver settings, and modelling strategies commonly adopted in the literature. These preliminary simulations provided the methodological foundation for the subsequent analyses and ensured consistency with established approaches reported in previous FSI studies of heart valves. The tutorial models are introduced here as part of the numerical development pathway, whereas their main outcomes and representative results are presented in the following chapter.

3.2.1 Tutorial 2D: Vertical structure

To become familiar with the core COMSOL ingredients needed for FSI problems (moving boundaries, mesh deformation and boundary conditions), I first reproduced a simple 2D tutorial model [76]. This preliminary exercise was meant as a training case before moving to the full 3D model developed later in this work, and it was designed to clearly show how a laminar flow can deform a flexible structure and how the flow solution can be maintained in a continuously deforming domain using the ALE approach.
The tutorial geometry consists of a straight horizontal micro-channel with a vertical flexible obstacle placed inside the flow path . The channel is 300 μm long and 100 μm high. The internal obstacle has a width of 5 μm, a height of 50 μm, and a semicircular tip, and it is positioned 100 μm downstream from the inlet boundary of the channel.

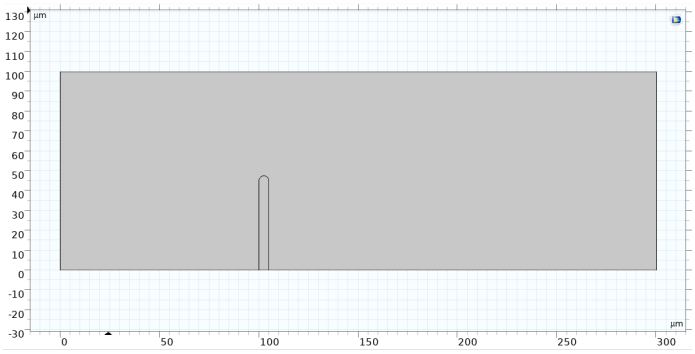

Figure 3.1: Vertical structure geometry.

For the fluid domain, a water-like Newtonian fluid is assumed, with density $\rho = 1000$ kg/m^3 and dynamic viscosity $\eta = 0.001$ Pa $\cdot$ s. The vertical obstacle is treated as a deformable solid, assigned density $\rho = 7850$ kg/m^3 and Young's modulus $E = 200$ kPa, in order to generate visible deformation under the hydrodynamic load and to highlight the coupling mechanisms.
At the inlet, the flow is prescribed as fully developed laminar, i.e., a parabolic velocity profile whose amplitude varies in time. The inflow rapidly increases, reaching its peak at $t = 0.215$ s, and then decreases progressively until it stabilizes to a steady value of 5 cm/s. The centerline inlet velocity component in the x-direction, U_{in}, is defined through:

$$U_{\text{in}} = \frac{U \cdot t^2}{(0.04 - t^2)^2 + (0.1t)^2}, \tag{3.1}$$

where t is expressed in seconds and U is the steady-state amplitude.

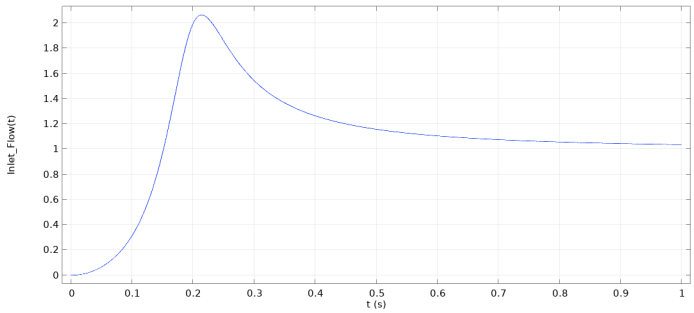

Figure 3.2: Inlet velocity.

At the outlet, a zero-pressure condition is imposed. Finally, a no-slip condition

is applied at the channel walls (non-deforming boundaries) to ensure physical adherence of the fluid to the solid boundaries.

3.2.2 Tutorial 3D: Cylindrical channel flow

After completing the introductory 2D FSI tutorial, a second intermediate tutorial was developed in order to extend the workflow to a fully three-dimensional configuration. This step was essential to become familiar with 3D geometry construction, boundary selection, solver configuration, and post-processing in COMSOL before moving to the final valve-oriented simulations.
The geometry was constructed using the built-in Cylinder function in COMSOL. A solid cylinder was defined with radius $R = 5$ mm and height $H = 15$ mm, aligned along the z-axis and centered at the origin. The cylinder represents a straight rigid channel through which an incompressible fluid flows.

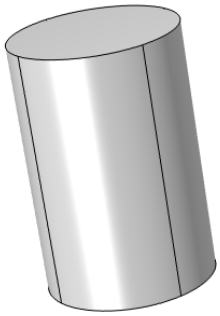

Figure 3.3: Single channel Tutorial Geometry.

The fluid domain was assigned the material Water from the COMSOL material library. Water was modeled as an incompressible Newtonian fluid with constant density and dynamic viscosity, consistent with laminar flow assumptions. The Laminar Flow physics interface was used. A constant inlet velocity was prescribed at the bottom surface of the cylinder, with magnitude:

$$u_{\text{in}} = 0.01 \text{ m/s}. \tag{3.2}$$

At the outlet (top surface), a zero-pressure boundary condition was imposed:

$$p_{\text{out}} = 0 \text{ Pa}. \tag{3.3}$$

All lateral walls of the cylinder were assigned a no-slip condition, enforcing zero velocity at the boundary. A stationary study was performed, allowing direct computation of the fully developed velocity and pressure fields.

3.3 Initial 3D Aortic Valve Geometry (Casting Model)

3.3.1 CAD Assembly and Fluid Domain Extraction

Following these tutorial-based benchmark cases, the workflow was transferred to the first geometry of interest for this thesis: a three-dimensional AV model. The geometry hereafter referred to as casting corresponds to a pre-existing laboratory model that had already been used in previous studies at the CAVE Lab at Aarhus University. The adopted nomenclature reflects the origin of the geometry, which was initially obtained from a physical cast manufactured in the laboratory. In the present thesis, the CAD model of this geometry, including the AV and the sinus of Valsalva, was provided and used as the baseline configuration for the subsequent analyses.

This step marks the transition from controlled training configurations to the anatomical domain relevant to TAVI simulations.

The first step in the modelling process was to extract the fluid domain from the sinus of Valsalva, as this area plays a crucial role in the aortic flow dynamics. To extract the fluid domain, I employed a thickening function within Autodesk Inventor to generate the appropriate geometry for the fluid region. This function allowed for the creation of the inner fluid boundary by thickening the surfaces of the sinus, ensuring the accurate representation of the fluid domain. Once the fluid domain was successfully defined, the valve and sinus geometries were assembled into a complete 3D model. The Assembly process involved aligning the valve and sinus components based on predefined reference points, ensuring that the geometries were properly positioned relative to

each other. This alignment was essential to ensure accurate simulations of the fluid-structure interaction in the subsequent FSI simulations.

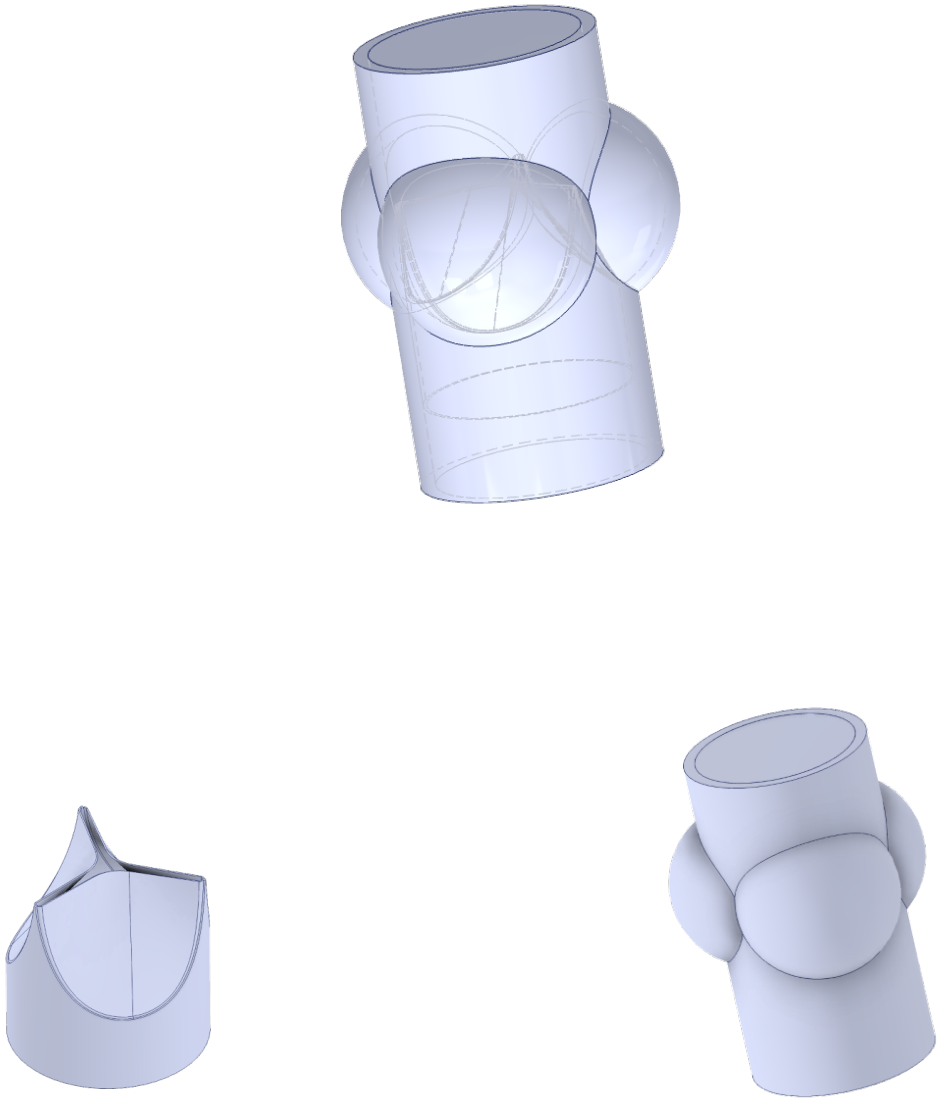

Figure 3.4: Assembled 3D geometry of the aortic valve and Valsalva sinuses (top) and individual CAD components used for the assembly (bottom).

3.3.2 Import into COMSOL and Physics Setup

Once the preliminary 3D geometry of the AV and sinus of Valsalva was completed in Autodesk Inventor and exported as an STL file, the next step involved importing the model into COMSOL Multiphysics for simulation. This allowed the system to recognize the geometry as a mesh and enabled the definition of appropriate domains for the fluid and solid regions of the model.

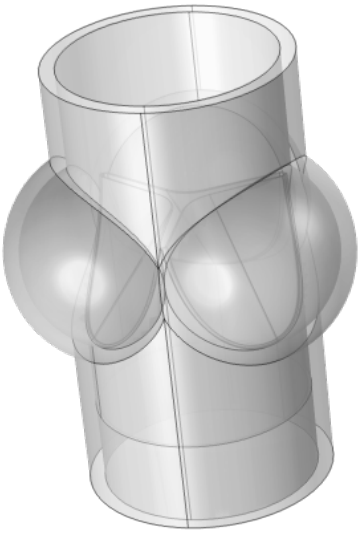

Figure 3.5: Casting geometry imported into COMSOL.

Mesh Refinement and Simulation Objectives For the initial phase of simulations, a Coarse mesh was chosen to simplify the setup and focus on the general FSI dynamics. The decision to use a coarse mesh was made to speed up the computation time and facilitate the exploration of the basic behavior of the system. This choice allowed for a more efficient investigation of the flow patterns and valve deformation without the additional complexity introduced by a finer mesh.

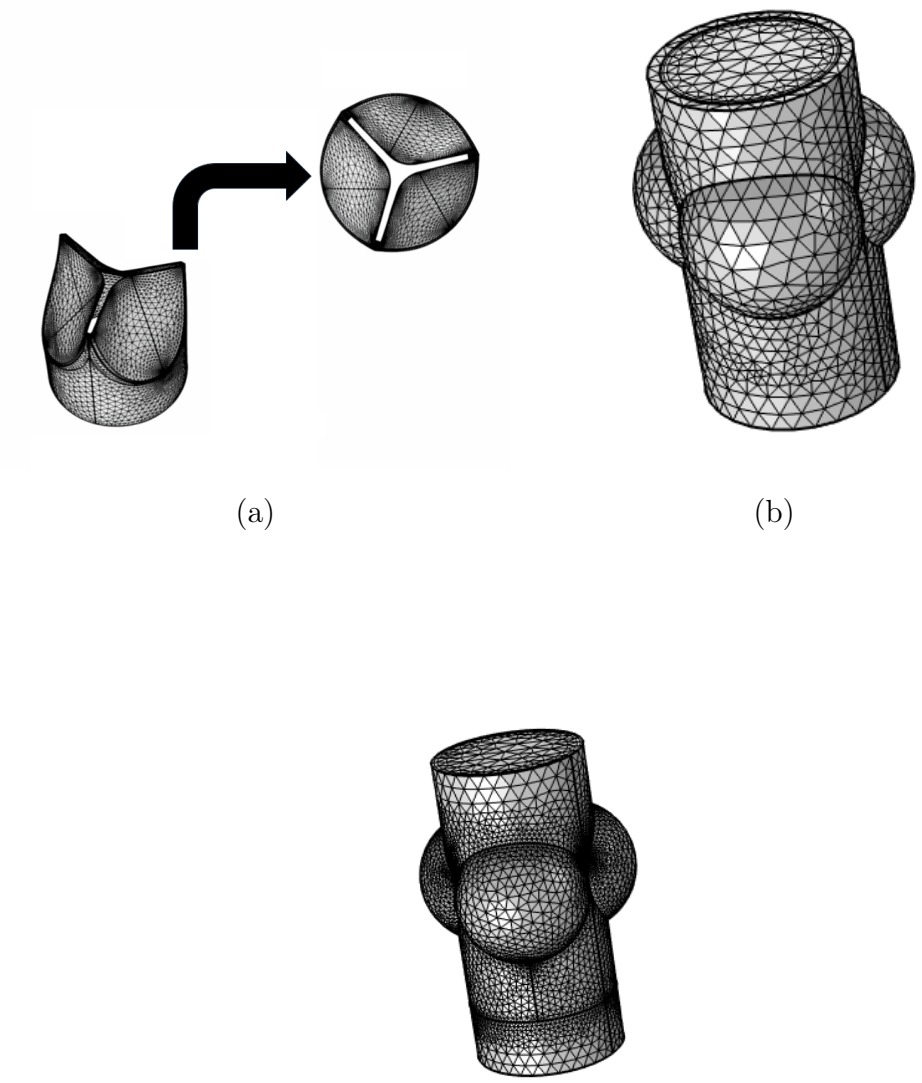

(a) (b)

(c)

Figure 3.6: Meshes of: a) the valve, b) sinus of Valsalva and c) the fluid part.

Material Assignments Material properties were assigned to the different regions of the model. The fluid domain was defined as Water, modeled as a Newtonian incompressible fluid ($\rho = 1000\ kg/m^3$, $\eta = 0.001$ Pa·s). For the solid domains (sinus of Valsalva and AV), a linear elastic constitutive model

was adopted (Table 3.2 and 3.3). Although aortic tissues typically exhibit hyperelastic and anisotropic behavior, a linear elastic approximation was employed in this preliminary phase to isolate the fundamental fluid-structure interaction mechanisms and ensure numerical convergence, consistent with simplified approaches found in the literature for initial stability assessments.

Property	**Sinus material**	**Valve material**
Density (ρ)	1200 kg/m^3	980 kg/m^3
Young's modulus (E)	2×10^9 Pa	1.2×10^6 Pa
Poisson's ratio (ν)	0.45	0.45

Table 3.2: Material properties assigned to the sinus and valve domains.

Physics Setup and Boundary Conditions After material assignments, the next step was to define the physics of the model. The Laminar Flow physics interface was used to model the incompressible fluid flow through the AV. The FSI interface was activated to enable coupling between the fluid and solid domains, allowing for the dynamic interaction between the blood flow and the valve deformation.

For the solid domains, representing the sinus of Valsalva and the AV, the Solid Mechanics interface was used to model the structural behavior of the tissue. In particular, the Fixed constraint boundary condition was applied to both the sinus of Valsalva and the walls of the AV. This ensured that the sinus and the valve walls remained stationary during the simulations, while allowing the leaflets to deform and interact dynamically with the fluid flow.

A velocity inlet condition was applied at the inflow boundary of the fluid domain, while a pressure outlet condition was imposed on the outlet boundary to simulate the outflow of blood from the AV, assuming that the downstream pressure is negligible compared to the inlet pressure.

The walls of the valve leaflets and the sinus of Valsalva were assigned a no-slip boundary condition, ensuring that the velocity of the fluid at the solid-fluid interface is zero.

To accurately capture the motion of the valve leaflets and the corresponding deformation of the fluid domain, the Moving Mesh functionality was employed in COMSOL. This approach allowed for the mesh to dynamically adapt as the

valve leaflets moved during the simulations based on the displacement of the solid structure, ensuring a high-quality mesh at all times.

Simulation Setup and Variable scaling For the simulations, a Fully Coupled Solver was employed. This approach was preferred over the Segregated Solver because it directly couples the fluid and structural equations, solving them simultaneously at each iteration. This is particularly advantageous for FSI problems, where the interaction between the fluid and the structure is strongly dependent on both domains. Using a segregated approach, where the fluid and solid equations are solved sequentially, can lead to slower convergence and less accurate results, especially when the fluid–structure interaction is strong and the mesh undergoes significant deformation. The Fully Coupled Solver, on the other hand, allows for a more efficient and accurate solution, particularly in simulations involving large deformations and complex interactions.

Given the strong nonlinearities of the coupled problem, the nonlinear solution method was set to Automatic Newton in COMSOL. This option was adopted to improve the robustness of the iterative procedure in the presence of large deformations, moving-mesh effects, and strong fluid–structure coupling.

To solve the resulting system of equations, a Direct Solver was used, specifically the PARDISO solver available in COMSOL. This solver was chosen because it provides highly efficient and accurate solutions for large sparse systems and is particularly well suited for problems with complex geometries and high computational demands, offering significant advantages over iterative solvers for this class of applications. It is also more reliable when handling systems with a high degree of nonlinearity, which is common in FSI problems due to the coupled nature of fluid flow and structural deformation.

To facilitate convergence in this complex multiphysics environment, a relative tolerance of 0.1 was applied.

Additionally, variable scaling was introduced to ensure that the solution process converged efficiently. Scaling is crucial in numerical simulations, especially in models involving physical quantities with very different orders of magnitude, such as pressure and displacement. Without scaling, certain variables may dominate the solution process, leading to poor convergence or even diver-

gence. By applying appropriate scaling factors, the relative magnitude of the variables is adjusted so that each term in the system of equations contributes more consistently to the numerical solution. This improves both the stability and the convergence rate of the solver. Based on the expected physical magnitudes of the problem, the following characteristic scales were enforced:

- Pressure: $1 \times 10^3\,\mathrm{Pa}$
- Velocity field: $1\,\mathrm{m/s}$
- Displacement field (structure and mesh): $1 \times 10^{-3}\,\mathrm{m}$

Several simulations were performed and carried out in different phases, evolving from steady-state models to time-dependent simulations, as described below:

- Steady-State Simulations with Pressure Boundary Conditions
  Initially, steady-state simulations were run using a constant pressure boundary condition at the inlet, while a zero-pressure condition was set at the outlet. These simulations were designed to examine the flow and pressure fields under relatively simple conditions, with the goal of understanding the general flow behavior in the system.

- Time-Dependent Simulations with Pressure Ramp
  In the second phase, time-dependent simulations were performed to simulate a more realistic pressure profile at the inlet. A ramp function was applied to gradually increase the pressure over time, mimicking the dynamic changes in pressure that occur during the cardiac cycle. This allowed for the analysis of transient fluid-structure interaction and provided a deeper understanding of how the AV and sinus behave under varying pressure conditions.

- Steady-State Simulations with Cardiac Cycle Curves
  In the third phase, more complex boundary conditions were used, including a time-varying velocity waveform imposed at the inlet and an aortic pressure curve applied at the outlet. These steady-state simulations aimed to reproduce a more physiologically representative scenario

for the AV, with the fluid domain subjected to boundary conditions derived from experimental measurements collected at the CAVE Lab.
The inlet velocity and outlet pressure curves adopted in this phase are shown in Figure 3.7. These curves were used as the reference source from which the inlet–outlet pairs of values were extracted at selected time instants along the cardiac cycle and then imposed in the sequence of concatenated steady-state studies.
For this phase, multiple steady-state studies were concatenated, each corresponding to a different time instant of the cardiac cycle. At each step, a specific pair of inlet velocity and outlet pressure values was assigned, so as to reproduce the temporal evolution of the loading conditions during systole and diastole. In this way, the boundary conditions were progressively updated to reflect the changing hemodynamic conditions, allowing a more detailed evaluation of the valve response under experimentally informed loading.

- Time-Dependent Simulations of the Opening Phase
  An additional set of simulations was performed through a time-dependent study restricted to the valve opening phase. The transient boundary conditions were defined using only the systolic portion of the inlet velocity waveform and outlet pressure curve shown in Figure 3.7, rather than the entire cardiac-cycle profiles. In this way, the two curves were applied directly in time-dependent form only over the opening interval, allowing the progressive development of leaflet deformation and transvalvular flow to be analysed during the initial systolic phase.

- Steady-State Contact Analysis
  An additional steady-state study was carried out on the ideal casting geometry to investigate leaflet contact under simplified loading conditions. In this case, three leaflet–leaflet contact pairs were defined in COMSOL in order to model the interaction between adjacent leaflets during closure. To improve the numerical robustness of the contact formulation and prevent solver failure, a small artificial gap of 5×10^{-6} m was introduced between adjacent leaflets. The simulation was performed with 0 Pa at the inlet and 12000 Pa at the outlet, so as to promote leaflet

coaptation under an imposed adverse transvalvular pressure gradient.

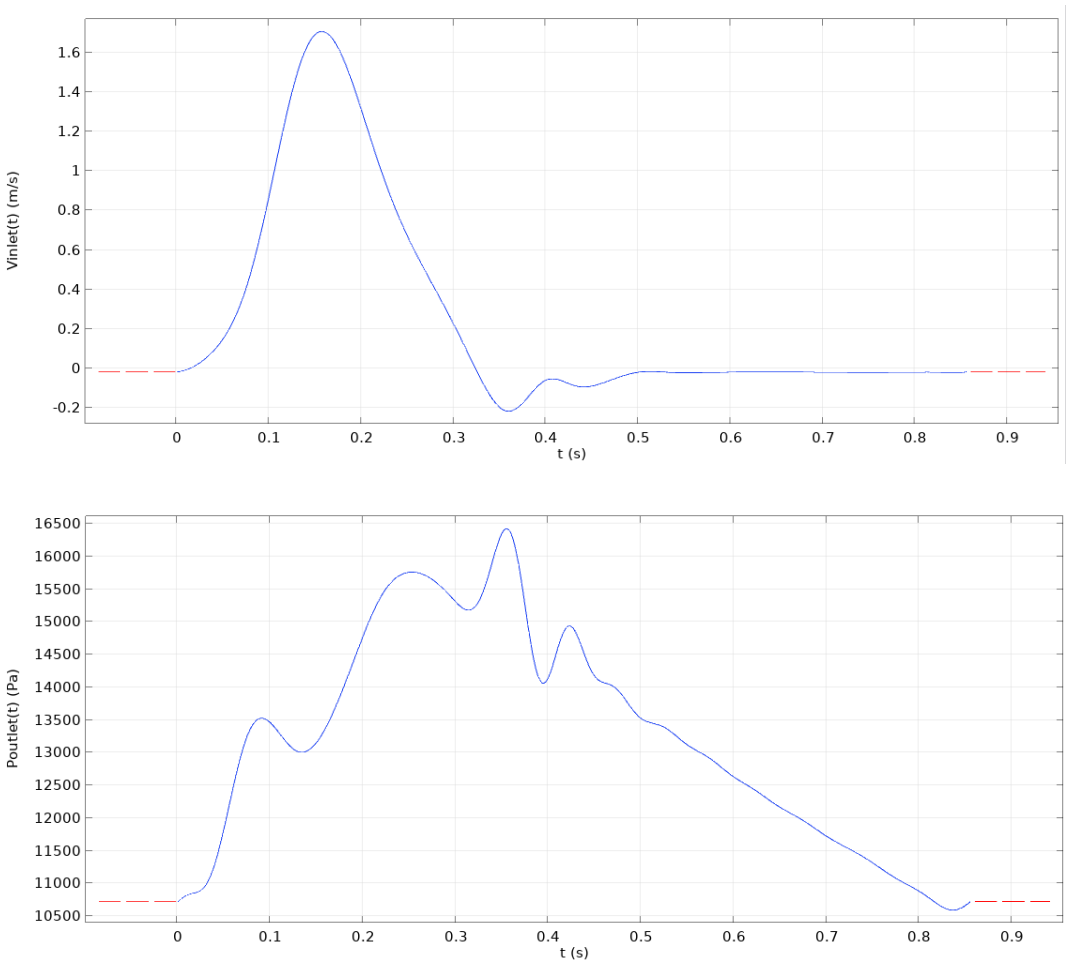

Figure 3.7: Inlet velocity waveform and outlet aortic pressure curve used to extract the boundary-condition pairs for the concatenated steady-state simulations.

Throughout these phases, a detailed table was kept to track the changes in boundary conditions, simulation settings, and solver configurations providing a comprehensive overview of the parameters used in each simulation phase. The complete table can be found in the appendix A, where it serves as a reference for the simulations performed.

3.4 Final Modular TAVI Model

3.4.1 Geometric Reconstruction from Experimental CAD

To ensure high geometric fidelity with the in-vitro platform, the final computational domain was derived directly from the original CAD files used for the mock loop construction. These CAD geometries were provided by the CAVE Lab at Aarhus University and correspond to the same models employed in the related laboratory activities. Importantly, the computational model implemented in COMSOL is based on the same aortic root geometry tested experimentally, thereby providing a structured basis for future in silico-in vitro validation activities.

Although experimental data were not used for validation within the scope of this thesis, the experimental campaign included high-speed camera acquisitions aimed at capturing valve kinematics. These recordings can be exploited to compare leaflet opening dynamics and EOA between numerical predictions and mock-loop observations.

From a manufacturing perspective, the stent structure and the Valsalva region were fabricated using clear resin, while the valve leaflets were produced in silicone (Shore 40A) to reproduce compliant behavior. The mock loop was operated using water as working fluid and driven by a ViVitro pulsatile pump to reproduce controlled pulsatile conditions.

A representative image of the experimental setup is provided in Figure 3.8. More specifically, the figure shows a zoomed view of the portion of the mock loop in which the valve was inserted. For completeness and reproducibility, detailed specifications of the experimental setup are reported in Appendix B.

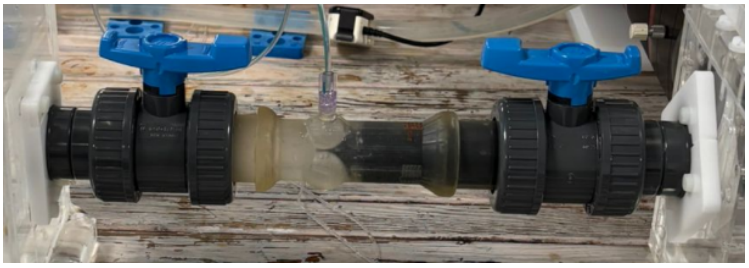

Figure 3.8: Zoomed view of the section of the mock loop in which the valve was mounted.

The raw geometry was pre-processed in Autodesk Inventor to isolate the fluid-relevant volume. Components specific to the experimental mounting (such as flanges, connectors, and external supports) were removed as they do not influence the internal hemodynamics.
A crucial geometric modification was introduced at the inflow section to resolve a diameter mismatch between the valve housing and the aortic root model. A structural support ring was modeled at the valve base and filleted to create a smooth transition to the sinus of Valsalva. This geometric adaptation was necessary to ensure continuity in the fluid domain and to prevent numerical singularities at the inlet boundary, which could otherwise compromise solver stability during the convergence of the flow equations. Following the procedure described in Section 3.3.1, the fluid domain was extracted via Boolean operations, resulting in a conforming assembly of the fluid volume, the aortic root, and the native valve leaflets.

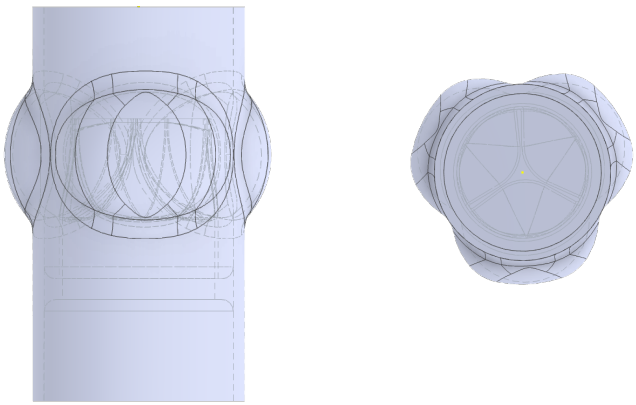

Figure 3.9: Native geometry of the aortic root and valve assembly shown in two representative views.

Integration of the TAVI Stent

To study the TAVI scenario, the model was further evolved by integrating the stent frame into the geometry (Figure 3.10). The stent was positioned within the aortic root, interacting with the native leaflets and the sinus wall. Unlike clinical scenarios where the frame is metallic, in this specific computational

setup, the stent was assigned the same material properties as the Sinus of Valsalva ($E = 2$ MPa, $\rho = 1200$ kg/m^3). This modeling choice was adopted to replicate the specific experimental conditions of the laboratory phantom and to maintain continuity in the structural domain without introducing abrupt stiffness discontinuities that could affect numerical convergence.

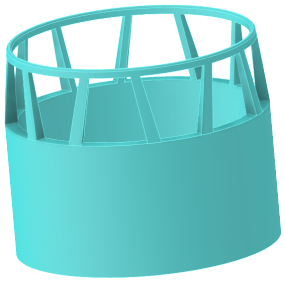

Figure 3.10: CAVE Lab stent geometry integrated into the computational model.

Definition of Case Studies

To evaluate the hemodynamic impact of device malpositioning, a comparative analysis was designed involving four distinct geometrical configurations. Starting from the nominal position, the device was virtually manipulated to simulate common procedural errors:

1. Nominal Configuration (Baseline): the device is centered and aligned with the aortic annulus, representing the ideal implantation.

2. Axial Translations (± 2.2 mm): two configurations were generated by translating the device vertically along the centerline: $+2.2$ mm (Supra-annular) simulating a shallow implantation and-2.2 mm (Sub-annular) simulating a deep implantation towards the LVOT.

3. Rotational Misalignment (60°): the device was rotated by 60 degrees clockwise relative to the aortic root axis.

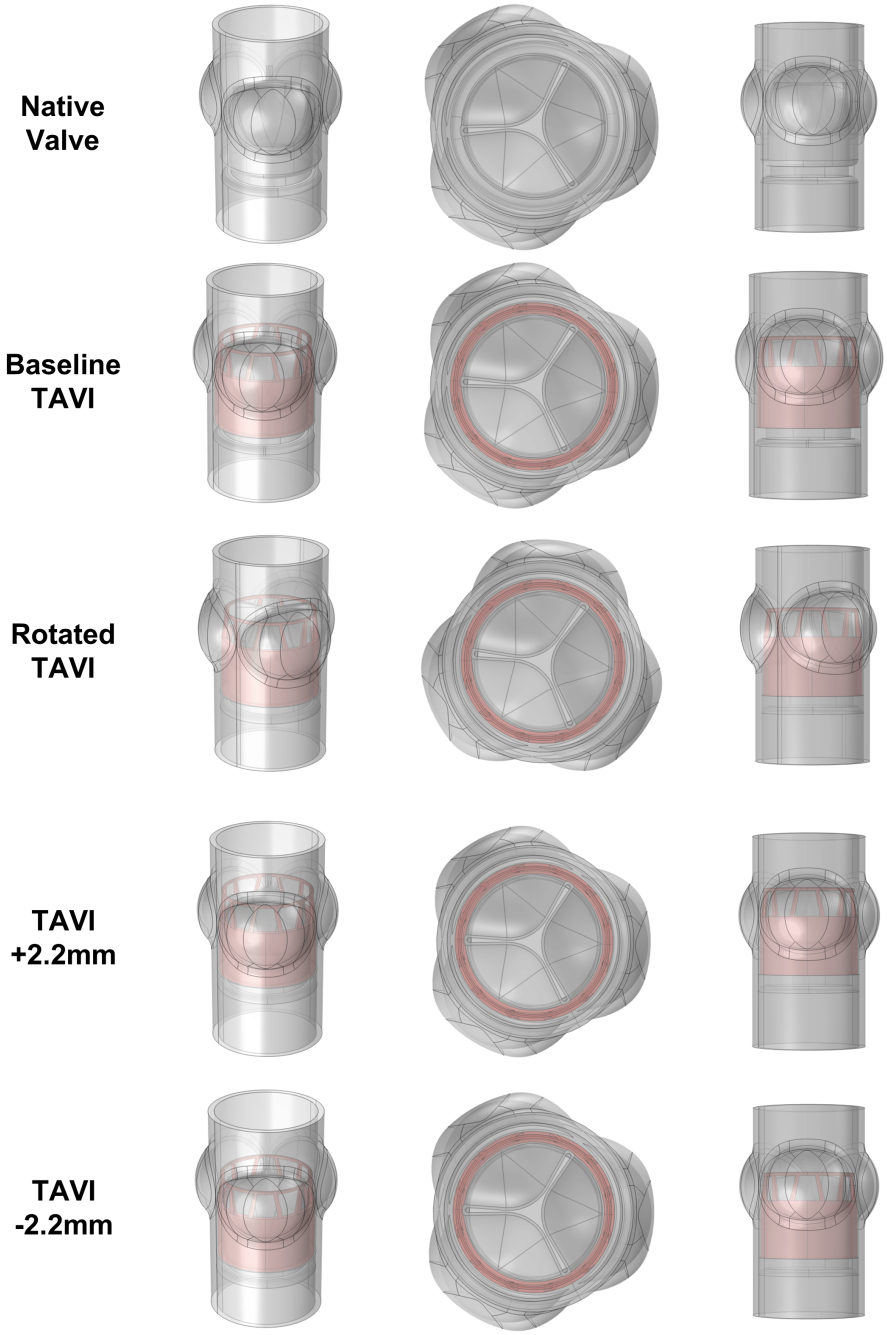

Figure 3.11: Comparison of the five investigated configurations shown in three different views. From top to bottom: native, nominal TAVI configuration, downward-translated configuration, upward-translated configuration, and rotated configuration.

3.4.2 Simulation Setup

The present simulations were deliberately restricted to the opening phase of the valve. This choice was motivated by the fact that, although COMSOL is widely used in cardiovascular multiphysics applications, the full numerical treatment of TAVI dynamics is still a demanding and not yet fully standardized task, due to the combined presence of large structural deformations, contact phenomena, and moving-mesh limitations. Moreover, the literature reviewed in this thesis shows that only a very limited number of studies have addressed the entire TAVI dynamic sequence in an integrated computational framework. Therefore, focusing on systolic opening allowed a more stable and controlled comparison among the investigated implantation configurations, while preserving the main hemodynamic information relevant to the objectives of this work.

Mesh While the preliminary coarse mesh (Section 3.3) was adequate for the valve-only configuration, the introduction of the TAVI stent required a more refined meshing strategy. The narrow gaps between the stent struts and the leaflets, together with the large nonlinear deformations of the valve during the cardiac cycle, made the original discretization insufficient for reliable FSI simulations.

A finer unstructured tetrahedral mesh was therefore generated. In particular, a smaller element size was assigned to the leaflets in order to better resolve their large deformations and their interaction with the surrounding domains. Moreover, boundary layers were introduced along the valve surfaces, corresponding to the blue-highlighted region visible in the valve mesh shown in the figure. These layers were used to improve the near-wall discretization and to better capture the high deformation and flow gradients developing close to the leaflet surfaces.

The fluid domain was also refined to ensure a more stable and accurate treatment of the moving mesh in the presence of large structural displacements.

For the sinus of Valsalva, a free triangular mesh was adopted on the corresponding boundaries, since this region does not directly participate in the deformational dynamics of the valve. This choice provided an adequate geometric discretization while limiting the overall number of mesh elements, thereby re-

ducing the associated memory requirements and computational cost.

Setup Consistent with the preliminary phase, the material properties for the fluid (Water) and the solid domains (linear elastic tissue) were maintained. However, unlike the preliminary quasi-static strategy, the final TAVI simulations were performed using a time-dependent study. This choice was motivated by the need to address the pronounced nonlinearities associated with the coupled FSI problem, including large leaflet displacements, moving-mesh deformation, and the complex interaction between the leaflets and the stent frame.

Under these conditions, a transient formulation was considered more suitable, as it allows the system response to develop progressively in time and improves the robustness of the numerical solution compared with a sequence of uncoupled stationary states. For numerical stability, the transient analysis was initialized from a stationary solution, which provided a physically consistent initial condition for the subsequent evolution of the velocity, pressure, and displacement fields. Given the strong nonlinearities of the coupled problem, the nonlinear solution method was set to Automatic Highly Nonlinear (Newton) in COMSOL. This option was adopted to improve the robustness of the iterative solution in the presence of large leaflet displacements, moving-mesh deformation, and strong fluid–structure coupling. Moreover, because the present work focuses specifically on the valve opening phase, the physiological boundary-condition curves were not applied over the entire cardiac cycle. Only the portion up to 0.3 s was retained for both inlet velocity and outlet pressure, as this interval contains the dynamics relevant to leaflet opening and early systolic flow development.

During the numerical solution, all five configurations exhibited a loss of convergence within the early systolic phase, around 0.07 s on average, although with some variability among cases. In particular, the rotated configuration stopped earlier, at approximately $t = 0.058$ s, whereas the downward-translated configuration remained convergent up to about $t = 0.079$ s. For this reason, the comparative analysis was restricted to the common reliable time interval, and only the results up to 0.07 s were considered in the Results chapter. Although the maximum converged time was not identical for all cases, this

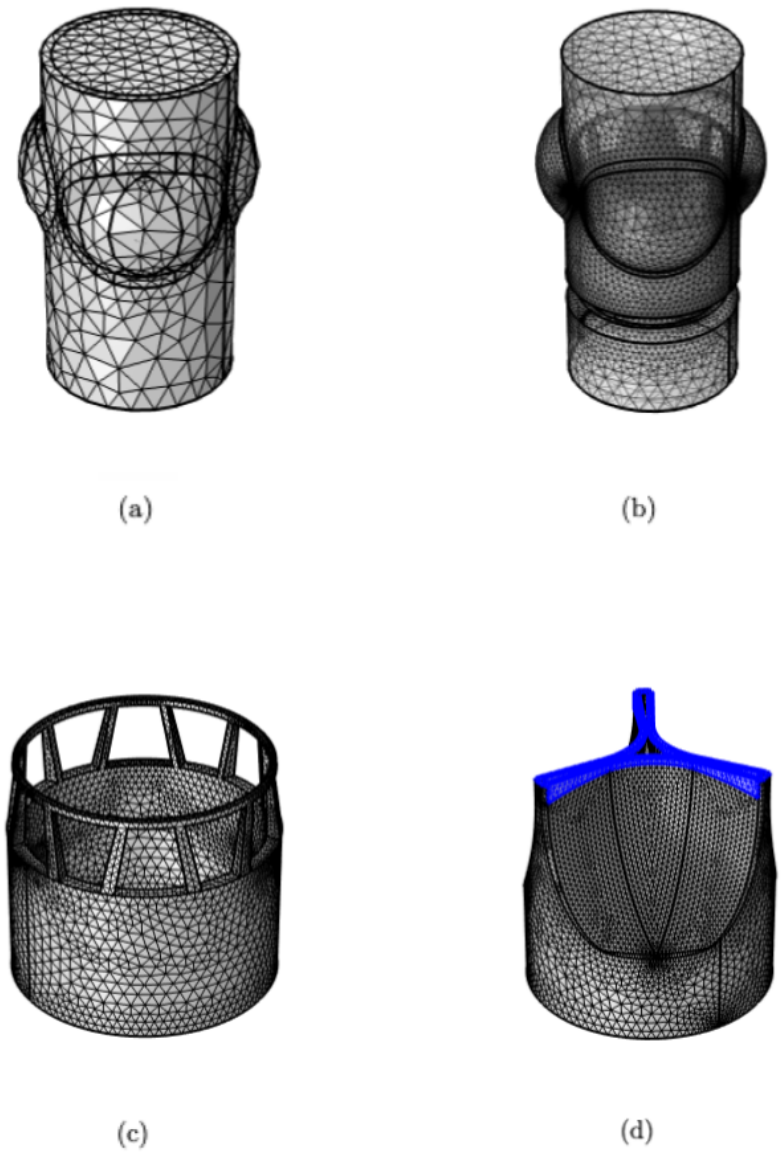

Figure 3.12: Meshes of the TAVI configuration and refined domains.

choice still ensures a consistent comparison of the early opening behaviour among the investigated configurations. The discrete values and corresponding waveforms adopted for the inlet velocity and outlet pressure boundary conditions are reported in Figure 3.13. In COMSOL, these data were implemented through piecewise cubic interpolation, which was preferred because it provides a smoother reconstruction of the experimental profiles than a linear interpolation. This choice was adopted to avoid abrupt changes between consecutive points and to ensure a more gradual and numerically stable variation of the imposed boundary conditions during the transient simulation.

Time [s]	Velocity [m/s]	Time [s]	Velocity [m/s]
0.00	0.0	0.16	1.705
0.01	0.005	0.17	1.664
0.02	0.012	0.18	1.577
0.03	0.044	0.19	1.456
0.04	0.088	0.20	1.316
0.05	0.146	0.21	1.169
0.06	0.225	0.22	1.027
0.07	0.333	0.23	0.896
0.08	0.476	0.24	0.778
0.09	0.656	0.25	0.673
0.10	0.865	0.26	0.578
0.11	1.087	0.27	0.489
0.12	1.299	0.28	0.403
0.13	1.481	0.29	0.317
0.14	1.614	0.30	0.227
0.15	1.690		

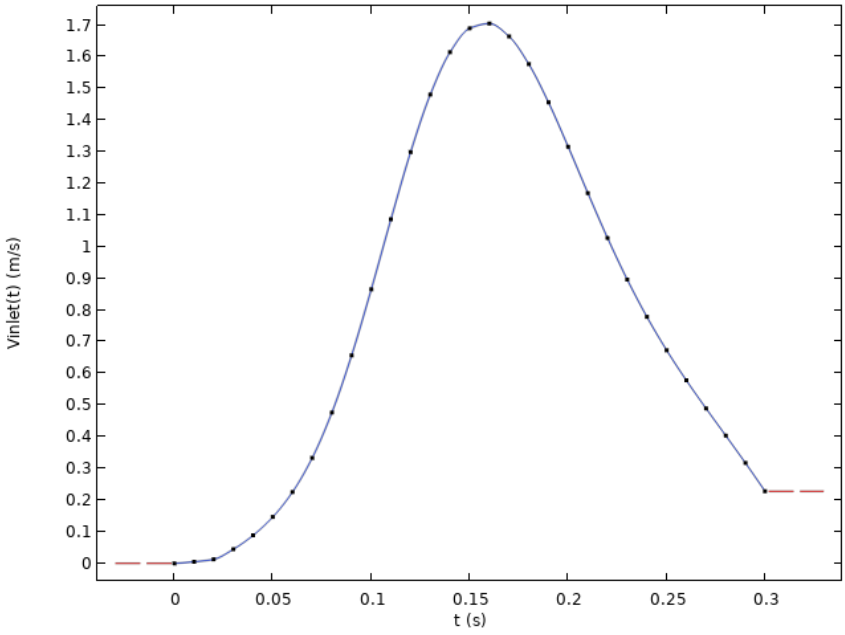

(a) Inlet velocity boundary condition.

Time [s]	Pressure [Pa]	Time [s]	Pressure [Pa]
0.00	10720.000	0.16	13374.614
0.01	10816.582	0.17	13673.155
0.02	10860.801	0.18	14019.812
0.03	10958.172	0.19	14389.148
0.04	11272.530	0.20	14761.652
0.05	11807.591	0.21	15107.585
0.06	12411.797	0.22	15390.906
0.07	13015.989	0.23	15590.857
0.08	13392.512	0.24	15709.353
0.09	13525.527	0.25	15757.919
0.10	13465.416	0.26	15748.741
0.11	13301.837	0.27	15692.608
0.12	13126.413	0.28	15596.193
0.13	13018.574	0.29	15463.167
0.14	13025.306	0.30	15310.411
0.15	13150.750		

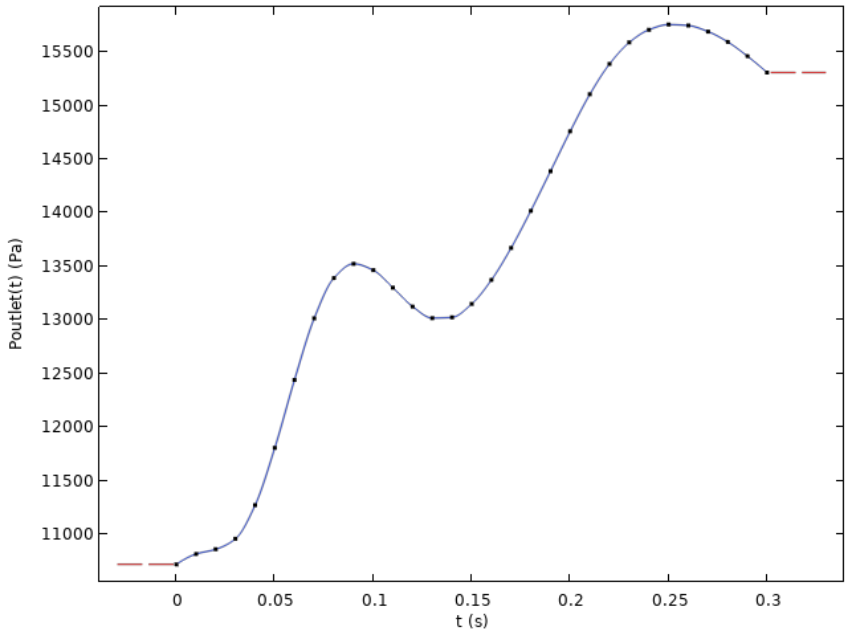

(b) Outlet pressure boundary condition.

Figure 3.13: Boundary conditions imposed in the simulations.

Chapter 4

Preliminary Numerical Development: Tutorials and Casting-Geometry Study

This chapter presents the preliminary numerical development that led to the final modular TAVI model adopted in this thesis. The tutorial-based benchmark cases and the initial casting geometry are discussed here not as auxiliary material, but as a fundamental intermediate step in the construction of the computational workflow.

The main purpose of this phase was twofold. First, it enabled a progressive familiarization with the FSI workflow in COMSOL Multiphysics, including moving boundaries, mesh deformation, and solver coupling. Second, it provided the first anatomically relevant platform on which to explore the numerical challenges associated with deformable valve simulations, such as convergence difficulties, mesh distortion, and sensitivity to boundary conditions.

4.1 Tutorial-based development of the COMSOL workflow

4.1.1 2D tutorial: vertical structure

The first preliminary case consisted of a two-dimensional tutorial reproducing the interaction between a laminar fluid flow and a flexible obstacle placed inside a straight micro-channel. The channel contains a vertical deformable structure, fixed at its base, which bends under the action of the fluid loading, with the inlet velocity waveform already illustrated in the previous chapter and a zero-pressure condition at the outlet.

The results of the 2D tutorial confirm the expected behaviour of a laminar flow interacting with a compliant obstacle. Figure 4.1 shows the deformed configuration of the vertical structure at $t = 4\,\mathrm{s}$, highlighting that the flow field and the structural response are consistently coupled during the transient simulation.

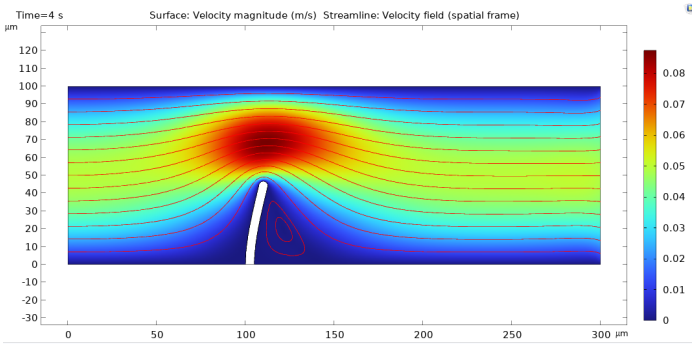

Figure 4.1: Streamline at t=4s.

Because the characteristic length scale of the channel is very small, the Reynolds number remains well below 100 ($\mathrm{Re} \ll 100$) and the flow is predominantly laminar across the domain. Local recirculation is limited: small eddies appear mainly upstream of the flexible structure, i.e., in the region immediately before the obstruction, while the downstream flow remains comparatively more regular. As expected, both the structure deformation and the size/location of these vortical regions are influenced by the imposed inflow magnitude (i.e.,

they change as the inlet velocity increases/decreases over time).
From a numerical standpoint, the tutorial is particularly useful to visualize how the moving mesh behaves.
Figure 4.2 shows the mesh velocity at $t = 0$ s: since the only deforming boundaries are those belonging to the vertical structure, the mesh velocity reaches its largest values in the proximity of that interface. Moreover, the mesh-velocity pattern is not fixed in time, but varies depending on whether the structure is undergoing increasing deformation, recovering, or remaining in a quasi-stationary state.
Finally, Figure 4.3 compares the mesh after deformation. The initial mesh is relatively uniform around the structure tip, while the deformed configuration highlights a clear redistribution of element shapes: as the obstacle bends, the mesh becomes stretched on one side and compressed on the other, reflecting the direction of the structural displacement.

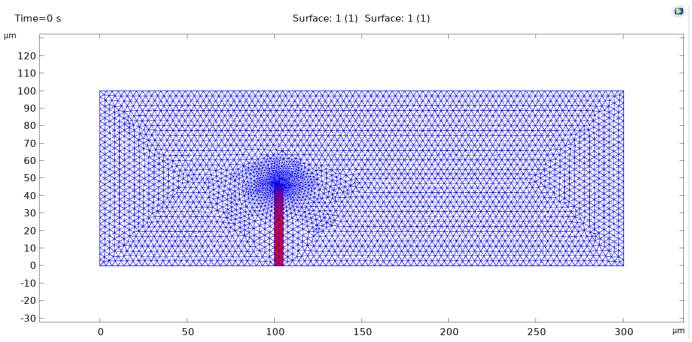

Figure 4.2: Mesh at time = 0s

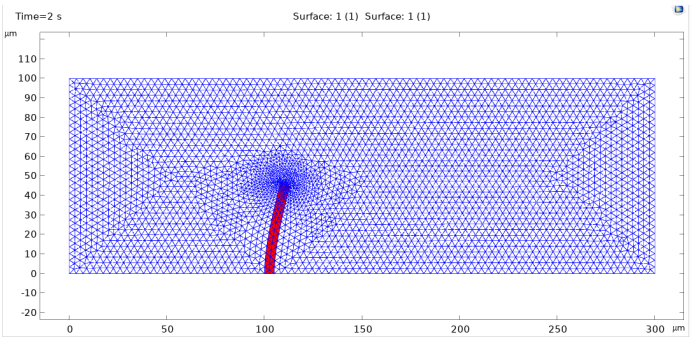

Figure 4.3: Mesh at time = 2s

Overall, this tutorial served as a practical entry step to understand the key COMSOL interfaces used in FSI problems and to verify that the ALE formulation can robustly resolve flow variables on a continuously deforming domain.

4.1.2 3D tutorial: cylindrical channel flow

After the 2D exercise, the workflow was extended to a fully three-dimensional configuration by means of a simple cylindrical channel with prescribed inlet velocity and zero-pressure outlet. In this case, no structural deformation was included; the objective was instead to verify the stability of the numerical setup in 3D and to gain familiarity with geometry definition, domain selection, boundary assignment, and post-processing of velocity and pressure fields.
The results of the three-dimensional tutorial are reported in Figure 4.4. The velocity magnitude distribution, evaluated on a vertical section of the cylindrical domain, exhibits the expected behaviour for laminar internal flow. In particular, the velocity profile shows a parabolic-like shape, with the highest values located along the central axis and progressively lower values toward the walls as a result of viscous effects.
The pressure field within the domain also follows the expected trend. A monotonic decrease in pressure is observed along the axial direction of the cylinder, consistent with the viscous pressure losses associated with internal flow under a prescribed inlet velocity and a zero-pressure condition at the outlet.

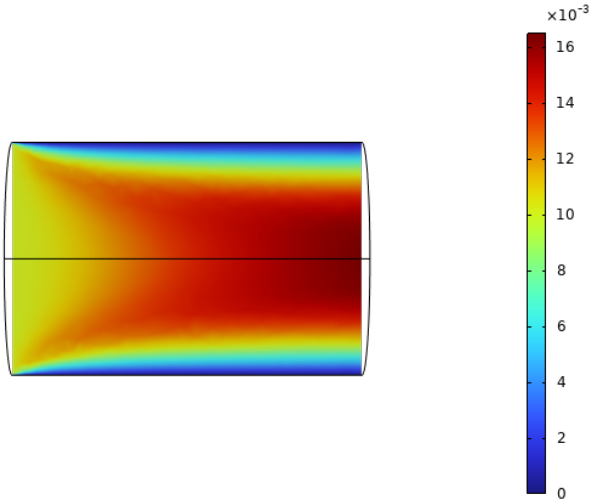

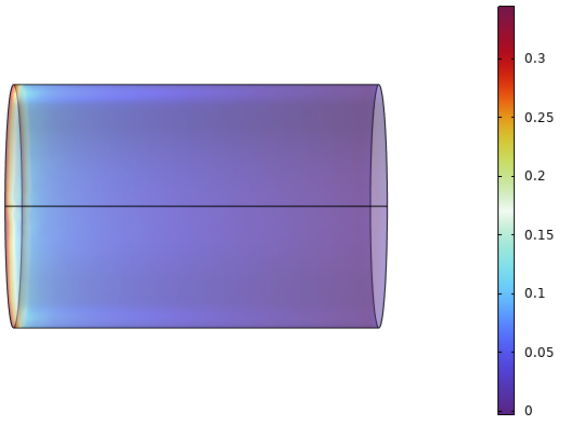

Figure 4.4: Velocity field [m/s] (up) and Pressure [Pa] (down)

This tutorial represented a fundamental intermediate step between the simplified 2D FSI example and the subsequent 3D valve-oriented simulations. It allowed validation of the numerical setup in three dimensions and ensured robustness of solver settings before introducing structural coupling and complex anatomical geometries.

4.2 Initial transfer to an anatomically relevant geometry: the casting model

Following the tutorial phase, the workflow was transferred to the first anatomically relevant configuration of the thesis, namely the three-dimensional aortic valve model referred to as the casting geometry. This geometry was based on a pre-existing laboratory model available at the CAVE Lab at Aarhus University and included both the aortic valve and the sinus of Valsalva. The assembled CAD geometry can be found in the previous chapter.
The casting model represented the first platform on which simplified but anatomically meaningful FSI simulations could be attempted.

4.2.1 Progressive numerical exploration on the casting model

The objective of this phase was not yet the extraction of definitive quantitative results, but rather the identification of a sufficiently stable numerical framework for the simulation of valve opening. In this context, the performed tests showed that the numerical behaviour of the model depended on the combined interaction of several factors rather than on a single modelling choice. In particular, relevant difficulties emerged when leaflet motion induced severe deformation of the fluid mesh, especially near narrow gaps and highly curved regions.

A first sufficiently robust strategy was obtained through concatenated stationary studies, in which different inlet–outlet boundary-condition pairs were imposed at successive time instants of the cardiac cycle. This approach proved useful because the individual stationary steps were able to converge and therefore provided an initial exploration of the model response under progressively varying loading conditions.

However, since valve opening is intrinsically a transient phenomenon, the stationary concatenation could only provide a quasi-static approximation of the underlying dynamics. The analysis was therefore shifted to a time-dependent framework, which was considered not only more physically consistent, but also numerically more robust for this specific FSI problem, as it allowed a progressive evolution of the coupled solution in the presence of strong nonlinearities, leaflet deformation, and moving-mesh effects.

A more robust solution was eventually obtained when the simulations were driven by experimentally informed inlet-velocity and outlet-pressure conditions and initialized from a stationary state.

4.2.2 Representative results from the convergent casting simulation

Once a sufficiently stable setup had been identified, a time-dependent simulation of the opening phase was obtained for the casting geometry. The analysis was driven by the systolic portion of the experimentally informed inlet-velocity

and outlet-pressure curves.. These boundary conditions were applied in time-dependent form so as to reproduce the progressive loading acting on the valve during the opening stage.
The analysis was therefore restricted to the valve opening phase, where the model remained numerically manageable and where the evolution of leaflet deformation and transvalvular flow could be visualized consistently.

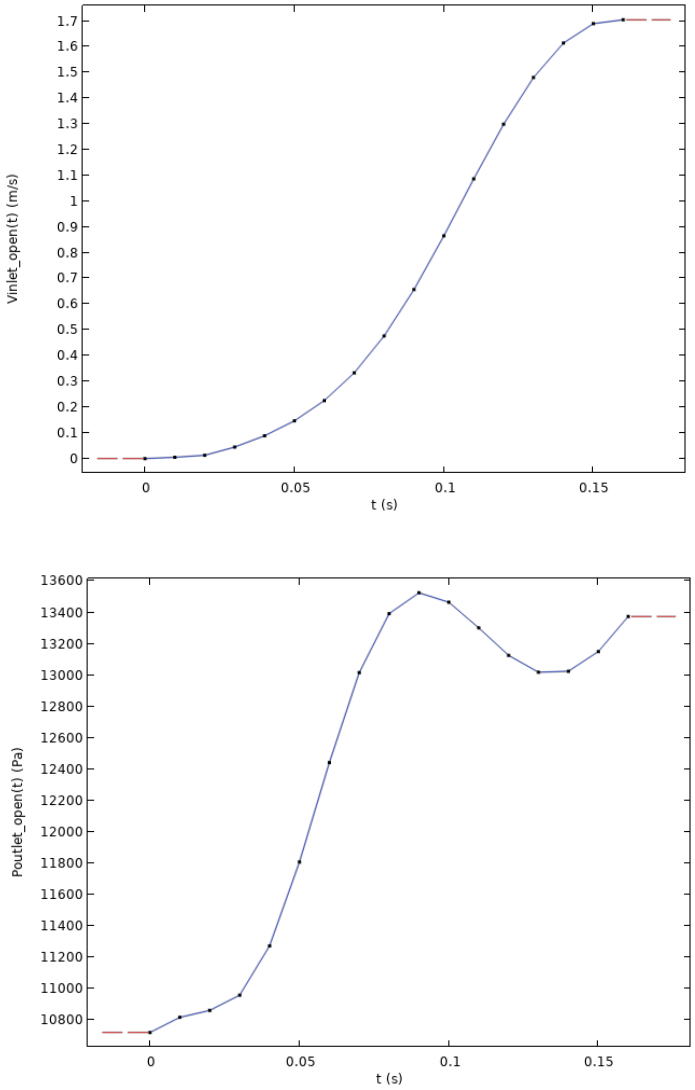

Figure 4.5: Systolic portion of the inlet velocity waveform and outlet pressure curve used as time-dependent boundary conditions for the opening-phase simulation of the casting geometry.

Once convergence during the opening phase had been achieved, the simulation

results were used to illustrate the progressive valve-opening process at different time instants. The resulting fields were inspected at four representative stages of the transient response, namely $t = 0\,\mathrm{s}$, $0.05\,\mathrm{s}$, $0.10\,\mathrm{s}$, and $0.15\,\mathrm{s}$.

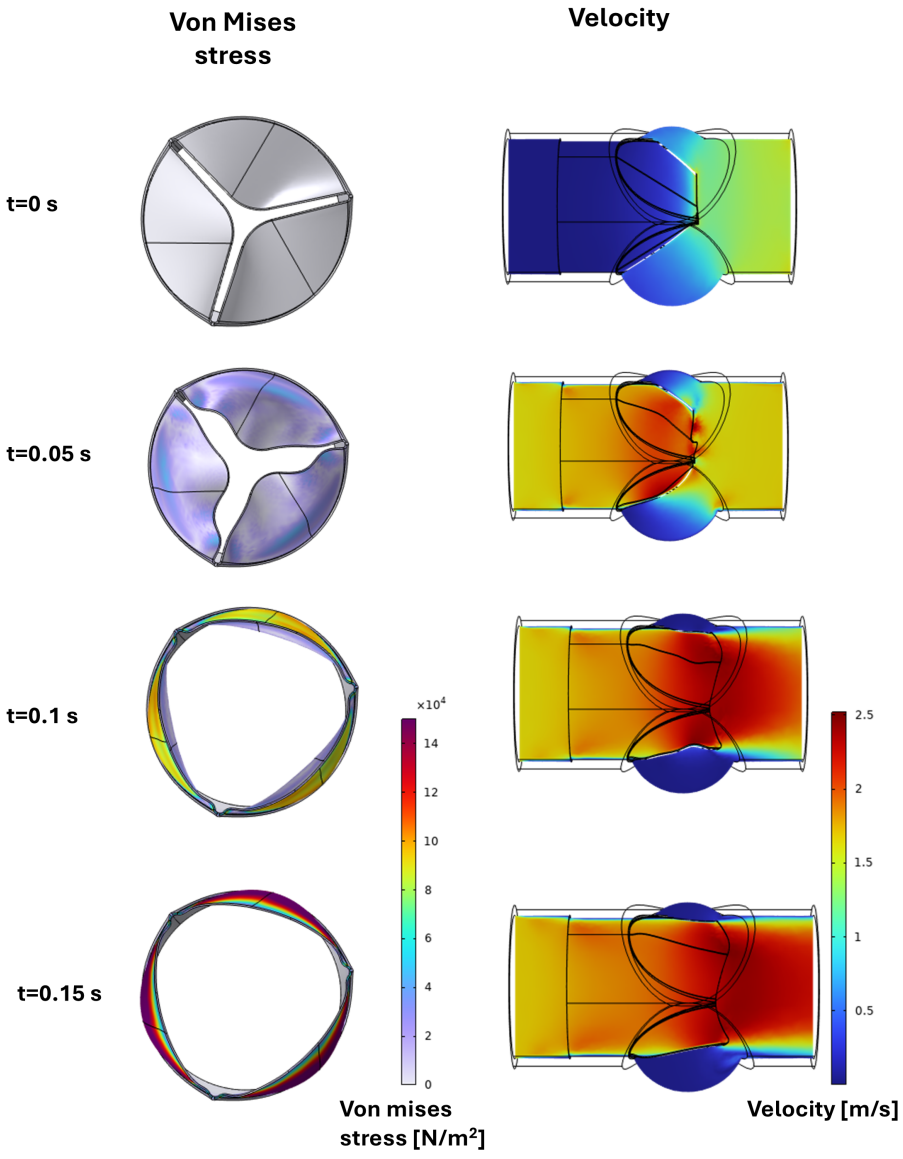

Figure 4.6: Representative results of the opening-phase simulation for the casting geometry. The figure reports the von Mises stress distribution on the valve leaflets and the velocity contours in the fluid domain at four representative time instants ($t = 0\,\mathrm{s}$, $0.05\,\mathrm{s}$, $0.10\,\mathrm{s}$, and $0.15\,\mathrm{s}$), highlighting the progressive leaflet opening and the associated development of the transvalvular flow field.

In Figure 4.6 the von Mises stress distribution on the leaflets and the velocity contours in the fluid domain are reported at different stages of the opening phase. These snapshots are not intended for a detailed quantitative comparison, but rather to document that the model was able to reproduce a coherent progression of leaflet opening together with the corresponding flow development.

At $t = 0\,\mathrm{s}$, the valve is still in its initial closed configuration, with negligible leaflet deformation and a limited flow field within the domain. At $t = 0.05\,\mathrm{s}$, the opening process has started and the leaflets already exhibit an appreciable deformation, accompanied by the appearance of localized stress regions and by the initial acceleration of the fluid through the emerging central orifice. At $t = 0.10\,\mathrm{s}$, the opening is more advanced: the effective flow passage is wider, the transvalvular jet becomes more clearly established, and the stress distribution appears increasingly concentrated in the peripheral and commissural regions of the leaflets. Finally, at $t = 0.15\,\mathrm{s}$, the valve reaches a more developed open configuration, with a fully formed jet crossing the valve and a stress pattern mainly localized along the leaflet attachment regions, consistent with the structural loading induced during opening.

From the structural point of view, the stress maps show that leaflet deformation progressively increases as the imposed loading rises during systole. From the fluid-dynamic point of view, the velocity contours show the corresponding growth and strengthening of the transvalvular flow region during valve opening. Taken together, these results provided the first visual confirmation that the adopted workflow could generate a physically interpretable coupled response in an anatomically meaningful geometry.

This result was especially important because it demonstrated that, despite the repeated numerical instabilities observed during the preliminary attempts, the workflow could eventually be brought to a convergent transient solution for the valve opening phase.

4.2.3 Simplified contact analysis on the casting geometry

In addition to the opening-phase analysis, a simplified contact study was performed in order to introduce and preliminarily assess leaflet–leaflet interaction

during valve closure. In this case, an adverse transvalvular pressure gradient was imposed by setting the inlet pressure to 0 Pa and the outlet pressure to 12000 Pa, so as to promote leaflet coaptation. To facilitate the numerical treatment of the contact problem, a small artificial gap was introduced between adjacent leaflets, together with the definition of three leaflet–leaflet contact pairs.

This pressure-driven configuration was adopted as a preliminary and numerically tractable basis for contact modelling. In particular, the simplified pressure-gradient boundary conditions were selected because they provided a more manageable framework for activating the contact formulation, whereas more complex loading conditions would have introduced additional numerical difficulties in an already strongly nonlinear problem.

The results of this analysis are shown in Figure 4.7, which reports the undeformed reference configuration together with representative fields obtained under the imposed closing load.

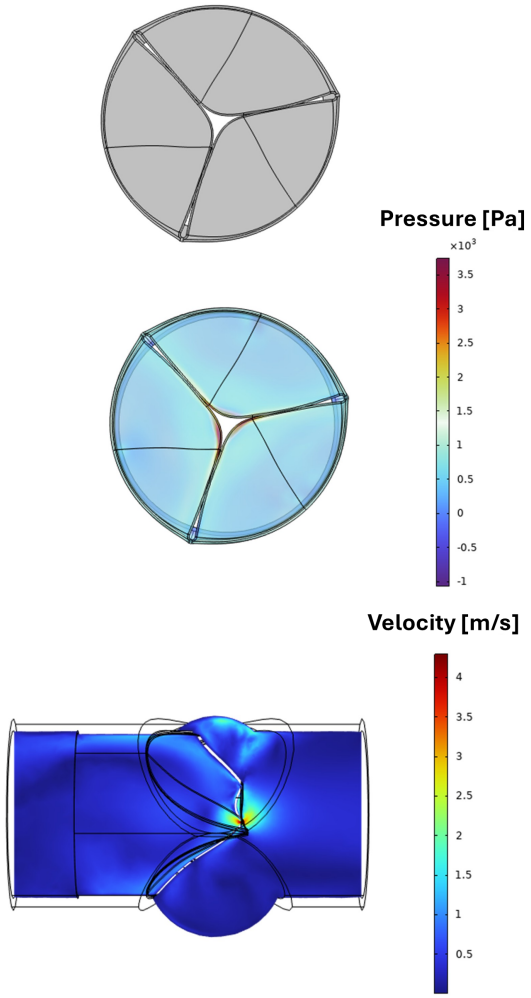

Figure 4.7: Representative results of the simplified contact analysis performed on the casting geometry under an imposed adverse pressure gradient. From top to bottom: undeformed reference configuration, pressure distribution on the valve leaflets under the applied closing load, and velocity magnitude contour in the central plane of the fluid domain.

The imposed pressure gradient promotes leaflet approach toward a closed configuration. The pressure field on the leaflets highlights the loading responsible for the closure tendency, while the velocity contour in the central plane shows the corresponding flow pattern developing under the imposed adverse transvalvular condition. From a methodological point of view, this result was relevant because it demonstrated that a contact treatment could be introduced within the computational framework, at least under simplified loading conditions. Therefore, although preliminary, this test represented an important first step toward the inclusion of leaflet contact in the model, even if the complete dynamic simulation of valve closure remained outside the scope of the present study.

4.3 Main limitations and take-home messages

The tutorial and casting phases also made the main limitations of the adopted numerical framework explicit. The most relevant issue concerned the numerical robustness of the ALE-based fluid–structure interaction formulation. During model development, the solution process was repeatedly affected by non-convergence, deterioration of mesh quality, and mesh distortion in regions characterized by strong leaflet motion and narrow fluid passages. These observations clearly indicated that moving-mesh handling represented one of the principal bottlenecks of the workflow.

At the same time, despite its preliminary nature, this development phase provided several essential indications for the construction of the final modular TAVI model.

First, it became evident that the numerical problem had to be addressed progressively. Starting directly from the final TAVI geometry would have made it considerably more difficult to identify the origin of the observed instabilities and to distinguish geometric issues from solver-related or mesh-related difficulties. The use of simplified tutorials and of the casting geometry therefore proved fundamental in building the workflow step by step.

Second, the casting simulations showed that a transient analysis initialized from a stationary solution provided a more robust strategy than direct time-

dependent attempts. This observation directly informed the final study definition adopted for the TAVI simulations, where stationary initialization was retained as part of the numerical setup.

Third, the strong sensitivity of the solution to mesh quality and to the definition of the boundary conditions highlighted the importance of carefully controlling local geometric complexity, leaflet deformation, and moving-mesh behaviour. This consideration motivated the more controlled meshing strategy adopted in the final model and also supported the decision to restrict the analysis to the opening phase, where the simulations remained both more numerically stable and more interpretable from a physiological point of view.

Finally, this preliminary phase clarified the methodological importance of the casting geometry itself. Rather than representing an isolated side study, it served as the first anatomically relevant testbed on which the COMSOL-based FSI workflow could be explored in a realistic valve environment. In this sense, the main outcome of the present chapter lies not only in the presentation of preliminary simulations, but also in the identification of the modelling and numerical choices that ultimately made the final comparative TAVI analysis possible.

Overall, the tutorial and casting stages should therefore be regarded as the phase in which the computational workflow of the thesis was effectively built. They revealed the main limitations of the adopted approach, demonstrated its feasibility within a controlled scope, and provided the practical and methodological basis for the final simulations discussed in the following chapters.

Chapter 5

Computational Results and Comparison for the Final TAVI Model

This chapter presents the computational results obtained from the five time-dependent simulations performed on the final modular TAVI geometry developed in this thesis.

The five analysed cases include the native valve, the nominal TAVI configuration, the downward-translated configuration, the upward-translated configuration, and the rotated configuration. All simulations were performed under the same transient inlet-velocity and outlet-pressure boundary conditions, thereby enabling a controlled comparative assessment of the effect of prosthesis positioning within the final geometry.

As discussed in Chapter 3, the simulations did not all reach exactly the same final converged time. For this reason, the comparison is mainly based on common time instants during early systole, whereas the last converged configuration-specific state is discussed separately when relevant. Within this framework, the chapter combines qualitative and quantitative analyses in order to evaluate how implantation and malpositioning influence leaflet kinematics and the associated hemodynamic response.

As shown in Figure 5.1, the results were extracted and visualized on common reference sections of the model, so as to ensure consistency across the five

investigated configurations.

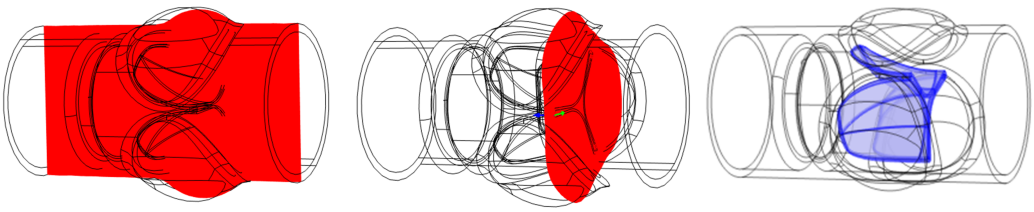

Figure 5.1: Cut planes used for the results analysis.

5.1 Qualitative comparison of the opening dynamics

A qualitative analysis was first performed to assess how the five configurations respond during the early systolic opening phase, considering both leaflet kinematics and the associated flow development. Since all cases were subjected to the same transient forcing, the comparison was structured to follow the progressive increase of the imposed inlet waveform.

Four representative stages were considered: $t = 0.02$ s, $t = 0.04$ s, $t = 0.06$ s, and the last converged time step reached by each configuration. The first three instants represent the onset of leaflet motion, an intermediate stage of opening, and a more advanced stage of the early systolic response. By contrast, the last row of the qualitative figures does not correspond to a common physical time, but rather to the last converged state of each individual simulation. Therefore, this final comparison should not be interpreted as a synchronous evaluation under identical loading conditions, but as an additional indication of how far each configuration could progress within the opening phase before loss of convergence.

Figure 5.2 reports the qualitative comparison of leaflet opening dynamics. At $t = 0.02$ s, all configurations remain close to their initial condition and only the onset of leaflet separation can be appreciated.

At $t = 0.04$ s, the opening process becomes more developed and the differences

among configurations are more evident. The native valve shows a wider and more regular central orifice, with a comparatively symmetric trileaflet opening pattern. The nominal TAVI configuration also reaches a clearly open state, but the effective opening appears slightly more restricted. Among the malpositioned cases, the rotated configuration displays the most evident loss of symmetry, suggesting that rotational misalignment perturbs the regularity of leaflet excursion more markedly than axial translation. The two translated cases remain intermediate, with the downward-translated configuration appearing slightly more permissive than the upward-translated one.

At $t = 0.06$ s, the native valve maintains the widest and most regular opening among the available cases. The nominal TAVI is also well open, but its effective orifice remains smaller than that of the native configuration. The downward-translated case appears to reach the largest opening among the prosthetic models, whereas the upward-translated configuration remains slightly more compact. The rotated configuration is no longer available at this time, since its simulation terminated earlier. This earlier loss of convergence is itself a relevant result, as it suggests that rotational malpositioning is the most critical condition from the standpoint of numerical stability and, indirectly, of kinematic regularity.

The last row must be interpreted with caution because it compares the final converged state of each case rather than the same physical instant. Nevertheless, it remains informative. The rotated configuration reaches the earliest final time and still shows a less advanced opening state than the other cases, confirming its more restricted and asymmetric behaviour. The downward-translated configuration progresses furthest in time and exhibits a more developed opening, whereas the upward-translated and nominal TAVI cases remain intermediate.

Overall, the qualitative comparison indicates that the native valve preserves the most regular and symmetric opening pattern, while prosthesis implantation already introduces a certain degree of constraint even in the nominal case. Among the malpositioned conditions, rotational misalignment is the most disruptive, whereas axial translations have a milder but still appreciable and direction-dependent effect.

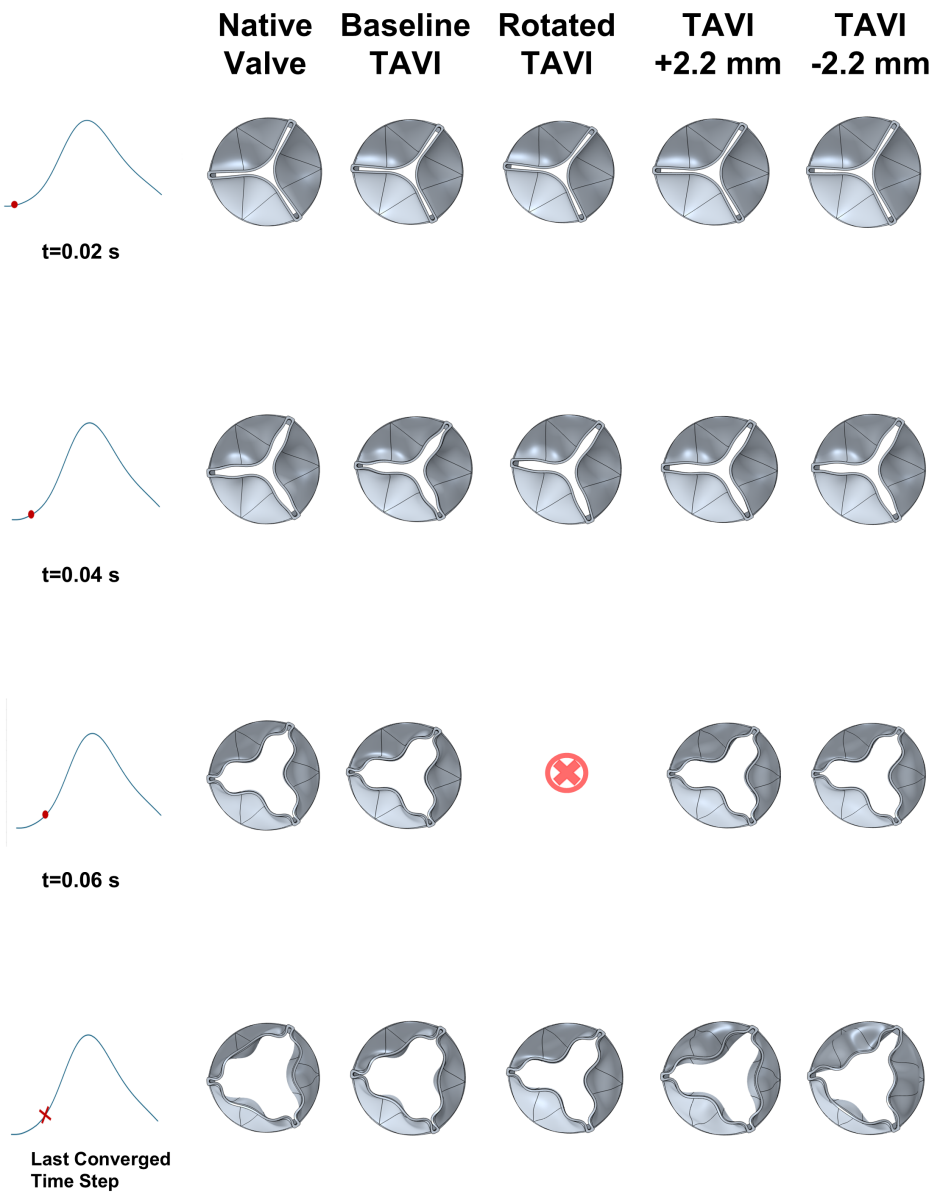

Figure 5.2: Qualitative comparison of leaflet opening dynamics for the five simulated configurations at four representative time instants: 0.02 s, 0.04 s, 0.06 s, and the last converged time step before loss of convergence. The first column indicates the corresponding position of each instant along the imposed temporal waveform. The rotated TAVI configuration is not shown at $t = 0.06$ s because the simulation diverged before reaching this time instant.

Figure 5.3 complements this analysis by showing the corresponding velocity contours. At $t = 0.02$ s, the flow field remains dominated by low velocities in all cases, which is consistent with the very early stage of the imposed waveform. At $t = 0.04$ s, a clearly identifiable transvalvular jet develops in all configurations, but its organization differs across cases. The native valve exhibits a broader and more regular accelerated region, whereas the nominal TAVI shows a more concentrated jet, consistent with a more constrained effective opening. The rotated configuration stands out because the high-velocity region is more localized and less evenly distributed, suggesting the emergence of an asymmetric preferential flow pathway.

At $t = 0.06$ s, the native valve maintains the most regular and centred jet, while the nominal TAVI exhibits a more contracted high-velocity core. The translated configurations remain intermediate, with the downward-translated case showing the most extended high-velocity region among the prosthetic models. Again, the rotated configuration is absent because its simulation terminated earlier.

Taken together, Figures 5.2 and 5.3 show that TAVI malpositioning affects not only leaflet motion but also the spatial organization of the systolic jet. In particular, the rotated configuration displays the clearest qualitative alteration of both kinematics and flow structure, whereas the translated configurations appear less disruptive, although still distinguishable from the native and nominal cases.

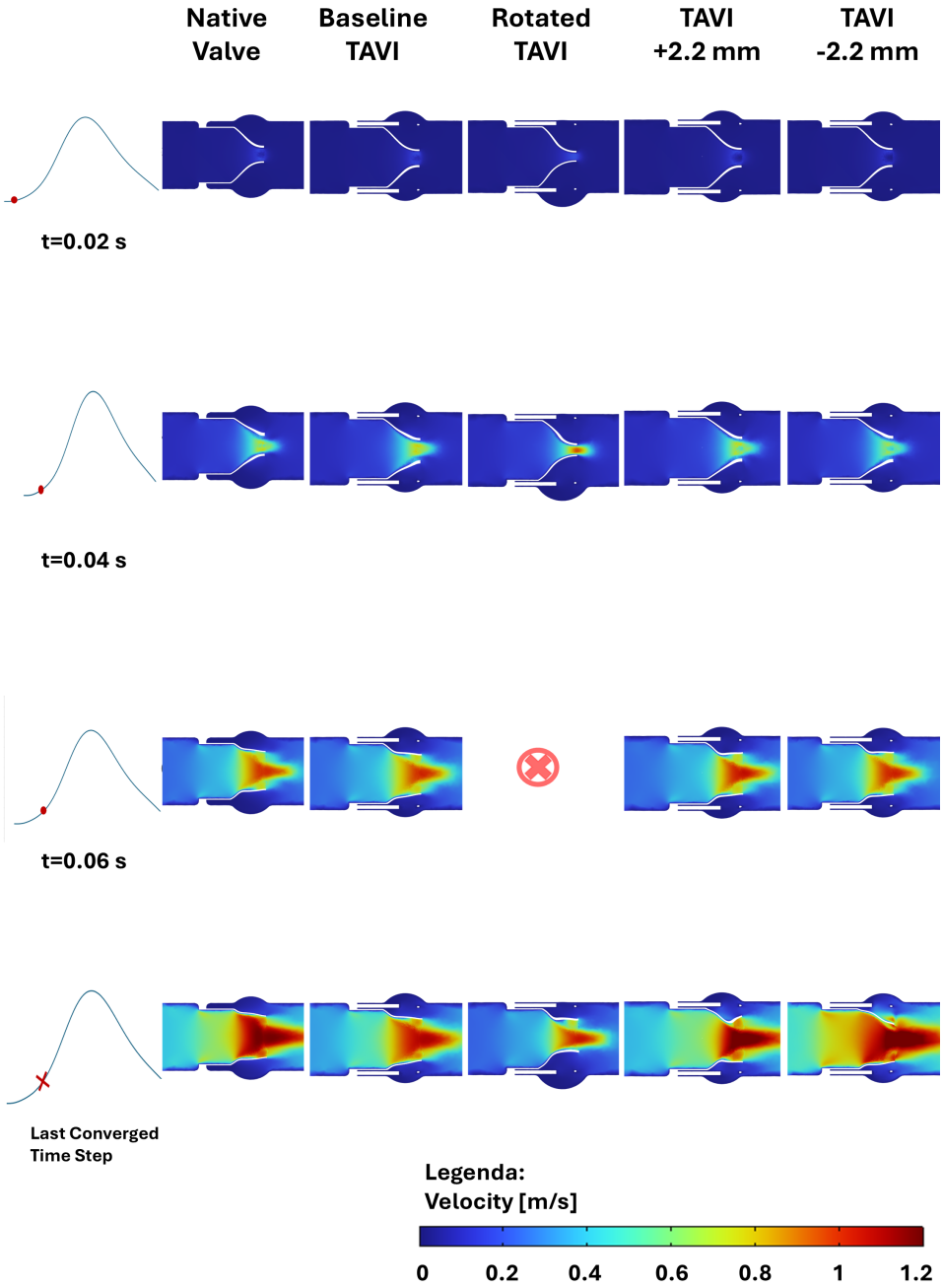

Figure 5.3: Qualitative comparison of velocity contours for the five simulated configurations at four representative time instants: 0.02 s, 0.04 s, 0.06 s, and the last converged time step before loss of convergence. The rotated TAVI configuration is not shown at $t = 0.06\,\mathrm{s}$ because the simulation diverged before reaching this time instant.

To complement the numerical qualitative comparison, high-speed camera images acquired during the mock-loop experiments were also inspected for the native valve and the baseline TAVI configuration. These frames provide an experimental visualization of the early opening sequence and allow a direct qualitative comparison of the evolving orifice shape. In both configurations, the frames at $t = 0.02$ s show only the onset of leaflet separation. At $t = 0.04$ s, the native valve displays a broader opening pattern than the baseline TAVI, although the leaflet motion is not perfectly symmetric, with slight differences in the opening of the three leaflet sectors. This feature becomes more evident at $t = 0.06$ s, where the native configuration reaches a visibly larger orifice, but with a mildly irregular and unbalanced shape. The baseline TAVI, on the other hand, maintains a narrower opening area with a more triangular and visually more regular geometry. These observations suggest that, in the experimental setup, the native valve preserves a larger effective opening but does not behave as a perfectly ideal symmetric configuration. Despite this difference, the high-speed images remain qualitatively consistent with the computational results in showing a more constrained opening in the prosthetic case.

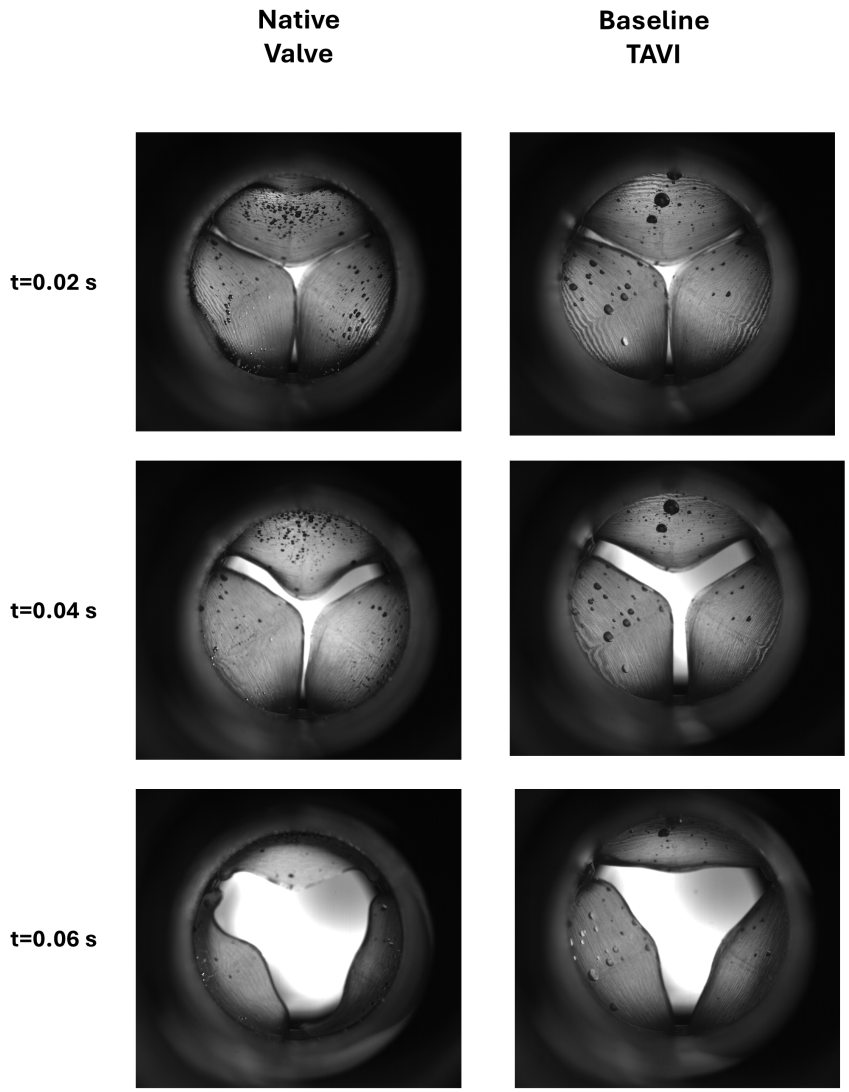

Figure 5.4: High-speed camera frames acquired during the mock-loop experiments for the native valve and the baseline TAVI configuration at three representative time instants of the opening phase ($t = 0.02$ s, 0.04 s, and 0.06 s).

5.2 Quantitative comparison of leaflet kinematics

In order to complement the qualitative observations, a quantitative analysis of leaflet kinematics was carried out for all five configurations. Two indicators were considered: the maximum leaflet displacement and the maximum von Mises stress of the leaflets.

5.2.1 Maximum Leaflet displacement

The first quantity considered was the maximum leaflet displacement as a function of time, reported in Figure 5.5. This parameter provides a global measure of the opening response and allows the temporal evolution of leaflet motion to be compared among the five cases.

In all configurations, the maximum displacement increased progressively during the early systolic phase. The differences among cases remained limited at the beginning of the opening process and became more evident only after approximately $t = 0.04$ s. This indicates that the investigated geometric variations had a modest influence on the onset of leaflet motion, whereas their effect became more pronounced during the later stages of opening.

This trend is clearly visible in the temporal curves. At $t = 0.055$ s, the displacement values were still relatively close: 3.18 mm for the native valve, 3.22 mm for the nominal TAVI, 3.22 mm for the downward-translated configuration, 3.40 mm for the upward-translated configuration, and 3.25 mm for the rotated configuration. At this common time instant, therefore, the nominal prosthesis did not yet show a marked reduction in opening relative to the native condition. The main divergence appeared later, during the terminal part of the opening phase.

When the final peak values are considered, the downward-translated configuration reached the highest maximum displacement, with 7.67 mm at 0.080 s. The native valve followed with 7.14 mm at 0.074 s, while the upward-translated case reached 5.98 mm at 0.072 s. Lower peak values were observed for the nominal TAVI and for the rotated configuration, with maxima of 5.22 mm at 0.0688 s and 3.86 mm at 0.0589 s, respectively.

The comparison between the native and nominal TAVI configurations should therefore be interpreted carefully. The nominal prosthesis cannot simply be described as showing lower leaflet motion throughout systole, because at matched time instants the two curves remain relatively close for most of the opening phase. Rather, the main difference emerges in the late-opening stage, where the native valve continues to open for longer and reaches a larger final excursion. From a functional perspective, the nominal TAVI still preserves a relatively regular opening pattern, although its final displacement remains smaller than that of the native valve.

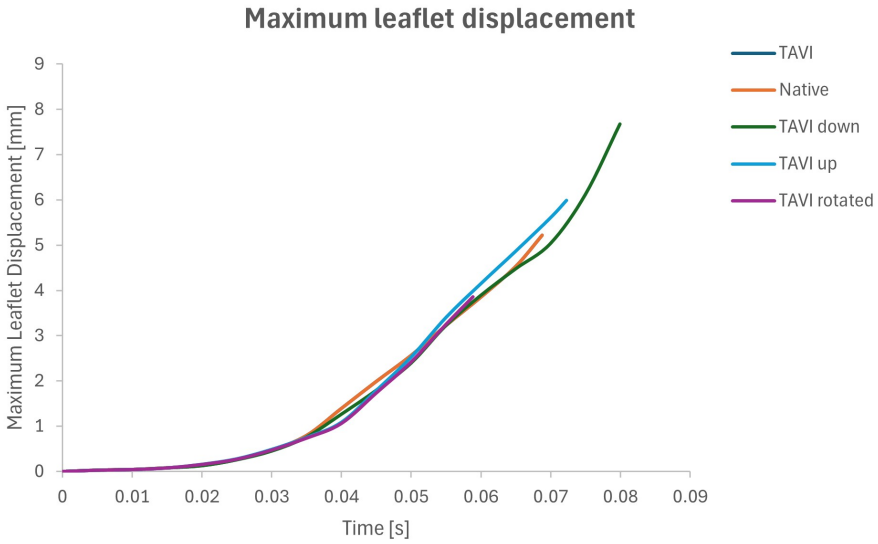

Figure 5.5: Time evolution of maximum leaflet displacement for the native valve, the nominal TAVI configuration, and the three malpositioned cases.

The corresponding three-dimensional displacement (Figure 5.6) maps help to interpret these results. In the native and nominal configurations, the opening pattern remains relatively regular, with a centred orifice and a fairly balanced distribution of leaflet motion. The native valve, however, exhibits a wider opening, consistent with its larger terminal excursion. In this context, asymmetry should not be identified from the peak displacement value alone, but from the spatial distribution of motion. A symmetric configuration is associated with a regular three-lobed opening pattern and a comparable displacement distribution among the three leaflets, whereas asymmetry is reflected by the presence

of a less mobile leaflet and by a non-uniform contour distribution.

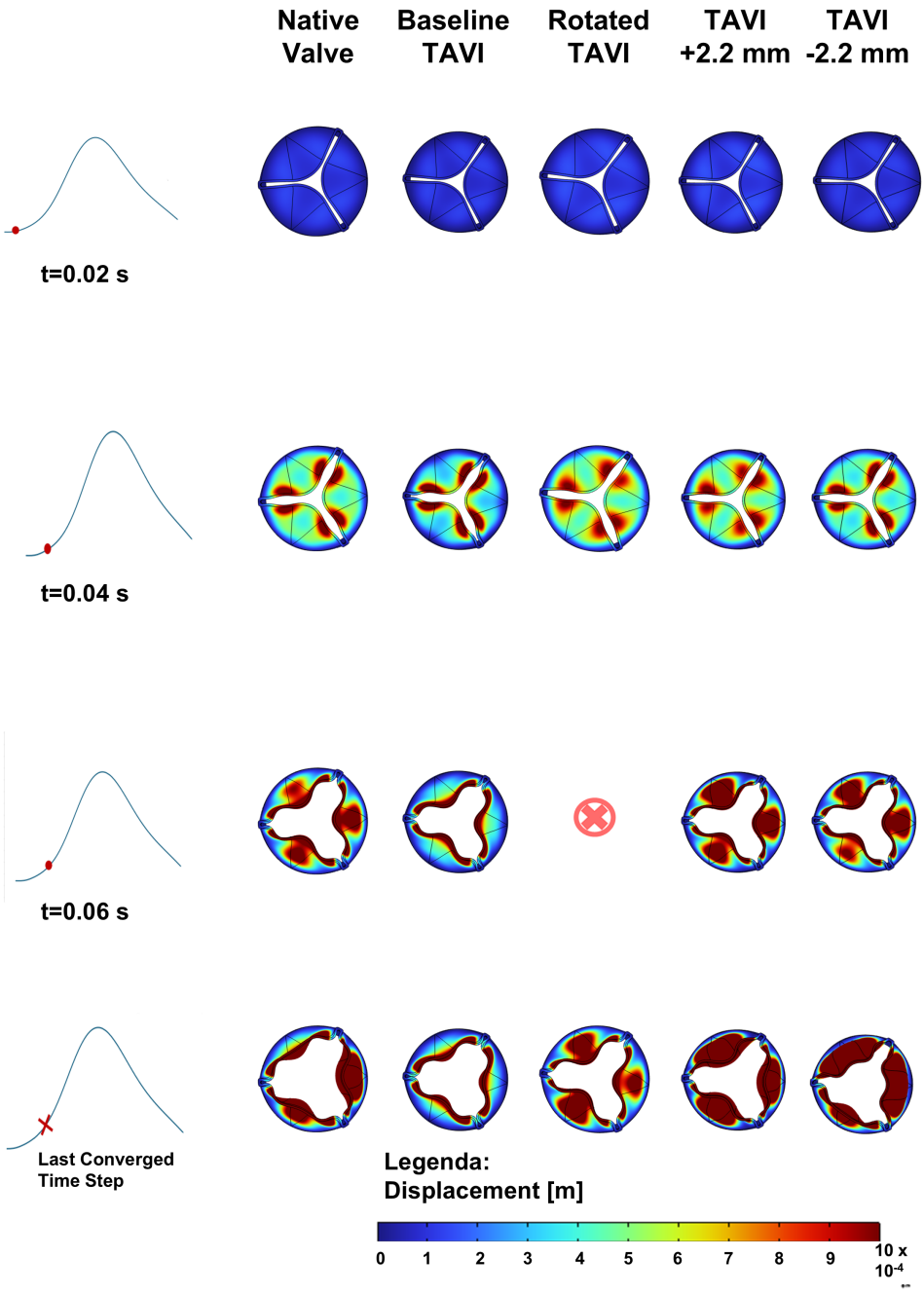

Figure 5.6: Comparison of leaflet displacement maps for the native and nominal TAVI configurations at a representative time instant of the opening phase. The rotated TAVI configuration is not shown at $t = 0.06\,\mathrm{s}$ because the simulation diverged before reaching this time instant.

This interpretation is particularly useful for the malpositioned cases. The rotated configuration represents the most critical condition, not only because it reaches the lowest final maximum displacement, but also because it saturates earlier than the other cases and remains below them during the terminal part of systole. Its three-dimensional displacement map confirms a clear loss of symmetry, with one leaflet appearing less open than the others. Rotational malpositioning therefore affects both the magnitude and the spatial distribution of leaflet excursion.
The axial malposition cases show a different behaviour. The downward-translated configuration eventually reaches the highest maximum displacement, but this occurs because its opening continues for a longer time and increases more markedly in the terminal phase. For this reason, its larger peak value should not be interpreted straightforwardly as an indicator of better valve performance. The corresponding displacement map suggests that this larger excursion is not associated with a fully regular opening pattern. The upward-translated case behaves as an intermediate condition, remaining close to the nominal TAVI during most of the opening phase and reaching a final peak between the nominal and the native configurations.
Overall, the combined interpretation of the temporal curves and three-dimensional displacement maps indicates that maximum leaflet displacement should be evaluated not only in terms of peak magnitude, but also in terms of temporal evolution and opening symmetry. Within this framework, the rotated configuration is the most penalized case, whereas the nominal TAVI represents the most balanced prosthetic condition.

5.2.2 Maximum Von Mises stress

In order to compare leaflet stresses consistently across all five configurations, the analysis of the maximum von Mises stress was based primarily on a common time instant rather than on the final peak value alone. The time $t = 0.055$ s was selected because it represents the last time step shared by all simulations and therefore allows a direct comparison under the same loading conditions.
At this time instant, the maximum von Mises stress is equal to 2.16×10^5 Pa for the native configuration, 2.04×10^5 Pa for the nominal TAVI, 1.98×10^5

Pa for the upward-translated case, 1.88×10^5 Pa for the downward-translated case, and 1.83×10^5 Pa for the rotated configuration. The native valve therefore exhibits the highest stress level at the same physical time, followed by the nominal TAVI and the upward-translated configuration, whereas the rotated and downward-translated cases show lower values.

From a qualitative standpoint, all configurations exhibit a similar general pattern, characterized by relatively low stress levels over most of the leaflet surface and localized high-stress regions near the commissures and along the free edge. A more detailed inspection of the stress maps reveals meaningful differences among the five configurations. The native valve, taken as the physiological reference, shows the highest stress value at the selected time, with stress strongly localized at the commissures and along the free edge. The nominal TAVI displays a slightly lower maximum value, but the overall stress pattern remains regular and consistent with a trileaflet prosthetic configuration.

The upward-translated case shows stress concentrations that remain marked near the commissures and partially extend toward the leaflet body, suggesting that upward displacement alters the load distribution without substantially relieving local stress concentrations. The downward-translated configuration exhibits a lower stress level at the common time instant, but its temporal evolution indicates a delayed and pronounced increase, eventually reaching values close to those of the native case. This suggests that downward displacement does not eliminate high-stress conditions, but rather shifts them to later stages of the opening phase.

The rotated configuration shows the lowest maximum stress at $t = 0.055$ s. However, this result should not be interpreted as evidence of better mechanical performance. In fact, the same configuration also exhibits the strongest asymmetry in leaflet motion and the earliest loss of convergence. The lower stress magnitude at the selected time is therefore more likely associated with an altered load-sharing mechanism than with a truly improved structural condition.

Overall, the von Mises stress analysis confirms that even limited variations in prosthesis positioning modify not only the magnitude of leaflet stress, but also its spatial distribution and temporal evolution. From a biomechanical perspective, these differences may be relevant because the commissural regions

and free edges are precisely the areas most associated with the onset of tissue damage and long-term structural degeneration.

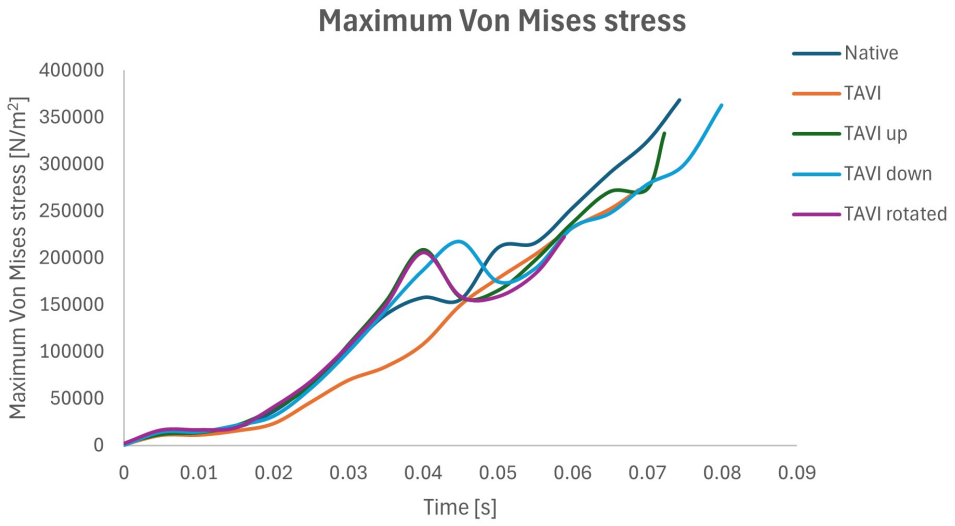

Figure 5.7: Time evolution Von Mises stress distribution of the five configurations.

In order to compare leaflet stresses consistently across all five configurations, the analysis of the maximum von Mises stress was based primarily on a common time instant rather than on the final peak value alone. The time $t = 0.055$ s was selected because it represents the last time step shared by all simulations and therefore allows a direct comparison under the same loading conditions. At this time instant, the maximum von Mises stress is equal to 2.16×10^5 Pa for the native configuration, 2.04×10^5 Pa for the nominal TAVI, 1.98×10^5 Pa for the upward-translated case, 1.88×10^5 Pa for the downward-translated case, and 1.83×10^5 Pa for the rotated configuration. The native valve therefore exhibits the highest stress level at the same physical time, followed by the nominal TAVI and the upward-translated configuration, whereas the rotated and downward-translated cases show lower values.
From a qualitative standpoint, all configurations exhibit a similar general pattern, characterized by relatively low stress levels over most of the leaflet surface and localized high-stress regions near the commissures and along the free edge. This behaviour is consistent with previous biomechanical studies, which report

peak leaflet stresses in the commissural and attachment regions because of the local curvature and the constrained nature of these areas.

A more detailed inspection of the stress maps reveals meaningful differences among the five configurations. The native valve, taken as the physiological reference, shows the highest stress value at the selected time, with stress strongly localized at the commissures and along the free edge. The nominal TAVI displays a slightly lower maximum value, but the overall stress pattern remains regular and consistent with a trileaflet prosthetic configuration.

The upward-translated case shows stress concentrations that remain marked near the commissures and partially extend toward the leaflet body, suggesting that upward displacement alters the load distribution without substantially relieving local stress concentrations. The downward-translated configuration exhibits a lower stress level at the common time instant, but its temporal evolution indicates a delayed and pronounced increase, eventually reaching values close to those of the native case. This suggests that downward displacement does not eliminate high-stress conditions, but rather shifts them to later stages of the opening phase.

The rotated configuration shows the lowest maximum stress at $t = 0.055$ s. However, this result should not be interpreted as evidence of better mechanical performance. In fact, the same configuration also exhibits the strongest asymmetry in leaflet motion and the earliest loss of convergence. The lower stress magnitude at the selected time is therefore more likely associated with an altered load-sharing mechanism than with a truly improved structural condition.

Overall, the von Mises stress analysis confirms that even limited variations in prosthesis positioning modify not only the magnitude of leaflet stress, but also its spatial distribution and temporal evolution. From a biomechanical perspective, these differences may be relevant because the commissural regions and free edges are precisely the areas most associated with the onset of tissue damage and long-term structural degeneration.

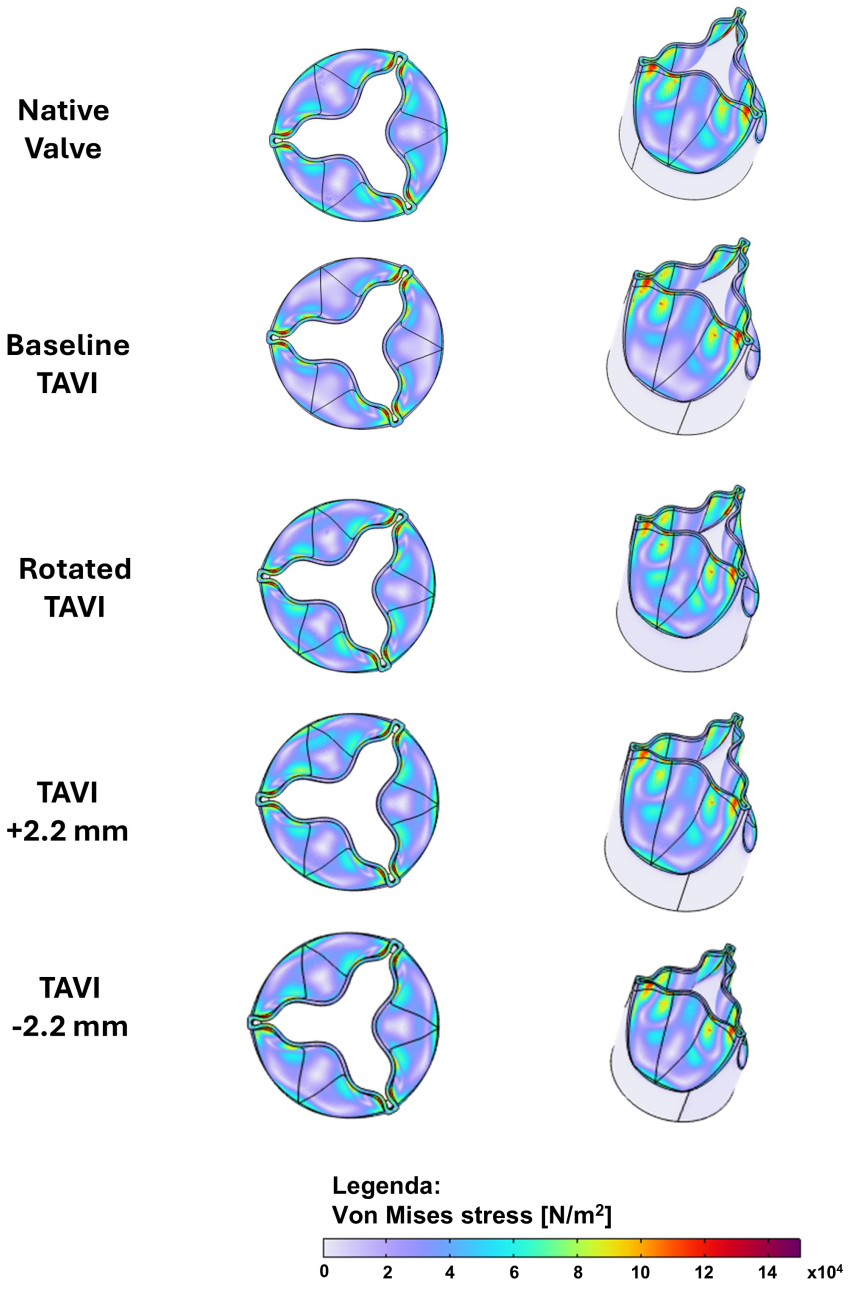

Figure 5.8: von Mises stress distribution in the five configurations at $t = 0.055$ s.

5.3 Hemodynamic comparison

In order to evaluate the hemodynamic response of the five configurations, two complementary indicators were analysed: the transvalvular pressure drop and the maximum fluid velocity. The use of these quantities is consistent with standard approaches to the assessment of aortic valve function, since pressure gradients and jet velocities are key descriptors of valvular hemodynamic performance [77].

The transvalvular pressure drop was computed as the difference between the area-averaged pressure evaluated on two cross-sectional planes located upstream and downstream of the valve. The two planes were positioned sufficiently close to the prosthesis to capture the pressure variation induced by the valve, while remaining outside the immediate leaflet region in order to reduce the influence of local numerical disturbances.

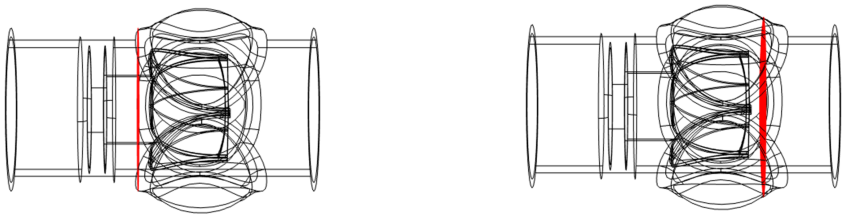

Figure 5.9: Cut planes used for the transvalvular pressure drop measurement.

It should be noted that the first value at $t = 0$ and the last value at the final time step were excluded from the graphical representation of the pressure drop. These points deviated markedly from the overall trend and were considered non-representative of the physical response. The initial value is affected by the start-up condition of the transient simulation, when the flow field is not yet developed, whereas the final value may be influenced by incomplete convergence near the end of the computation. Their exclusion therefore allows a clearer and more reliable comparison among the different configurations.

The temporal evolution of the pressure drop is shown in Figure 5.10. All

configurations exhibit a similar trend during the initial phase, with only limited differences up to approximately $t = 0.03$–0.035 s. Thereafter, the curves progressively diverge, indicating that the influence of valve geometry and prosthesis positioning becomes more pronounced as systolic opening develops. At the common comparison time $t = 0.055$ s, the native configuration exhibits the lowest pressure drop, whereas all prosthetic configurations show higher values. The upward- and downward-translated cases display the largest pressure levels, while the nominal TAVI and the rotated configuration remain intermediate.

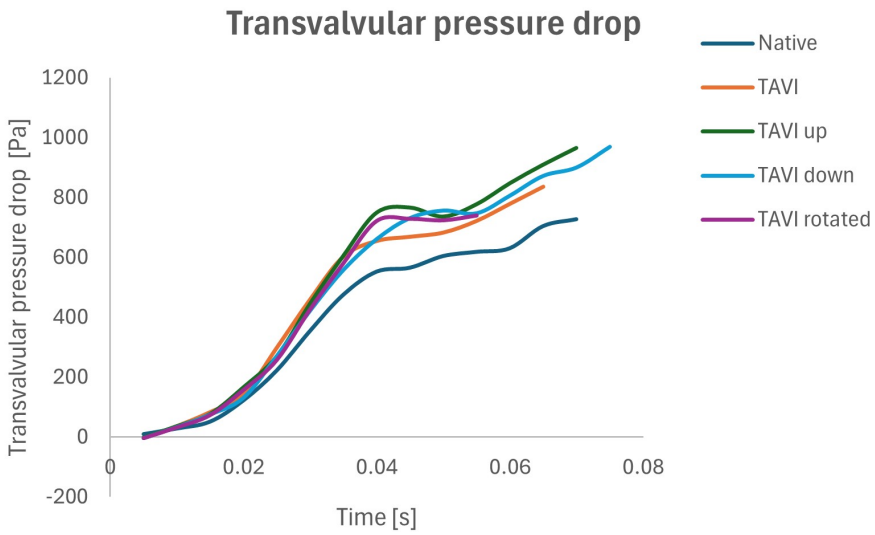

Figure 5.10: Temporal evolution of the transvalvular pressure drop for the five configurations.

The maximum fluid velocity was evaluated as the maximum velocity magnitude within the fluid domain at each time step, thereby providing an estimate of the intensity of the transvalvular jet. The corresponding curves are reported in Figure 5.11.
The velocity curves display a similar early trend in all configurations, suggesting that the initial flow acceleration is only weakly affected by the investigated geometric variations. More pronounced differences appear in the second part of the analysed interval. In particular, the downward-translated configuration reaches the highest velocity values, indicating a stronger jet development. The upward-translated case also shows an evident increase in velocity, while the

rotated configuration maintains comparatively lower values. The native and nominal TAVI cases remain intermediate and relatively close over most of the analysed time interval.

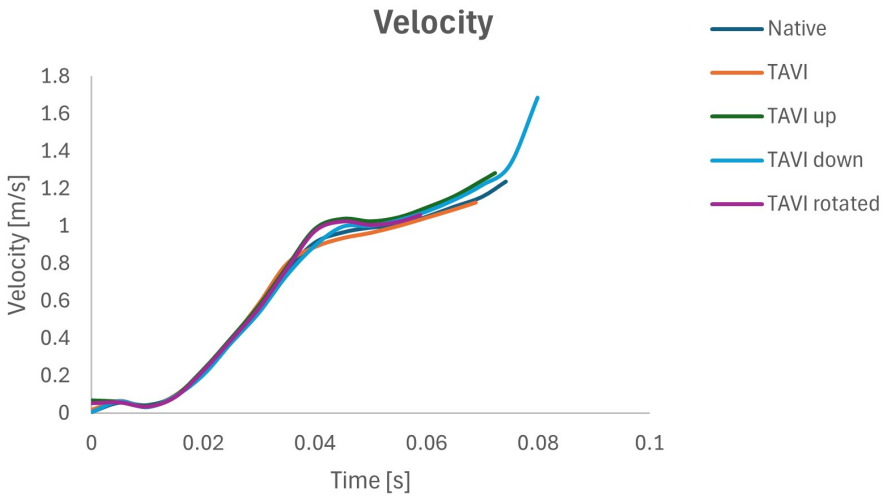

Figure 5.11: Temporal evolution of the maximum velocity for the five configurations.

A combined interpretation of the two indicators provides a more complete view of the hemodynamic response. In general, the configurations associated with higher maximum velocities also exhibit larger transvalvular pressure drops, indicating a stronger local acceleration of the flow and a higher resistance to forward passage. This behaviour is especially evident in the downward-translated configuration, which combines the highest jet intensity with one of the largest pressure drops. The upward-translated case shows a similar tendency, although to a slightly lesser extent.
By contrast, the native valve consistently exhibits the lowest pressure drop at the common comparison time while preserving a comparatively regular velocity distribution. This suggests that the physiological configuration enables a more efficient transvalvular flow development, with lower energy losses. The nominal TAVI represents an intermediate condition, whereas the rotated case appears less penalized than the translated configurations in terms of these two global hemodynamic indicators, despite remaining the most critical one from the standpoint of symmetry and regularity of opening.

Overall, the hemodynamic analysis indicates that prosthesis positioning has a relevant impact on the early systolic response. In particular, axial displacement tends to increase both jet velocity and pressure drop, whereas rotational misalignment has a less pronounced effect on these global metrics but markedly affects the spatial organization of the flow.

5.4 Comparative discussion of the five configurations

The combined qualitative and quantitative results allow a global comparison of the five investigated configurations. A summary of the main quantitative indicators extracted from the simulations is reported in Table 5.1.

Configuration	**Final conv. time [s]**	$u_{leaf,max}$ **peak [mm]**	$u_{leaf,max}$ **at** $t = 0.055$**s [mm]**	$\sigma_{vM,max}$ **at** $t = 0.055$**s [Pa]**	v_{max} **peak [m/s]**	Δp **peak [Pa]**
Native	0.0743	7.14	3.18	2.16×10^5	1.2384	727
Nominal TAVI	0.0688	5.22	3.22	2.04×10^5	1.1264	836
Downward-translated	0.0800	7.67	3.22	1.88×10^5	1.6853	970
Upward-translated	0.0723	5.98	3.40	1.98×10^5	1.2817	965
Rotated	0.0589	3.86	3.25	1.83×10^5	1.0590	739

Table 5.1: Summary of the main quantitative indicators extracted for the five configurations.

The native valve represents the reference condition and consistently shows the most regular opening pattern, the most centred systolic jet, and the lowest transvalvular pressure drop. These features indicate the most efficient flow organization within the analysed early systolic interval.
The nominal TAVI configuration can be regarded as the most balanced prosthetic condition. Although its opening remains more constrained than that of the native valve and its final leaflet excursion is lower, it preserves a relatively regular kinematic pattern and intermediate hemodynamic behaviour. The native valve represents the reference condition and consistently shows the most

regular opening pattern, the most centred systolic jet, and, within the adopted simplified framework, the lowest resistance to forward flow.

The rotated configuration is the most critical one from a kinematic standpoint. It exhibits the lowest maximum leaflet displacement, the clearest asymmetry in the opening pattern, the most localized jet development in the qualitative contours, and the earliest loss of convergence. Even though its global pressure-drop and velocity levels are not the highest, its overall behaviour indicates that rotational misalignment has a strongly detrimental effect on the regularity of valve function.

The downward-translated configuration reaches the highest final leaflet displacement and the most intense jet, but these results should not be interpreted as evidence of better performance. In fact, this configuration also exhibits one of the highest pressure drops and a less homogeneous opening pattern. Its behaviour suggests an altered and more forceful flow passage rather than a more physiological one.

Finally, the upward-translated configuration behaves as an intermediate malpositioned case. Its leaflet displacement remains higher than that of the nominal TAVI at matched late time instants, but it is also associated with elevated pressure-drop values and marked commissural stresses. This suggests that shallow implantation can modify both mechanical loading and forward-flow resistance, even when the opening pattern remains less perturbed than in the rotated case.

Overall, the results indicate that prosthesis malpositioning affects the investigated system through different mechanisms. Rotational misalignment primarily disrupts opening symmetry and jet organization, whereas axial translation more strongly alters global hemodynamic metrics such as pressure drop and velocity. These findings support the importance of considering not only whether the prosthesis is implanted, but also how it is positioned within the aortic root when assessing early systolic valve performance.

Chapter 6

Conclusions and Future developments

This thesis presented the progressive development of a three-dimensional FSI workflow in COMSOL Multiphysics for the analysis of early systolic behaviour in transcatheter aortic valve configurations. The work was structured as a stepwise numerical development pathway. It started from simplified tutorial cases, which were used to gain familiarity with the FSI interfaces, moving boundaries, solver settings, and ALE mesh deformation. It then progressed to the preliminary casting geometry, which represented the first anatomically relevant testbed on which the computational strategy could be transferred to a realistic valve environment. In this sense, the tutorial and casting phases should not be regarded as ancillary parts of the thesis, but as integral components of the work, because they allowed the numerical framework to be constructed, tested, and progressively stabilized before the final TAVI analysis.

The casting phase was particularly important from a methodological perspective. It enabled the first exploration of experimentally informed boundary conditions, transient opening simulations, and simplified leaflet-contact modelling, while at the same time making the principal numerical bottlenecks explicit, especially in relation to mesh distortion, moving-mesh sensitivity, and convergence loss. The indications obtained in this stage directly informed the final modelling choices, including the use of stationary initialization, the more controlled meshing strategy, and the restriction of the final simulations

to the opening phase. Therefore, one of the main outcomes of the thesis lies not only in the comparison among the final TAVI configurations, but also in the development of a coherent COMSOL-based workflow capable of reaching anatomically meaningful and interpretable transient FSI solutions within a controlled scope.

Within this framework, the workflow was progressively extended to a final modular TAVI model derived directly from the CAD files of the experimental platform available at the CAVE Lab. Five configurations were investigated: the native valve, a nominal TAVI configuration, two axially translated prosthetic configurations, and one rotated configuration. The study was specifically focused on the valve opening phase, in order to analyse how implantation and malpositioning affect leaflet kinematics and the associated early systolic haemodynamic response under a common set of boundary conditions.

The results showed that the native valve preserved the most regular opening pattern and, within the adopted simplified framework, the lowest resistance to forward flow, characterized by a wider and more symmetric orifice, a more centred jet, and the lowest transvalvular pressure drop among the analysed cases. The nominal TAVI configuration represented the most balanced prosthetic response among the simulated configurations. Among the malpositioned cases, rotational misalignment emerged as the most critical condition from a kinematic standpoint, since it produced the strongest asymmetry in leaflet motion and the earliest loss of convergence. By contrast, axial translations mainly affected the global haemodynamic indicators, leading to higher jet velocities and larger transvalvular pressure drops, especially in the downward-translated configuration. The stress analysis further showed that the highest von Mises stresses were mainly localized near the commissures and along the free leaflet edges, confirming that even limited changes in prosthesis positioning can alter both the magnitude and the spatial distribution of leaflet loading.

Overall, the present work confirms that prosthesis malpositioning cannot be interpreted as a purely geometric issue, since even controlled changes in axial position or rotational alignment may produce measurable differences in valve opening, stress distribution, and early systolic flow organization. At the same time, the main value of the present framework lies in providing a controlled comparative setting in which the effect of positioning can be isolated while

preserving coherence with the experimental platform from which the geometry was derived. In this sense, the developed model represents not only a comparative numerical investigation, but also a first methodological step toward a future integrated in silico–in vitro analysis of TAVI performance.

A first limitation of the present work is that the simulations were restricted to the opening phase only. This choice was necessary because the complete numerical treatment of valve dynamics in COMSOL remains particularly challenging in the presence of strong nonlinearities, large structural displacements, moving-mesh deformation, and the complex interaction between the prosthetic frame and the leaflets. As reported in the thesis, all five simulations lost convergence during early systole, with a common reliable interval limited to approximately 0.07 s, while the rotated configuration stopped even earlier. Consequently, the study could not address the full cardiac cycle, leaflet closure, regurgitation phenomena, or washout-related quantities, which remain important aspects of prosthetic valve performance.

A second important limitation concerns the numerical robustness of the adopted ALE-based FSI framework. During model development, the solution process was repeatedly affected by numerical instabilities associated with mesh distortion in the fluid domain, especially in regions characterized by narrow gaps, strong leaflet excursion, and local deformation gradients. In practical terms, these difficulties manifested as repeated non-convergence, severe deterioration of mesh quality, and situations compatible with local inverted mesh elements, which are typical critical issues in moving-mesh simulations of highly deformable valve systems. In this respect, the tutorial and casting phases were also valuable because they made these limitations explicit and helped identify the numerical choices that were necessary to bring the final workflow to a controlled and interpretable stage.

Additional limitations derive from the modelling assumptions adopted to maintain tractability. In the present framework, the fluid was modeled as water and the solid domains were represented using linear elastic constitutive laws. While these choices improved numerical robustness and preserved consistency with the mock-loop setup, they do not reproduce the full rheological behaviour of blood nor the nonlinear, hyperelastic, and anisotropic response of native and prosthetic valve tissues. As a consequence, the absolute values of stress,

velocity, and transvalvular pressure drop obtained in this study cannot be interpreted as direct physiologic predictions of in-vivo valve function. Their main value lies instead in enabling a controlled relative comparison among configurations simulated under the same assumptions, so as to isolate the effect of prosthesis positioning. In this sense, the present results should be read primarily as comparative indicators of how malpositioning alters leaflet kinematics and early systolic flow organisation within a simplified but coherent computational framework.

Moreover, the investigated TAVI positions were imposed geometrically rather than obtained through a full simulation of crimping, deployment, and anchoring inside a realistic pathological anatomy. Similarly, the present model did not include calcifications, coronary flow, or patient-specific anatomical variability. These simplifications do not invalidate the comparative significance of the analysis, but they do limit the direct physiologic generalization of the obtained quantitative values.

Future developments should therefore proceed along both numerical and modelling directions. From the numerical side, an important improvement would be the stabilization of the FSI solution strategy through more advanced mesh-handling techniques, including stronger local refinement, improved boundary-layer discretization, adaptive remeshing procedures, and smaller time-step control during the most critical phases of leaflet motion. A more robust treatment of contact during closure would also be essential to extend the simulations beyond the opening phase and to reproduce the complete cardiac cycle. In this respect, future work could also explore alternative formulations that are less sensitive to large mesh distortions, especially for configurations involving stronger deformation or leaflet–stent interaction.

From a modelling perspective, a priority development will be the introduction of more physiologically representative assumptions, including more realistic constitutive laws for the leaflets, sinus wall, and support structures, as well as a more representative blood or blood-analog fluid model. These improvements would make it possible to move progressively from the present simplified comparative framework toward a model with stronger physiologic predictive value. Additional extensions should include patient-specific anatomical features such as calcific deposits, non-circular implantation environments, and coronary out-

lets, together with the explicit simulation of the TAVI deployment phase so that the final prosthesis position and shape arise from procedural mechanics rather than from idealized imposed manipulations.

Finally, the most relevant future development is the quantitative validation of the numerical model against the experimental mock-loop platform. Since the computational geometry was derived from the same CAD files used in the laboratory setup, and since the experimental campaign already included high-speed camera acquisitions as well as pressure and flow measurements, the developed framework is well suited for a future in silico–in vitro comparison. Such a validation step would allow leaflet opening dynamics, pressure drop, and velocity-related indicators to be compared directly between simulations and experiments, thereby strengthening the credibility of the model and enabling its use as a more robust tool for the study of TAVI malpositioning. In this sense, the present thesis should be regarded as a first step toward a more comprehensive and progressively validated computational platform for the investigation of prosthetic aortic valve performance.

Appendix A

Casting Studies Summary and Simulation Results

In order to identify a sufficiently stable numerical setup for the casting simulations, several preliminary tests were carried out by progressively varying the study type, boundary conditions, time discretization, mesh, and selected solver settings. At this stage, the goal was not yet the quantitative analysis of the results, but rather the assessment of the numerical robustness of the model and the identification of the main causes of non-convergence. Table A therefore summarizes the tested cases, highlighting for each configuration the adopted modeling choices, the implemented modifications, and the main observations in terms of convergence and numerical issues.

Study	**Type**	**Main conditions**	**Mesh / time stepping**	**Main modifications**	**Outcome / observations**
`Casting_LC_p400`	Stationary	Constant pressure inlet (4000 Pa); zero-pressure outlet; active moving mesh	Coarse mesh	Added fully coupled approach; modified tolerance and nonlinearity settings; number of iterations increased from 25 to 50	No convergence; study used as the first reference attempt

Study	Type	Main conditions	Mesh / time stepping	Main modifications	Outcome / observations
`Casting_LC_rampa`	Time-dependent	Pressure ramp at the inlet through a piecewise function; zero-pressure outlet	`range(0,0.05,0.2)`; coarse mesh	Pressure ramp imposed to describe the initial leaflet opening	No convergence; possible non-physical fluid passage between wall and valve
`Casting_LC_triangle`	Time-dependent	Triangular pressure profile at the inlet to simulate the beginning of systole; zero-pressure outlet	`range(0,0.05,0.2)`; coarse mesh	Replaced the ramp with a triangular law	No convergence; issues similar to the previous case, with problems related to geometry and solver parameters
`Casting_LC_closep4000_std1`	Stationary	Constant pressure inlet (4000 Pa); zero-pressure outlet	Mesh more refined than in the initial cases	Closed the gap between valve and vessel; fluid mesh changed from coarse to normal; fully coupled with direct solver; iterations increased to 70; relative tolerance set to 0.1	No convergence; different error compared with the previous cases, possibly related to a fluid jump
`Casting_LC_closep4000_std2`	Stationary	Variant of the previous case with the same basic setup	Non-uniform mesh (normal/coarse)	Further attempt to stabilize the setup	Unsatisfactory or inconclusive results; configuration retained as an intermediate test
`Casting_LC_closeT_ramp`	Time-dependent	Pressure ramp at the inlet; zero-pressure outlet	Modified mesh; simulation stopped before the final time	Mesh size 2 changed to normal; added fixed constraint; switched from Direct 2 to Direct; iterations increased from 4 to 25; stepping changed from automatic to constant	No convergence; the simulation stopped at about 0.11 s instead of 0.2 s

Study	**Type**	**Main conditions**	**Mesh / time stepping**	**Main modifications**	**Outcome / observations**
`Casting_LC_close_ramp_std1`	Time-dependent	Variant of the `close_ramp` case	Locally refined mesh	Mesh quality analysis; very low minimum element quality detected (≈ 0.032); local refinement proposed especially in the vessel; ramp made more consistent	No convergence; critical issues mainly attributed to mesh quality
`Casting_LC_Vin`	Time-dependent	Inlet velocity profile V_{in} from FlowMockTAVI; zero-pressure outlet	Normal mesh	Modified minimum damping factor; corrected and realigned the geometry	No convergence, despite a better aligned geometric configuration
`Casting_LC_Vin_+5mm`	Time-dependent	Same V_{in} profile as in the previous case; zero-pressure outlet	Normal mesh	Geometry translated upward by $+5$ mm	Outcome similar to the previous case; numerical issues persisted in the same time interval
`Casting_LC_Vin_v2`	Time-dependent	Imported V_{in} profile at the inlet; zero-pressure outlet	Fine mesh	Further variation of the inlet profile and numerical setup	No convergence; useful test to assess the effect of the imposed inlet profile
`Casting_LC_Vin_v3`	Time-dependent	V_{in} profile over a single cycle at the inlet; zero-pressure outlet	Fine mesh; custom time stepping	Further refinement of the setup with custom time discretization	Final attempt of the `Vin` series; useful as a sensitivity test for mesh and time stepping

Table A.1: Summary of the preliminary tests performed for the casting simulations.

Appendix B

Mock loop setup

The experimental activity was carried out using the mock loop available at the CAVE Lab. The system was designed to reproduce the pulsatile haemodynamics of the left heart under controlled in vitro conditions, allowing pressure and flow measurements to be acquired upstream and downstream of the tested valve configuration. In agreement with the experimental protocol previously adopted in the laboratory, the mock loop includes a set of hydraulic, mechanical and measurement components that ensure control of preload, afterload and signal acquisition. A general view of the experimental apparatus is shown in Figure B.1.

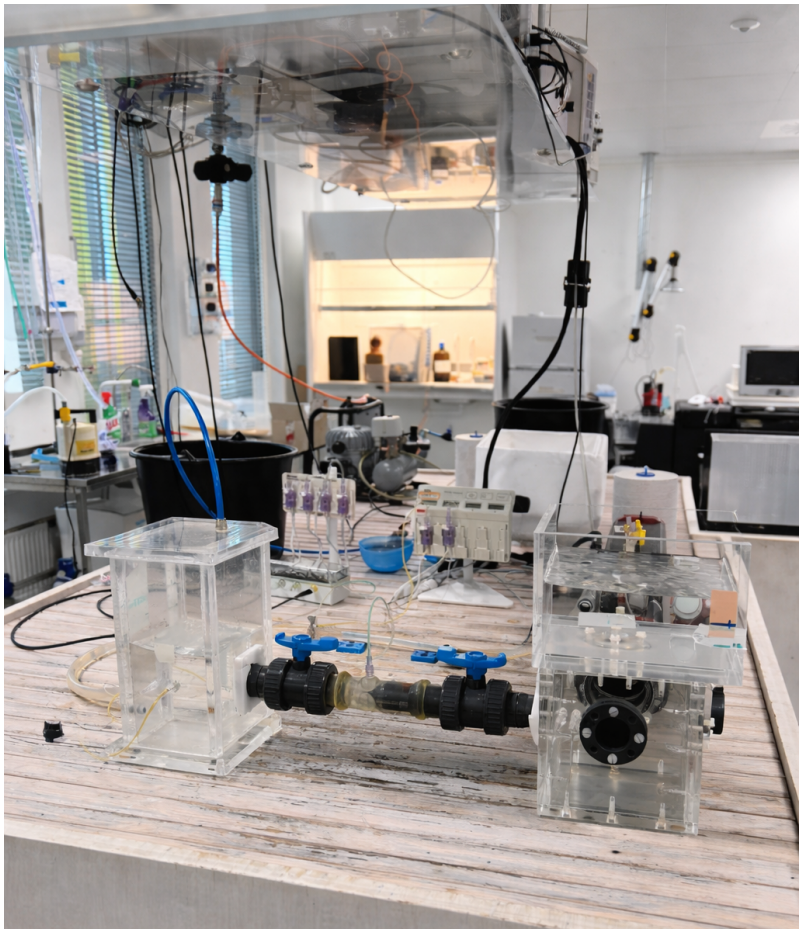

Figure B.1: Overview of the mock loop used for the in vitro experiments at the CAVE Lab. The system includes the atrial and ventricular chambers, the compliance chamber, the afterload resistance line, the Vivitro piston pump, flow probes, pressure acquisition system, and the test section where the investigated valve configuration was mounted.

The main components of the mock loop are listed below:

- Atrial chamber: reservoir representing the left atrium and used to collect the returning working fluid.
- Ventricular chamber: chamber representing the left ventricle, connected to the actuation system to generate the pulsatile flow.
- Compliance chamber: element used to reproduce the arterial compliance of the system and to regulate pressure conditions in the loop.

- Valve support assembly: support structure used to house and position the tested valve configuration inside the circuit. As visible in the experimental setup, this element includes the mounting region for the valve and ensures its stable connection with the upstream and downstream sections of the mock loop.
- Afterload resistance tube: hydraulic branch used to reproduce peripheral resistance and connected back to the atrial chamber.
- Vivitro piston pump: electromechanical actuation system used to impose the pulsatile waveform in the loop.
- Connectors: rigid connectors used to link the different chambers, tubes and test section, while also allowing the integration of pressure measurement points.
- Flow probes: sensors positioned along the circuit to measure the flow rate during the cardiac cycle.
- Flow monitor: acquisition unit connected to the flow probes for real-time recording of the flow signal.
- Pressure catheters and pressure scan: pressure measurement system used to acquire ventricular and aortic pressure signals.

Bibliography

[1] Iso 5840-3:2013 cardiovascular implants — cardiac valve prostheses — part 3: Heart valve substitutes implanted by transcatheter techniques, 2013.

[2] Iso 5840-3:2021 cardiovascular implants — cardiac valve prostheses — part 3: Heart valve substitutes implanted by transcatheter techniques, 2021.

[3] Johns Hopkins Medicine. Cardiovascular diseases, n.d.

[4] Physio-Pedia. Anatomy of the human heart. https://www.physio-pedia.com/Anatomy$_o f_t he_H uman_H eart$, 2026.

[5] Prashant Nagpal, Mukta D Agrawal, Sachin S Saboo, Sandeep Hedgire, Sarv Priya, and Michael L Steigner. Imaging of the aortic root on high-pitch non-gated and ecg-gated ct: awareness is the key! *Insights into imaging*, 11(1):51, 2020.

[6] Petr Fila. *Rizikové faktory ovlivňující selhání záchovné operace aortální chlopně*. Disertační práce, Masarykova univerzita, Lékařská fakulta, Brno, 2016.

[7] Oliver Jones. The valves of the heart, 2025. TeachMeAnatomy.

[8] Riccardo Toninato, Jacob Salmon, Francesca Maria Susin, Andrea Ducci, and Gaetano Burriesci. Physiological vortices in the sinuses of valsalva: an in vitro approach for bio-prosthetic valves. *Journal of biomechanics*, 49(13):2635–2643, 2016.

[9] Takashi Kunihara. Anatomy of the aortic root: implications for aortic root reconstruction. *General thoracic and cardiovascular surgery*, 65(9):488–499, 2017.

[10] Michele Conti. Prosthetic cardiac valves, 2024. Slides del corso di Bioingegneria, Laurea Magistrale in Bioingegneria, Università degli Studi di Pavia, a.a. 2023/2024, materiale didattico non pubblicato.

[11] Brian R Lindman, Marie-Annick Clavel, Patrick Mathieu, Bernard Iung, Patrizio Lancellotti, Catherine M Otto, and Philippe Pibarot. Calcific aortic stenosis. *Nature reviews Disease primers*, 2(1):1–28, 2016.

[12] Gaetano Thiene, Stefania Rizzo, and Cristina Basso. Bicuspid aortic valve: The most frequent and not so benign congenital heart disease. *Cardiovascular Pathology*, 70:107604, 2024.

[13] M Charlesworth, BG Williams, and MH Buch. Advances in transcatheter aortic valve implantation, part 2: perioperative care. *BJA education*, 21(7):264–269, 2021.

[14] Jonathon P Fanning, David G Platts, Darren L Walters, and John F Fraser. Transcatheter aortic valve implantation (tavi): valve design and evolution. *International journal of cardiology*, 168(3):1822–1831, 2013.

[15] Ke-Wei Xu, Qi Gao, Min Wan, and Ke Zhang. Mock circulatory loop applications for testing cardiovascular assist devices and in vitro studies. *Frontiers in physiology*, 14:1175919, 2023.

[16] Finja Borowski, Sebastian Kaule, Jan Oldenburg, Klaus-Peter Schmitz, Alper Öner, and Michael Stiehm. Analysis of thrombosis risk of commissural misaligned transcatheter aortic valve prostheses using particle image velocimetry. *Tm-technisches Messen*, 91(6):291–304, 2024.

[17] ViVitro Labs. Pulse duplicator. https://vivitrolabs.com/product/pulse-duplicator/, 2026. Accessed: 2026-03-17.

[18] Ernest Young, Ji-Feng Chen, Owen Dong, Shengqiang Gao, Alex Massiello, and Kiyotaka Fukamachi. Transcatheter heart valve with

variable geometric configuration: in vitro evaluation. *Artificial organs*, 35(12):1151–1159, 2011.

[19] Jordan A Brown, Jae H Lee, Margaret Anne Smith, David R Wells, Aaron Barrett, Charles Puelz, John P Vavalle, and Boyce E Griffith. Patient–specific immersed finite element–difference model of transcatheter aortic valve replacement. *Annals of biomedical engineering*, 51(1):103–116, 2023.

[20] Salvatore Pasta, Stefano Cannata, Giovanni Gentile, Marzio Di Giuseppe, Federica Cosentino, Francesca Pasta, Valentina Agnese, Diego Bellavia, Giuseppe M Raffa, Michele Pilato, et al. Simulation study of transcatheter heart valve implantation in patients with stenotic bicuspid aortic valve. *Medical & biological engineering & computing*, 58(4):815–829, 2020.

[21] Xiangkun Liu, Wen Zhang, Ping Ye, Qiyi Luo, and Zhaohua Chang. Fluid-structure interaction analysis on the influence of the aortic valve stent leaflet structure in hemodynamics. *Frontiers in physiology*, 13:904453, 2022.

[22] Giulia Luraghi, Francesco Migliavacca, Alberto García-González, Claudio Chiastra, Alexia Rossi, Davide Cao, Giulio Stefanini, and Jose Felix Rodriguez Matas. On the modeling of patient-specific transcatheter aortic valve replacement: A fluid–structure interaction approach: Luraghi et al. *Cardiovascular engineering and technology*, 10(3):437–455, 2019.

[23] I. Rehman and A. Rehman. *Anatomy, Thorax, Heart*. StatPearls Publishing, Treasure Island (FL), 2025. [Updated 2023 Aug 28].

[24] Efstratios I Charitos and Hans-Hinrich Sievers. Anatomy of the aortic root: implications for valve-sparing surgery. *Annals of cardiothoracic surgery*, 2(1):53, 2013.

[25] Muditha Lansakara and Shinya Unai. An overview of aortic valve anatomy: the current understanding. *Indian Journal of Thoracic and Cardiovascular Surgery*, 39(Suppl 2):246–252, 2023.

[26] Frederick J Schoen. Cardiac valves and valvular pathology: update on function, disease, repair, and replacement. *Cardiovascular Pathology*, 14(4):189–194, 2005.

[27] Kevin D O'Brien. Epidemiology and genetics of calcific aortic valve disease. *Journal of Investigative Medicine*, 55(6):284–291, 2007.

[28] Choon-Sik Jhun, Raymond Newswanger, Joshua P Cysyk, Sailahari Ponnaluri, Bryan Good, Keefe B Manning, and Gerson Rosenberg. Dynamics of blood flows in aortic stenosis: mild, moderate, and severe. *ASAIO Journal*, 67(6):666–674, 2021.

[29] Gry Wisthus Eveborn, Henrik Schirmer, Geir Heggelund, Per Lunde, and Knut Rasmussen. The evolving epidemiology of valvular aortic stenosis. the tromsø study. *Heart*, 99(6):396–400, 2013.

[30] Jagmeet P Singh, Jane C Evans, Daniel Levy, Martin G Larson, Lisa A Freed, Deborah L Fuller, Birgitta Lehman, and Emelia J Benjamin. Prevalence and clinical determinants of mitral, tricuspid, and aortic regurgitation (the framingham heart study). *The American journal of cardiology*, 83(6):897–902, 1999.

[31] Gerald Maurer. Aortic regurgitation. *Heart*, 92(7):994–1000, 2006.

[32] Samuel C Siu and Candice K Silversides. Bicuspid aortic valve disease. *Journal of the American College of Cardiology*, 55(25):2789–2800, 2010.

[33] William C Roberts. Anatomically isolated aortic valvular disease: the case against its being of rheumatic etiology. *The American journal of medicine*, 49(2):151–159, 1970.

[34] John P Veinot. Pathology of inflammatory native valvular heart disease. *Cardiovascular Pathology*, 15(5):243–251, 2006.

[35] Adriana Postolache, Simona Sperlongano, and Patrizio Lancellotti. Tavi after more than 20 years. *Journal of clinical medicine*, 12(17):5645, 2023.

[36] Callum Howard, Lucas Jullian, Mihika Joshi, Arish Noshirwani, Mohamad Bashir, and Amer Harky. Tavi and the future of aortic valve replacement. *Journal of cardiac surgery*, 34(12):1577–1590, 2019.

[37] Marco Mussardo, Azeem Latib, Alaide Chieffo, Cosmo Godino, Alfonso Ielasi, Micaela Cioni, Kensuke Takagi, Giedrius Davidavicius, Matteo Montorfano, Francesco Maisano, et al. Periprocedural and short-term outcomes of transfemoral transcatheter aortic valve implantation with the sapien xt as compared with the edwards sapien valve. *JACC: Cardiovascular Interventions*, 4(7):743–750, 2011.

[38] Fadi J Sawaya, Marco Spaziano, Thierry Lefèvre, Andrew Roy, Phillippe Garot, Thomas Hovasse, Antoinette Neylon, Hakim Benamer, Mauro Romano, Thierry Unterseeh, et al. Comparison between the sapien s3 and the sapien xt transcatheter heart valves: A single-center experience. *World journal of cardiology*, 8(12):735, 2016.

[39] Eberhard Grube, Jean C Laborde, Ulrich Gerckens, Thomas Felderhoff, Barthel Sauren, Lutz Buellesfeld, Ralf Mueller, Maurizio Menichelli, Thomas Schmidt, Bernfried Zickmann, et al. Percutaneous implantation of the corevalve self-expanding valve prosthesis in high-risk patients with aortic valve disease: the siegburg first-in-man study. *Circulation*, 114(15):1616–1624, 2006.

[40] Elaine E Tseng, Andrew Wisneski, Ali N Azadani, and Liang Ge. Engineering perspective on transcatheter aortic valve implantation. *Interventional Cardiology*, 5(1):53, 2013.

[41] Benyamin Rahmani, Spyros Tzamtzis, Rose Sheridan, Michael J Mullen, John Yap, Alexander M Seifalian, and Gaetano Burriesci. In vitro hydrodynamic assessment of a new transcatheter heart valve concept (the triskele). *Journal of cardiovascular translational research*, 10(2):104–115, 2017.

[42] Philipp Aigner, Eleonora Sella Bart, Sebastiano Panfili, Tito Körner, Markus Mach, Martin Andreas, Markus Königshofer, Simone Saitta, Alberto Redaelli, Albrecht Schmid, et al. Quantification of paravalvular

leaks associated with tavi implants using 4d mri in an aortic root phantom made possible by the use of 3d printing. *Frontiers in cardiovascular medicine*, 10:1083300, 2023.

[43] Jacob Andrew Salmonsmith, Andrea Ducci, and Gaetano Burriesci. Does transcatheter aortic valve alignment matter? *Open Heart*, 6(2), 2019.

[44] Desiree Pott, Alexander Sedaghat, Christoph Schmitz, Nikos Werner, Thomas Schmitz-Rode, Ulrich Steinseifer, and Sebastian Victor Jansen. Hemodynamics inside the neo-and native sinus after tavr: Effects of implant depth and cardiac output on flow field and coronary flow. *Artificial organs*, 45(1):68–78, 2021.

[45] Leonardo Pietrasanta, Shaokai Zheng, Dario De Marinis, David Hasler, and Dominik Obrist. Characterization of turbulent flow behind a transcatheter aortic valve in different implantation positions. *Frontiers in cardiovascular medicine*, 8:804565, 2022.

[46] Brandon J Kovarovic, Oren M Rotman, Puja Parikh, Marvin J Slepian, and Danny Bluestein. Patient-specific in vitro testing for evaluating tavr clinical performance—a complementary approach to current iso standard testing. *Artificial organs*, 45(4):E41–E52, 2021.

[47] Paul S Gunning, Neelakantan Saikrishnan, Laoise M McNamara, and Ajit P Yoganathan. An in vitro evaluation of the impact of eccentric deployment on transcatheter aortic valve hemodynamics. *Annals of biomedical engineering*, 42(6):1195–1206, 2014.

[48] Najla Sadat, John Habakuk Lojenburg, Michael Scharfschwerdt, Buntaro Fujta, and Stephan Ensminger. Impact of different in vitro models on functional performance of the self-expanding transcatheter heart valve. *European Journal of Cardio-Thoracic Surgery*, 64(4):ezad333, 2023.

[49] Beatrice E Ncho, Keshav Kohli, Vahid Sadri, and Ajit P Yoganathan. Effect of native aortic leaflet geometry modification on transcatheter aortic valve neo-sinus and aortic sinus flow: An in-vitro study: Ncho et al. *Cardiovascular Engineering and Technology*, 14(2):182–193, 2023.

[50] Finja Borowski, Robert Ott, Jan Oldenburg, Sebastian Kaule, Alper Öner, Klaus-Peter Schmitz, and Michael Stiehm. Validation of a fluid structure interaction model for tavr using particle image velocimetry. In *Current Directions in Biomedical Engineering*, volume 8, pages 512–515. De Gruyter, 2022.

[51] Vijay Govindarajan, Arun Kolanjiyil, Nils P Johnson, Hyunggun Kim, Krishnan B Chandran, and David D McPherson. Improving transcatheter aortic valve interventional predictability via fluid–structure interaction modelling using patient-specific anatomy. *Royal Society Open Science*, 9(2), 2022.

[52] Harkamaljot S Kandail, Setu D Trivedi, Armaan C Shaikh, Tanvir K Bajwa, Daniel P O'Hair, Arshad Jahangir, and John F LaDisa Jr. Impact of annular and supra-annular corevalve deployment locations on aortic and coronary artery hemodynamics. *Journal of the mechanical behavior of biomedical materials*, 86:131–142, 2018.

[53] Wenbin Mao, Kewei Li, and Wei Sun. Fluid–structure interaction study of transcatheter aortic valve dynamics using smoothed particle hydrodynamics. *Cardiovascular engineering and technology*, 7(4):374–388, 2016.

[54] Nikita Pil, Alex G Kuchumov, Bakytbek Kadyraliev, and Vagram Arutunyan. Influence of aortic valve leaflet material model on hemodynamic features in healthy and pathological states. *Mathematics*, 11(2):428, 2023.

[55] David Oks, Cristóbal Samaniego, Guillaume Houzeaux, Constantine Butakoff, and Mariano Vázquez. Fluid–structure interaction analysis of eccentricity and leaflet rigidity on thrombosis biomarkers in bioprosthetic aortic valve replacements. *International Journal for Numerical Methods in Biomedical Engineering*, 38(12):e3649, 2022.

[56] Adi A Basri, Mohammad Zuber, Ernnie I Basri, Muhammad S Zakaria, Ahmad FA Aziz, Masaaki Tamagawa, and Kamarul A Ahmad. Fluid structure interaction on paravalvular leakage of transcatheter aortic valve implantation related to aortic stenosis: A patient-specific case. *Computational and mathematical methods in medicine*, 2020(1):9163085, 2020.

[57] Ivan Fumagalli, Rebecca Polidori, Francesca Renzi, Laura Fusini, Alfio Quarteroni, Gianluca Pontone, and Christian Vergara. Fluid-structure interaction analysis of transcatheter aortic valve implantation. *International Journal for Numerical Methods in Biomedical Engineering*, 39(6):e3704, 2023.

[58] Michael CH Wu, Heather M Muchowski, Emily L Johnson, Manoj R Rajanna, and Ming-Chen Hsu. Immersogeometric fluid–structure interaction modeling and simulation of transcatheter aortic valve replacement. *Computer Methods in Applied Mechanics and Engineering*, 357:112556, 2019.

[59] Joris Degroote, Klaus-Jürgen Bathe, and Jan Vierendeels. Performance of a new partitioned procedure versus a monolithic procedure in fluid–structure interaction. *Computers & Structures*, 87(11-12):793–801, 2009.

[60] Michele Bucelli, Luca Dede, Alfio Quarteroni, and Christian Vergara. Partitioned and monolithic algorithms for the numerical solution of cardiac fluid-structure interaction. *Communications in Computational Physics*, 32(5):1217–1256, 2022.

[61] Sang Truong Ha, Long Cu Ngo, Muhammad Saeed, Byoung Jin Jeon, and Hyounggwon Choi. A comparative study between partitioned and monolithic methods for the problems with 3d fluid-structure interaction of blood vessels. *Journal of Mechanical Science and Technology*, 31(1):281–287, 2017.

[62] Shaily Wald, Alex Liberzon, and Idit Avrahami. A numerical study of the hemodynamic effect of the aortic valve on coronary flow. *Biomechanics and modeling in mechanobiology*, 17(2):319–338, 2018.

[63] Anna Maria Tango, Alessandra Monteleone, Andrea Ducci, and Gaetano Burriesci. Analysis of the haemodynamic changes caused by surgical and transcatheter aortic valve replacements by means fluid-structure interaction simulations. *Computers in Biology and Medicine*, 186:109673, 2025.

[64] Chiara Catalano, Roberta Scuoppo, Tahir Turgut, Vincent Bouwman, Nils Götzen, Stefano Cannata, Giovanni Gentile, Caterina Gandolfo, and

Salvatore Pasta. Credibility assessment of patient-specific modeling in transcatheter aortic valve implantation. i. a population-based validation of patient-specific modeling. *APL bioengineering*, 9(4), 2025.

[65] May YS Kuan and Daniel M Espino. Systolic fluid–structure interaction model of the congenitally bicuspid aortic valve: assessment of modelling requirements. *Computer Methods in Biomechanics and Biomedical Engineering*, 18(12):1305–1320, 2015.

[66] Marcos Loureiro-Ga, Cesar Veiga, Generosa Fdez-Manin, Victor Alfonso Jimenez, Francisco Calvo-Iglesias, and Andres Iniguez. A biomechanical model of the pathological aortic valve: simulation of aortic stenosis. *Computer Methods in Biomechanics and Biomedical Engineering*, 23(8):303–311, 2020.

[67] Hamidreza Ghasemi Bahraseman, Ehsan Mohseni Languri, Niloofar Yahyapourjalaly, and Daniel M Espino. Fluid-structure interaction modeling of aortic valve stenosis at different heart rates. *Acta of bioengineering and biomechanics*, 18(3), 2016.

[68] Jaafar Ghanbari, Amirhossein Dehparvar, and Amirhossein Zakeri. Design and analysis of prosthetic heart valves and assessing the effects of leaflet design on the mechanical attributes of the valves. *Frontiers in Mechanical Engineering*, 8:764034, 2022.

[69] A Khosravi, HG Bahraseman, K Hassani, and D Kazemi-Saleh. Numerical method to measure velocity integration, stroke volume and cardiac output while rest: using 2d fluid-solid interaction model. *Engineering Solid Mechanics*, 2(2):91–100, 2014.

[70] Andrea Avanzini, Giorgio Donzella, et al. Coupled fluid-structural analysis of heart mitral valve. In *Proceedings European COMSOL Conference 2008*. COMSOL Inc., 2008.

[71] Xiaoyang Xu and Jie Cheng. Fluid-structure interaction simulation of the three-leaflet aortic valve using comsol. *Computer Methods in Biomechanics and Biomedical Engineering*, pages 1–13, 2024.

[72] Polina Fedotova, Nikita Pil, Alex G Kuchumov, Ekaterina Barbashina, Vladimir Tsilibin, Fulufhelo Nemavhola, Thanyani Pandelani, Bakytbek Kadyraliev, and Truong Sang Ha. Numerical simulation of aortic valve leaflets calcification influence on hemodynamic performance using fluid–structure interaction approach. *Processes*, 13(11):3750, 2025.

[73] Khalid Alonazi. *Simulation of Aortic Valve Dynamics during Left Ventricular Support*. PhD thesis, UNSW Sydney, 2015.

[74] Han Hung Yeh, Oleksandr Barannyk, Dana Grecov, and Peter Oshkai. The influence of hematocrit on the hemodynamics of artificial heart valve using fluid-structure interaction analysis. *Computers in biology and medicine*, 110:79–92, 2019.

[75] Saeed Adham Esfahani, Kamran Hassani, and Daniel M Espino. Fluid-structure interaction assessment of blood flow hemodynamics and leaflet stress during mitral regurgitation. *Computer methods in biomechanics and biomedical engineering*, 22(3):288–303, 2019.

[76] K Srinivasa Rao, K Girija Sravani, G Yugandhar, G Venkateswara Rao, and VN Mani. Design and analysis of fluid structure interaction in a horizontal micro channel. *Procedia Materials Science*, 10:768–788, 2015.

[77] Domenico Angellotti, Rachele Manzo, Domenico Simone Castiello, Maddalena Immobile Molaro, Andrea Mariani, Cristina Iapicca, Dalila Nappa, Fiorenzo Simonetti, Marisa Avvedimento, Attilio Leone, et al. Hemodynamic performance of transcatheter aortic valves: a comprehensive review. *Diagnostics*, 13(10):1731, 2023.